

Thesis for the degree of Doctor of Philosophy

Tunable photonic crystals  
based on carbon nanofibers

Robert Rehammar

Department of Applied Physics  
Chalmers University of Technology  
SE-412 96 Göteborg, Sweden, 2012

Tunable photonic crystals  
based on carbon nanofibers  
ROBERT REHAMMAR  
ISBN 978-91-7385-634-8

© Robert Rehammar 2012

Doktorsavhandlingar vid Chalmers tekniska högskola,  
Ny serie nr 3315  
ISSN 0346-718X

Typeset using X<sub>Y</sub>L<sup>A</sup>T<sub>E</sub>X. Figures created using MATLAB, Inkscape, matplotlib,  
POVRAY and QtiPlot.

Cover: A SEM image of a sample and optical response in diffraction from the  
tuned sample.

Department of Applied Physics  
Chalmers University of Technology  
SE-412 96 Göteborg, Sweden, 2012

Printed by Chalmers Reproservice  
Chalmers University of Technology  
Göteborg, Sweden 2012

---

# Tunable photonic crystals based on carbon nanofibers

Robert Rehammar

Department of Applied Physics  
Chalmers University of Technology

## Abstract

Photonic crystals are materials with periodically varying refractive indices. In conventional photonic crystal design it is hard to achieve tunable structures in the visible range, *i.e.* structures with changeable optical properties.

Carbon nanofibers have dimensions similar to multi-walled carbon nanotubes, but have the advantage that they can be fabricated vertically free-standing. In this thesis the possibility to use carbon nanofibers as the basic building block for tunable two-dimensional photonic crystals is investigated. By growing nanofibers in a lattice pattern and keeping neighbouring fibers at different electrostatic potentials, the nanofibers can be bent electrostatically. This changes the lattice, which in turn modifies the optical properties of the photonic crystal.

A finite-difference time-domain method was used to model a photonic crystal with a changeable basis. It was shown that the optical transmission through a photonic crystal slab can, at a certain frequency, be switched from almost 100% to approximately 1% with only a few rows of nanofibers in the light propagation direction. It was shown that many features in the transmission can be attributed to changes in the bandstructure.

Both static and tunable carbon nanofiber photonic crystals were fabricated using catalytic DC plasma enhanced chemical vapour deposition. An optical measurement set-up was developed and used for investigating diffraction from the samples. Samples were also investigated using ellipsometry.

It was found that ellipsometry is a powerful tool for probing the band structure of 2D photonic crystal slabs. The intensity variations in diffracted beams, as functions of incidence angle, were measured and verified against theory. It was possible to detect carbon nanofiber actuation using both methods on the tunable samples and results are compared to theoretical expectations. The results from static and tunable structures are compared.

Finally, possible extensions and applications of the devices are discussed.

---

**Keywords:** Photonic crystal, carbon nanofiber, tunable, FDTD, diffraction, PECVD, ellipsometry

---

# Ställbara fotoniska kristaller baserade på kolnanofibrer

Robert Rehammar

Institutionen för Teknisk Fysik  
Chalmers Tekniska Högskola

## Svensk sammanfattning

Fotoniska kristaller är material med periodiskt varierade brytningsindex. Vid konventionell design av fotoniska kristaller är det svårt att åstadkomma ställbara strukturer inom det synliga frekvensområdet, dvs. strukturer med ställbara optiska egenskaper.

Kolnanofibrer har ungefär samma dimensioner som kolnanotuber med flera väggar, men med den fördelen att de kan tillverkas vertikalt fristående. I detta arbetet undersöks möjligheten till att använda kolnanofibrer som byggstenar i ställbara två-dimensionella fotoniska kristaller. Genom att växa kolnanofibrer i ett gitter och placera närliggande fibrer på olika elektrisk potential, kan nanofibrerna böjas elektrostatiskt. Detta modifierar gittret, vilket i sin tur påverkar de optiska egenskaperna.

En finit-differens-tids-domänmetod har använts för att modellera en fotonisk kristall med ställbar bas. Det visades att optiska transmissionen genom ett finit fotonisk-kristallsystem kan ändras från nästan 100% till ca 1% med bara några få rader nanofibrer i utbredningsriktningen. Man fann också att många av egenskaperna i transmissionspektret kunde relateras till bandstrukturen hos den fotoniska kristallen.

Både statiska och ställbara kolnanofiber-baserade fotoniska kristaller har tillverkats i en DC-plasmaförstärkt CVD-process (chemical vapour deposition-process). En optisk mätuppställning har konstruerats och använts för att undersöka diffraktion från proverna. Proverna undersöktes också med ellipsometri.

Man fann att ellipsometri är en kraftfull metod för att undersöka bandstrukturen hos 2D fotoniska kristaller. Intensitetsvariationer i diffrakterade strålar som funktion av infallsvinklar mättes och verifierades mot teori. Det var möjligt att detektera elektrostatiska kolnanofiber-deformationer med båda teknikerna på de ställbara proverna. Resultat från dessa mätningar jämförs med teori. Resultaten mellan statiska och ställbara strukturer jämförs.

Slutligen diskuteras möjliga tillämpningar och utvidgningar av projektet.

---

## Research publications

This thesis is an introduction to and summary of the work published in the following research articles, referred in the text as Papers I-IV.

**Paper I** R. Rehammar and J. M. Kinaret, *Nanowire-based tunable photonic crystals* Optics Express **16**, 21682-21691, 2008.

**Paper II** R. Rehammar, R. Magnusson, A. I. Fernández-Domínguez, H. Arwin, J. M. Kinaret, S. A. Maier, E. E. B. Campbell, *Optical properties of carbon nanofiber photonic crystals*, Nanotechnology, **21**, 465203, 2010.

**Paper III** R. Rehammar, Y. Francescato, A. I. Fernández-Domínguez, S. A. Maier, J. M. Kinaret, E. E. B. Campbell, *Diffraction from carbon nanofiber arrays*, Optics Letters, **37**, 100-102, 2012.

**Paper IV** R. Rehammar, F. Alavian Ghavanini, R. Magnusson, J. M. Kinaret, P. Enoksson, H. Arwin, E.E.B. Campbell, *Carbon Nanofiber Tunable Photonic Crystal*, submitted to Small

The articles are appended in the end of the thesis.

## Related publications by the author not included in the thesis

1. J.M. Kinaret, R. Rehammar and E.E.B. Campbell, *Tunable photonic crystal using nanostructures*, Patent application, **WO2008SE50221**, 2008
2. R. Rehammar, R. Magnusson, A. Lassesson, H. Arwin, J. M. Kinaret, and E. E. B. Campbell, *Carbon Nanofiber-Based Photonic Crystals - Fabrication, Diffraction and Ellipsometry Investigations*, MRS Online Proceedings Library, **1283**, 2011.

---

# Contents

<b>1</b>	<b>Introduction</b>	<b>1</b>
1.1	Photonic crystals . . . . .	1
1.2	Carbon nanofibers . . . . .	5
1.3	A tunable carbon nanofiber-based photonic crystal . . . . .	6
1.4	Thesis overview . . . . .	7
<b>2</b>	<b>Background theory</b>	<b>11</b>
2.1	Waves in periodic media . . . . .	12
2.2	Diffraction from a two dimensional surface . . . . .	16
2.3	Polarised light . . . . .	18
2.4	Surface Plasmon Polaritons . . . . .	19
2.5	Properties of carbon nanofibers . . . . .	19
<b>3</b>	<b>Modelling methods</b>	<b>23</b>
3.1	Transfer matrix method . . . . .	23
3.2	Plane wave expansion . . . . .	24
3.3	Finite-difference time-domain method . . . . .	25
<b>4</b>	<b>Carbon nanofiber fabrication</b>	<b>31</b>
4.1	Selecting metal underlayer . . . . .	32
4.2	Growth conditions . . . . .	32
<b>5</b>	<b>Measurements</b>	<b>37</b>
5.1	Diffraction . . . . .	37
5.2	Ellipsometry . . . . .	43
<b>6</b>	<b>Introduction to and summary of appended papers</b>	<b>45</b>
6.1	Paper I – Nanowire-based tunable photonic crystals . . . . .	45
6.2	Paper II – Optical properties of carbon nanofiber photonic crystals . . . . .	61
6.3	Paper III – Diffraction from carbon nanofiber arrays . . . . .	64
6.4	Paper IV – Carbon Nanofiber Tunable Photonic Crystal . . . . .	68
<b>7</b>	<b>Conclusions and outlook</b>	<b>75</b>
7.1	Conclusions . . . . .	75
7.2	The work seen in retrospect . . . . .	75
7.3	An outlook . . . . .	76
	<b>Acknowledgements</b>	<b>79</b>
<b>A</b>	<b>Substrate processing</b>	<b>81</b>

## Abbreviations and symbols

### Abbreviations used in the thesis

BZ	Brillouin zone
CNF	Carbon nanofiber
CNT	Carbon nanotube
DC-PECVD	Direct current plasma enhanced chemical vapour deposition
DOS	Density of states
FDTD	Finite-difference time-domain
FEM	Finite elements method
LDOS	Local density of states
ME	Maxwell's equations
MEMS	Micro-electro-mechanical system
NEMS	Nano-electro-mechanical system
NOEMS	Nano-optical-electro-mechanical system
PEC	Perfect electric conductor
PC	Photonic crystal
SEM	Scanning electron microscope
PML	Perfectly matched layer
SMU	Source measure unit
SPP	Surface plasmon polariton
VACNF	Vertically aligned CNF

### Symbols used in the thesis

$a$	Lattice constant
$\mathbf{a}_i$	Lattice vector
$\lambda$	Wavelength
$\omega$	Angular frequency
$\mathbf{k}$	Wavevector
$c$ and $c_0$	Speed of light and speed of light in vacuum respectively.
$\varepsilon = \varepsilon_1 + i\varepsilon_2$	Relative dielectric function. $\varepsilon_0\varepsilon(\omega)\mathbf{E}(\omega) = \mathbf{D}(\omega)$ .
$N = n + ik$	Complex refractive index. $n$ is the real refractive index and $k$ is the extinction coefficient. $N$ is related to $\varepsilon$ via $N^2 = \varepsilon$ .
$\mathbf{G}$	Reciprocal Lattice Vector
$\Theta_{\text{in out}}$	Polar angle of incoming and exiting light beam. Measured from the $z$ -axis
$\nu_{\text{in out}}$	Azimuthal angle of incoming and exiting light beam. Measured from the $x$ -axis.
$\alpha_{\text{in out}}$	Angles measured in the diffraction set-up that relates to polar angles.
$\phi_{\text{in out}}$	Angles measured in the diffraction set-up that relates to azimuthal angles.

# Chapter 1

## Introduction

Nanotechnology – the technology of manipulation in the nanometre range – is emerging as the technology of the 21st century, providing openings for truly new applications in medicine, engineering, electronics and optics. As dimensions are shrunk to nanometer size, several new phenomena become available for exploration and quantum physics starts to come into play. This thesis describes a particular device — a photonic crystal. This PC operates in the visible spectrum of light, and hence the typical dimensions of its parts are in the range of the wavelength of visible light, 400 - 750 nm. The building material used for the PC reported here is one of the core structures of the "nano era" – the carbon nanofiber.

Nanoelectromechanical systems, NEMS, are artificially created systems where electrical and mechanical degrees of freedom are coupled on the nanometre scale. NEMS can to some degree be regarded as a natural continuation of MEMS - microelectromechanical systems, which today have a natural place in the gadget jungle providing *e.g.* gyroscopes and accelerometers in smartphones. When also optical phenomena, that is, electromagnetism with frequencies in the 100 THz range, play a relevant part, an 'O' is added in the NEMS abbreviation, giving NOEMS. The systems investigated in this work could be classified as NOEMS; optical, electrical and mechanical degrees of freedom all play a part in the systems operation. On the other hand, as will be seen, not all of these are dynamically coupled, so it could be argued that the systems investigated are not proper NOEMS, but rather NEMS, probed by optical techniques.

In this thesis two concepts; photonic crystals and carbon nanofibers are brought together to provide new kinds of structures that can control light on the nanometer scale in new ways. I will now introduce these two main concepts.

### 1.1 Photonic crystals

In physics, a lattice is a structure which is periodic. The period is the smallest separation between two points from which the structure looks identical. If a one-dimensional problem is considered this distance is denoted  $a$ , if the structure is in more than one dimension these are known as the fundamental lattice vectors, denoted  $\mathbf{a}_i$ . Periodic structures in general provide a very rich spectrum of phenomena and applications. Regular *crystals* are atoms or molecules placed in a periodic pattern [1]. Hence, effects stemming from periodicity are fundamental in understanding ordinary solids.

A PC is a material slab (in theory infinite) where there is a periodicity in the material parameter, most often the dielectric constant,  $\varepsilon$ , in one, two or three dimensions. The periodicity is defined by the lattice vectors which have magnitudes of the order of some relevant electromagnetic radiation's wavelength,  $\lambda \sim |\mathbf{a}_i|$ , usually in the visible, but not necessarily. Technical applications often work in the infra red.

It is amazing how rich spectrum of phenomena emerges from such a simple definition. First, the peculiar scattering phenomena of diffraction appear which will be discussed in great detail in later chapters. Next, if wave propagation within the structure is considered, there are several exciting phenomena to mention such as a photonic bandstructure, which might exhibit bandgaps [2]. PCs have been shown to experience negative refraction [3, 4, 5] and super prism [6] effects in certain situations. There have been PC designs where ultra-high Q-factors in  $\lambda$ -sized cavities have been achieved [7], as well as ultra-confined waveguiding [8] and lasing [9, 10, 11]. Finally, strong localisation of light has been demonstrated in disordered structures [12].

There are several excellent introductions to PCs, in particular the book by Joannopoulos [13], which can also be freely downloaded from the internet. A more advanced treatment is given by Sakoda [14], covering group theory and introducing many of the computational tools used to analyse PCs. Inoue [15] puts the focus on experimental methods and fabrication. Long before the ideas of photonic crystals were sprung, the excellent and easily accessible book by Brillouin (one of the fathers of the theory of periodic structures) was published [16], covering to a very detailed degree wave propagation in periodic structures. Finally, a book covering modern concepts is the one by Sibilina [17].

## The birth of photonic crystals

The birth of the concept of PC is usually dated to two seminal papers published in 1987 by Yablonovitch [2] and John [18]. Both these papers focus on how periodic structures can be used to strongly localise electromagnetic radiation. There are however much earlier investigations [19] of structures that could also be described as photonic crystals. Before Yablonovitch and John's work however most focus was on systems with dimensionality lower than three. This was mainly because of fabrication issues with 3D structures, but also because the radical consequences of the periodicity realised by Yablonovitch and John were not fully appreciated before. After the works by Yablonovitch and John the interest in PCs exploded. In 1996 Krauss fabricated the first two-dimensional PC, with a full band gap (BG) in the optical regime Krauss [20].

Even though PCs are relatively new within science they are in no way a new phenomenon in nature. Opals get their beautiful colours from nano-spheres assembled to form PCs, see figure 1.1(a). Many insects such as butterflies and beetles do not use any pigment to achieve their shiny exterior but rather have a kind of microscopic periodicity on their surface that causes colourful reflections, see figure 1.1(b).

## Different periodic structures

In radio and microwave engineering, (two dimensional) antenna arrays are used. Simple antenna elements are placed in regular arrays to achieve enhancement in antenna characteristics [23]. A related concept is that of frequency selective surfaces that are used in

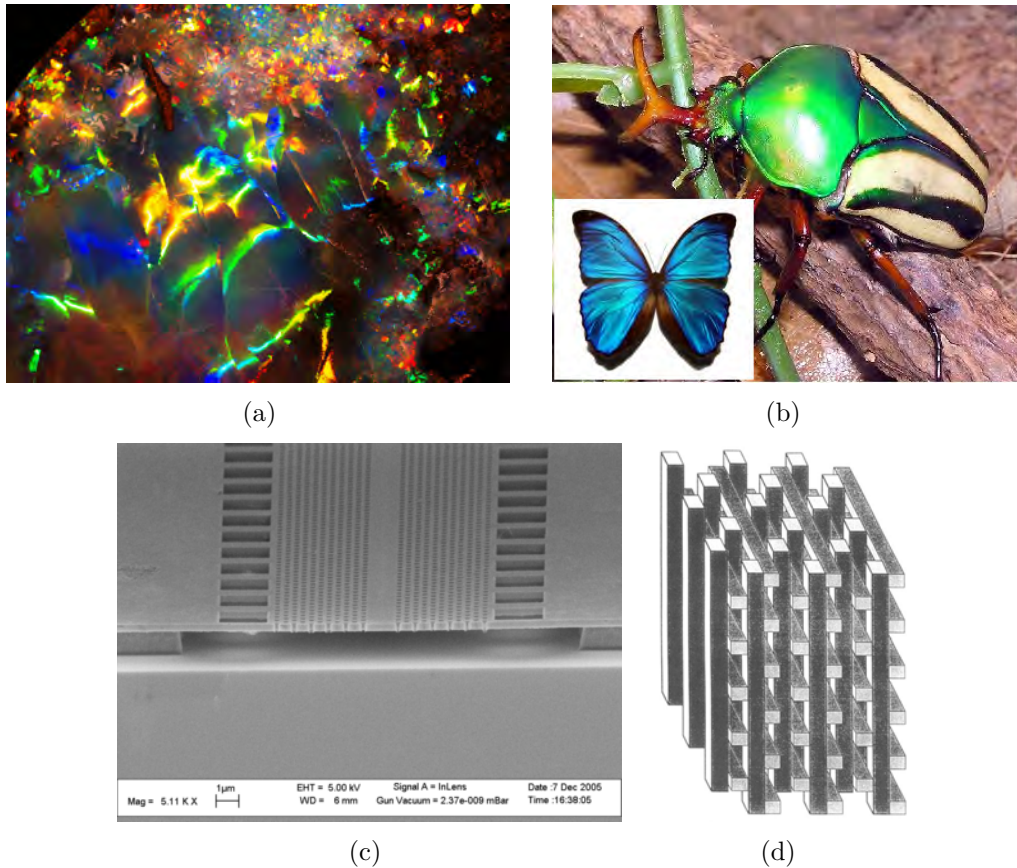


**Figure 1.1:** (a) A PC consisting of small spheres auto-assembled to form an opal, (b) insects show high reflectance and colourful parts stemming from PCs. Images from Wikipedia. (c) A GaAs-based 2D PC slab with a dislocation, reproduced from [21]. (d) Sketch of the woodpile PC structure, reproduced from [22].

microwave engineering to control the scattering cross section of objects [24].

Moving down in dimensionality to one dimensional structures, there are anti reflection coatings where layers of dielectrics with different refractive indices are stacked on top of each other to reduce reflections on e.g. windows or lenses [25]. Bragg-mirrors are another example where a dielectric stack is used, now instead to enhance reflections. These are of fundamental importance in modern micro-lithography where the wavelength of the exposure light is now in the deep UV, rendering regular metallic mirrors useless. In spectrometers, diffraction gratings, which are one-dimensional periodic structures, are used to separate wavelengths before the light hits a photon counter, typically a charge-coupled device.

In addition to the classically periodic structures discussed above, there are also quasi-crystals: systems with a deterministic structure, but non-periodic [26, 27]. Their discovery led to the award of the Nobel prize in chemistry in 2011 to Shechtman [28]. There are several studies of quasi-crystalline PCs as well, e.g. by Chan and Kaliteevski [29, 30].

PC also have high potential as different type of sensors. Xu and co workers demonstrated [31] a two-dimensional PC cavity used for refractive index measurement of fluids. They showed a 3.5 nm resonance shift for a refractive index change of 0.01.

Commercial applications of PCs of dimension higher than one are few. One of the oldest applications is probably the application of one-dimensional layered structures that are used as antireflection coatings, mentioned above. Another example, in this case of a two dimensional system, is optical fibres, also called crystal fibres, which use a PC-structure with a dislocation to guide light within the bandgap with low losses. These fibres are generally single mode and quite expensive.

One of the most exciting routes of PCs is the possibility to use them as integrated devices for on-chip optical components. With the possibility to provide light confinement of the size of the wavelength (typically  $\lambda \simeq 1 \mu\text{m}$ ) PCs open up for the possibility of replacing on-chip communication mediated via electrons as used in today's integrated electronics by photon-mediated communication [32]. This is due to their ability to confine and guide light around very sharp corners (corners with curvature of the order of the wavelength of the radiation) [8]. Therefore it has been suggested that future multiple-core processors where each core works as a conventional micro-electronic processor, should perform the inter-core communication by optical means, providing low losses and extreme bandwidth.

It is interesting to compare PCs with regular crystalline solids. In a PC, the wave equation that governs the dynamics concerns photons, while in regular crystals it is the electrons that play the corresponding role. Photons are bosons, and hence in PCs there is no Fermi level as in regular crystals with fermions. Also light has the property of being polarised, an effect that does not appear for electrons. It turns out that it is very important to take polarisation into account when discussing the optical behaviour of PCs. Another important difference is that in a regular crystal, the electrons are confined to the structure while a PC, at least in most situations, does not confine light in the sense that a PC slab contains photons permanently. Instead, when working with PCs, it is central to take into account how light enters and exits the structure.

## A note on dimensionality

In general we live in three-dimensional space. This means there are three mutually orthogonal directions for us to move in. In the setting of the work presented in this thesis there is no ambiguity about what is meant by three dimensions. Going to "two-dimensional" systems however, there are two opposite extreme cases, both denoted "two-dimensional". On the one hand imagine a geometry, here typically defined by the dielectric constant  $\varepsilon = \varepsilon(\mathbf{r})$ , where there is no variation in one spatial dimension, say the  $z$ -dimension. Hence  $\varepsilon = \varepsilon_{\parallel}(x, y)$ . If propagation in the  $(x, y)$ -plane is considered, the system possesses a mirror-symmetry in that plane which can be used to classify the modes according to the symmetry [33]. In the other extreme case of "two-dimensionality", the dynamics under consideration is constrained to a two dimensional surface. Typically this is the situation with wave-guiding in the plane. Then  $\varepsilon = \varepsilon(\mathbf{r})$ , but the  $z$ -dimension is special in that large parts of it are not accessible for the dynamics. It might e.g. be the case that

$$\varepsilon = \begin{cases} \varepsilon(x, y, z), & |z| < z_0 \\ -\infty, & \text{otherwise,} \end{cases}$$

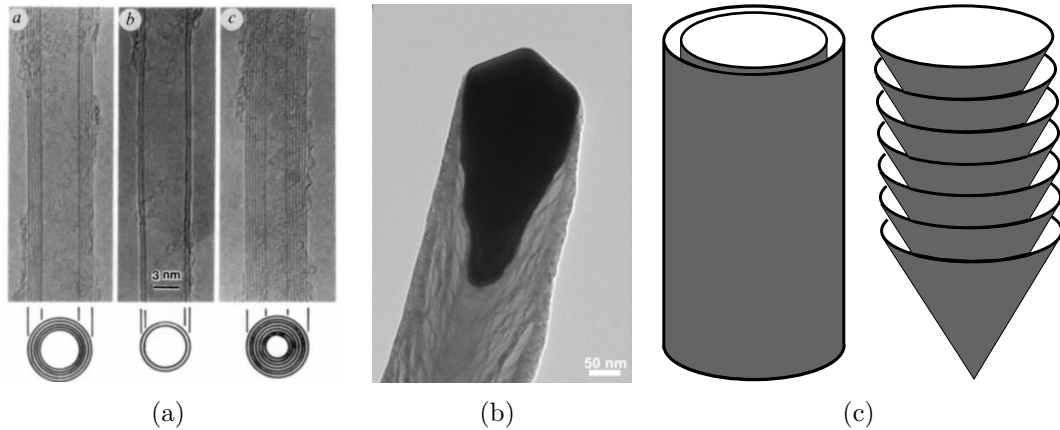


**Figure 1.2:** (a) TEM image of CNTs, reproduced from [34] (b) TEM image of CNF with the catalyst particle visible as a dark region in the tip, reproduced from [38] and (c) a sketch of a double walled CNT (CNF) to the left (right).

corresponding to space outside  $|z| < z_0$  being filled by a perfect metal. Typically a relation like

$$z_0 \lesssim \frac{c}{\hat{\epsilon}f}, \quad (1.1)$$

where  $f$  is the frequency light in the situation and  $c$  is the speed of light, holds.  $\hat{\epsilon}$  is a representative dielectric constant of the system, e.g.

$$\epsilon = \begin{cases} \hat{\epsilon}, & |z| < z_0 \\ -\infty, & \text{otherwise.} \end{cases}$$

The requirement in equation (1.1) represents a case where only one or a few modes exist in the vertical direction. These can then be treated as separate channels which are well separated in energy and the dynamics is individually explored in the  $(x, y)$ -plane for each mode. The PCs investigated in this work are of this last type where there is variation in the  $z$ -dimension, but we are mainly interested in the in-plane dynamics. Often such PC systems are denoted PC slabs in the literature.

## 1.2 Carbon nanofibers

The second main constituent of the work presented in this thesis consists of carbon nanofibers, CNFs. They are closely related of *the* nano material: carbon nanotubes. The discovery of CNTs is somewhat disputed (as probably most great discoveries are) but it is common to attribute it to Iijima [34], though there are several prior publications and patent applications on CNTs and CNFs [35, 36, 37].

In figure 1.2 TEM images depict CNTs (a) and CNFs (b). A CNT is one or a few layers of graphene rolled up to form a tube. Graphene is a single layer of the regular form of carbon, graphite. If the CNT consists of a single sheet of graphene it is usually called single-walled and if two or more layers are present it is instead denoted multi-walled. In CNFs the tubular shape of CNTs is replaced by conical graphene sheets, stacked to form a cylinder. The cones can be cut off at the tip, creating a void in the middle, see

figure 1.2(b), or as depicted in figure 1.2(c) where the cone ends up in a tip, creating a completely filled cylinder. The tilt angle of the cone varies depending on fabrication conditions, and a tilt angle of  $0^\circ$  correspond to a CNT.

Due to an important property of CNFs they have been deployed in the present work in favour of CNTs: CNFs can be fabricated vertically free-standing<sup>1</sup>, not requiring any sideways support, see e.g. figure 1.4. There have been claims that also CNTs can be fabricated vertically aligned without support, but the author has not seen any proofs of this. A recent review of aligned CNTs and CNFs covering both fabrication and application aspects can be found in the paper by Lan [39].

## Photonics with carbon nanofibers

There has been much work on optical properties of CNTs. This will not be reviewed here, but is considered to be outside the scope of this thesis. There are a number of papers on photonics with CNFs. VACNFs have been used as building blocks of PCs which have been studied using diffraction [40, 41]. Arrays of VACNFs were also viewed as optical antennas [42, 43], an intensively studied subject at the moment [44]. CNF arrays have been used as building blocks of metamaterials for plasmonics [45]. A theoretical study of CNT-based PCs for energies higher than the visible was reported by Lidorikis [46].

## 1.3 A tunable carbon nanofiber-based photonic crystal

Within semiconductor physics it is well known that dislocations and impurities cause new modes to be available in the system. This is often undesired as it changes the microscopic properties in an uncontrolled way. But it is also used, e.g. when intentional doping is done to obtain a desired electron density. In PCs, similar things can be achieved by modifying some scatterers in a lattice. Doing this can create e.g. cavities and/or waveguides. These "doping" schemes however in general result in static structures that are not possible to modify after fabrication. Thus a structure similar to a semiconductor transistor, which can be turned "on" and "off" electronically, can not be fabricated with this simple scheme. The work in this thesis represents one attempt to remedy this limitation.

When talking about a particular system, the ability of this system to be tuned during operation is (of course) in many situations a desirable property. In the nano-world, systems are commonly denoted as tunable if there is a parameter that can be changed which results in a change in the systems transfer function. For example, the length of a resistive wire could be varied to change the resistance of the wire as a whole. This makes the "wire based resistor" tunable in the sense that we can cut the wire to a length that gives a desirable resistance for our particular application. However, the tunability is limited. Once the wire is cut, there is no obvious way to increase the resistance of the resistor. The system possesses tunability in a static sense. This could also be described as the system being "designable".

In a way similar to the resistor example above, there are parameters  $\{a_i\}$  of a PC that directly control the optical properties of the PC. By varying these it is possible to

---

<sup>1</sup>It is common to talk about vertically aligned carbon nanofibers, VACNFs. In this work only vertically aligned CNFs are of interest, and hence the terms CNF and VACNF are used interchangeably.

design the PC; vary  $a_i$  and hence change what wavelength range it operates within.<sup>2</sup> However, it is not easy to modify size the shape of a structure once it has been fabricated. Thus, there are often several ways to tune a system to a particular response by design in the fabrication process. But it is considerably more challenging to have a dynamical way of changing the response based on some dynamical parameters such as temperature or applied field.

There have been several efforts to make PCs tunable in the dynamical sense. In particular, tunability at optical frequencies is desirable from an application point of view. The potential for this kind of device is very large: optical tunable filters and other active optical components are examples. In [47] Liu and co-workers use liquid crystals to modify the bandgap of a three-dimensional photonic crystal, in [48] Wu and co-workers use mechanical deformation to achieve a tunable super-lens and in [49] Furumi report on lasing in a colloidal-based deformable PC. In [50] Rajic and co-workers use a microelectromechanical system (MEMS) to deform a photonic crystal in a waveguide to create a tunable filter. Also all-optical tuning has been suggested, e.g. by Alkeskjold [51]. Very fast all-optical tuning was recently reported by Euser [52] where the so-called woodpile structure was used and in [53] where Fushman and co-workers achieve tuning via non-linear effects in GaAs. Finally, in [54] Vlasov *et al.* use heat to control light propagation and also in [55] heat is used to switch light in a PC device. The majority of the papers published about tunable PCs use liquid crystals to achieve the tuning. All the different techniques have different drawbacks such as high energy consumption, non-repeatability, very slow operation or complicated/impossible fabrication. The present work tries to address some of these issues.

One way to achieve tunability of a PC is to deform the geometry of the lattice. The idea investigated in the work presented here is to place nanowires, in particular VACNFs, on electrodes in a lattice. By contacting the CNFs they can be electrostatically actuated by applying a voltage difference. The actuation is a deformation of the lattice and could hence be used to modify the optical properties. A schematic picture displaying this idea is presented in figure 1.3.

Many versions of the structure can be imagined, opening up for tunable cavities, tunable waveguides and filters. These applications and others are covered in a patent referenced in additional publications in the publication list. In this work however the basic system illustrated in figure 1.3, but without waveguides, and depicted in figure 1.4 is the only version realized and investigated. Other realisations are left for future work. This type of electrostatic actuation has been demonstrated before in purely electrical devices [56, 57].

## 1.4 Thesis overview

In addition to this introductory chapter, there are six more chapters in the thesis. In chapter 2 the framework for discussing PCs from a theoretical point of view is set up based on Maxwell's equations. It is primarily a review chapter. In chapter 3, the computational modelling methods used in this work to model PCs and investigate optical properties of

---

<sup>2</sup>A PC could almost be described as a scaled up regular crystal. Hence, *tuning* the lattice constant could be said to be the very idea behind PCs in the first place.

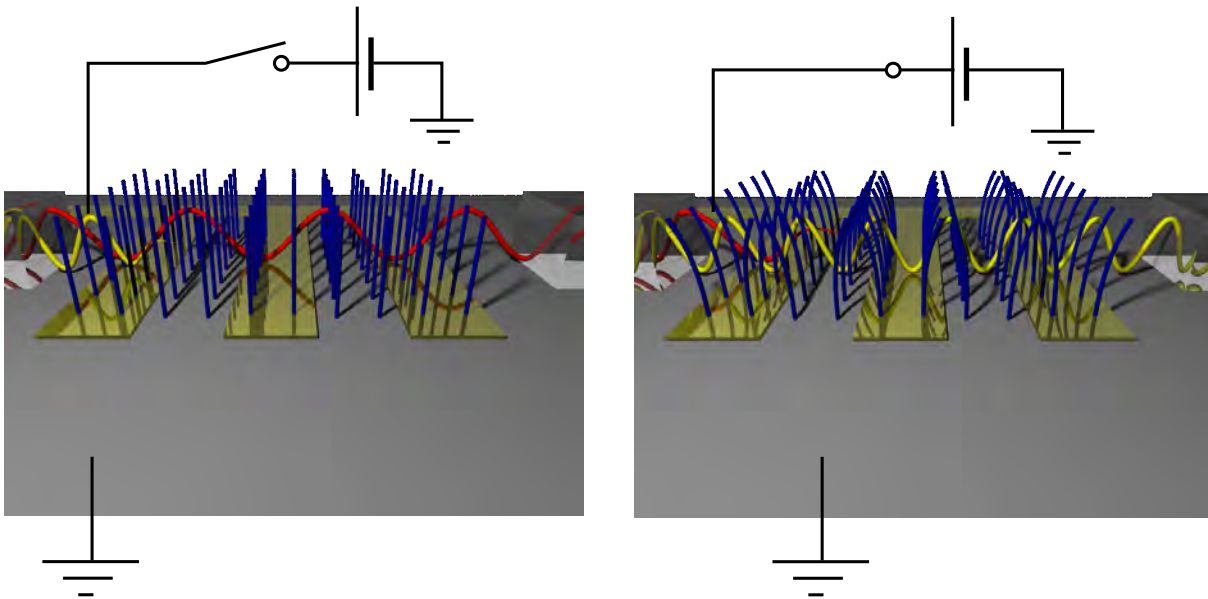


**Figure 1.3:** A sketch of how a system built on the idea behind the tunable PC studied in this thesis could look. To the left the system without any voltage applied. In the far left on the figure is seen a waveguide guiding light of two colours. Due to the structure of the PC, only the red light can pass through and continue on to the collecting waveguide to the right in the picture. The yellow light is damped out. To the right is the same system, now with a voltage applied. The nanowires (in this work VACNFs) actuate from capacitive forces and the changed structure now makes yellow light pass without damping through the PC while red light is damped out. A set-up like this could be thought of as an opto-mechanical switch.

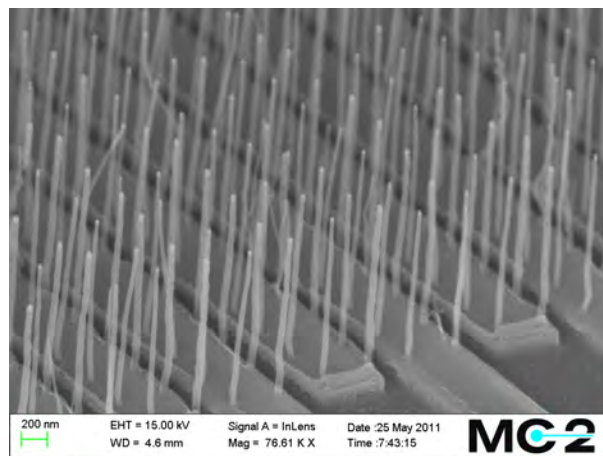


**Figure 1.4:** SEM micrograph of a realisation of the system described in figure 1.3.

the same are described. Chapter 4 is dedicated to descriptions of the fabrication methods used to fabricate VACNFs, excluding clean room work which is placed in an appendix. Chapter, 5 describes the measurement set-ups used in the optical characterisation of the fabricated PCs. This includes diffraction measurements which were developed by me and ellipsometry measurements which use a commercial tool. In chapter 6 the results are presented in the form of introductions and summaries of the papers that have been published during the work. The thesis ends with chapter 7 concluding and discussing future possible directions.

Paper I covers a theoretical study on the possible functioning of a tunable CNF-based PC. A simplified, non-tunable, version of the system presented in Paper I was studied theoretically and experimentally in Papers II and III. In Paper IV, measurements on a tunable CNF-based 2D PC slab were presented.



# Chapter 2

## Background theory

The foundation for analysis of electromagnetic phenomena in general and PCs in particular is Maxwell's equations (ME). In the time domain these can be written as [58]:

$$\begin{aligned}\nabla \cdot \mathbf{D} &= \rho \\ \nabla \cdot \mathbf{B} &= 0 \\ \nabla \times \mathbf{H} - \frac{\partial \mathbf{D}}{\partial t} &= \mathbf{J} \\ \nabla \times \mathbf{E} + \frac{\partial \mathbf{B}}{\partial t} &= 0,\end{aligned}\tag{2.1}$$

where  $\mathbf{E}$  and  $\mathbf{H}$  are the electric and magnetic fields respectively. The sources in the equations are  $\rho$  and  $\mathbf{J}$ ; the free electric charge and free current density. For linear, isotropic media the electric displacement field  $\mathbf{D}(\omega)$  is linearly related to the electric field  $\mathbf{D}(\omega) = \varepsilon_0 \varepsilon(\omega) \mathbf{E}(\omega)$  where  $\varepsilon(\omega)$  is the relative dielectric constant.<sup>1</sup> Similarly the magnetic induction,  $\mathbf{B}$ , is related to the magnetic field by  $\mu_0^{-1} \mu^{-1}(\omega) \mathbf{B}(\omega) = \mathbf{H}(\omega)$ , where  $\mu$  is called the relative permeability.

ME constitute a set of equations completely describing electromagnetic phenomena and, if the Lorentz force law is added, also how electromagnetic fields interact with matter. They are extremely rich in nature, and in many situations it is not possible to solve them analytically.

Usually the equations in (2.1) are named, in order of appearance: Gauss's law, absence of magnetic monopoles, generalised Ampère's law and Faraday's law of induction. This is how they will be referred to in the text.

The form of ME, as written in equation (2.1), is called macroscopic because of the appearance of the two macroscopic fields  $\mathbf{D}$  and  $\mathbf{H}$ . As stated above they depend on the electric and magnetic fields respectively, but also on the material functions  $\varepsilon$  and  $\mu$ . Hence, to use the macroscopic ME it has to be possible to define  $\varepsilon$  and  $\mu$ . The forms of these two functions are derived from microscopic considerations of the materials involved in the particular problem averaged over a small volume. When working with PCs, usually the macroscopic ME are used. That is to say, the wavelength of interest is much longer than the atomic radius so we can sensibly use dielectric functions that vary in space to

---

<sup>1</sup>Note that this multiplicative relation holds in the frequency domain. If moving to the time domain, this product is transformed into a convolution.

describe material changes from one place in space to another. At optical frequencies, in most materials  $\mu$  does not vary substantially from the behaviour in vacuum, so it can be set to unity. Indeed, this is the case for CNFs and the other materials considered in this work<sup>2</sup> [58]. The form of the dielectric constant in PC will be discussed further in the coming sections.

In the next few pages a review of concepts related to electromagnetic waves is presented. All these concepts are used further on in the thesis and in the papers when discussing properties of the VACNF-based PCs. The focus is on simple examples that illustrate the aspects which will later be generalised to fit in the context of PCs. After these, there is a section on diffraction theory which is used in Papers III and IV for characterising the PCs. Then follows a section on ellipsometry which is a particular technique used in Papers II and IV, also for optical characterisation. The chapter ends with a short discussion on a few properties of CNFs which are of importance.

## 2.1 Waves in periodic media

A central property of ME is that they can support waves<sup>3</sup>. Consider the vacuum where Gauss's law takes the form  $\nabla \cdot \mathbf{E} = 0$ . Further, there are no currents, so we have  $\mathbf{J} = 0$ . Also

$$\frac{\partial \mathbf{D}}{\partial t} = \varepsilon_0 \frac{\partial \mathbf{E}}{\partial t}.$$

Now the curl of Ampère's law gives

$$\nabla \times [\nabla \times \mathbf{H}] = \nabla(\nabla \cdot \mathbf{H}) - \nabla^2 \mathbf{H} = -\nabla^2 \mathbf{H} = \varepsilon_0 \frac{\partial \nabla \times \mathbf{E}}{\partial t},$$

where the facts that there are no magnetic monopoles and  $[\nabla \times, \frac{\partial}{\partial t}] = 0$  have been used. Using Faraday's law to replace  $\nabla \times \mathbf{E}$  gives the equation

$$\nabla^2 \mathbf{H} = \frac{1}{c^2} \frac{\partial^2 \mathbf{H}}{\partial t^2}, \quad (2.2)$$

where  $\varepsilon_0 \mu_0$  has been replaced by  $1/c_0^2$ ,  $c$  being the speed of light. If polarisation and frequency is assumed to be  $\mathbf{H} = [h, 0, 0]e^{i\omega t}$  equation (2.2) is transformed to

$$\frac{d^2}{dx^2} h + \frac{\omega^2}{c_0^2} h = 0, \quad (2.3)$$

<sup>2</sup>There is however one thing that should also be considered here, and that is that the catalyst particle, situated in the top of the CNF, is made of Ni, which is a ferromagnetic material. As such it is not a linear material which invalidates the whole description with the permeability function.

<sup>3</sup>Generally a wave equation is a first order system of differential equations where the differential operator of space coordinates,  $D$ , is anti-hermitian:

$$\frac{\partial \mathbf{w}}{\partial t} = D\mathbf{w} + \mathbf{s}.$$

$\mathbf{w}$  denotes the field and  $\mathbf{s}$  the source term. This can be considered the definition of a wave equation and ME, the Schrödinger equation and other well known wave equations in physics can be written in this form [59].

## 2.1. Waves in periodic media

---

which has a general solution

$$h(x) = Ae^{ikx} + Be^{-ikx},$$

with  $k^2 = \omega^2/c_0^2$  and where  $A$  and  $B$  are arbitrary constants. Equation (2.3) is the Helmholtz equation in one dimension. The constants are set by the boundary conditions, e.g. a right moving wave with unit amplitude and phase 0 will have  $A = 1$ ,  $B = 0$ .

### The dispersion relation

A general travelling scalar wave (in a non-dispersive medium) has the form

$$f(kx - \omega t),$$

where  $f$  is any function,  $x$  and  $t$  are space and time coordinates respectively,  $k$  and  $\omega$  are constants relating space and time and are denoted wavevector and frequency. Usually time dependence is harmonic; e.g. as seen in the previous section with  $f(x) = e^{ix}$ . Typically  $k$  and  $\omega$  are not free to take any value. In the previous section it was seen that in vacuum

$$k(\omega) = \frac{\omega}{c_0}.$$

This is an example of a dispersion relation, relating the wavevector  $k$  to the frequency  $\omega$ . Different wave equations give rise to different dispersion relations. These are of great interest since they control many properties of the wave. As an example, the propagation speed of a wave package (the group velocity) is [60]:

$$v_g = \frac{d\omega}{dk}. \quad (2.4)$$

The form of the dielectric function  $\varepsilon$  has great influence on the dispersion relation. As will be seen, in PCs  $\varepsilon$  takes a particular form, shaping the dispersion relation to have several important and unique properties.

### The refractive index

The speed of a propagating electromagnetic wave in a medium is denoted  $c$ . For a linear, non-dispersive, homogeneous, isotropic, source-free medium it is

$$c = \frac{1}{\sqrt{\varepsilon_0 \varepsilon \mu_0 \mu}}.$$

The refractive index of a material is defined as

$$n = \frac{c_0}{c} = \sqrt{\varepsilon \mu},$$

where  $c_0$  is the speed of light in vacuum. The refractive index controls reflections at interfaces between materials with different  $\varepsilon$  and  $\mu$ . It appears in the Fresnel equations for the reflection coefficients [61] and will be discussed in connection to PCs in the ellipsometry works of Papers II and IV.

## Wave propagation in periodic media

An (electromagnetic) medium is periodic<sup>4</sup> in space if

$$\varepsilon(\omega, \mathbf{x}) = \varepsilon(\omega, \mathbf{a}_i + \mathbf{x}) \quad (2.5)$$

holds for all positions  $\mathbf{x}$  and a set of fixed vectors  $\{\mathbf{a}_i\}$ . In solid state physics it is well known that waves propagating in periodic media obtain a particular form, known as Bloch waves. This name comes from a theorem proved by Bloch which is a special case of Floquet's theorem [16, 62]. In the one dimensional case, Bloch's theorem says that any solution to the wave equation

$$\left( \frac{d^2}{dx^2} + f(x) \right) E(x) = 0, \quad (2.6)$$

where  $f(x) = f(x + a)$  for some constant  $a$  and all  $x$ , has the form

$$E_{k,n}(x) = u_{k,n}(x)e^{inkx}. \quad (2.7)$$

Here  $n$  is an integer numbering the solutions and  $k \in [-\pi/a, \pi/a]$  is the Bloch wavevector. The function  $u_{k,n}(x)$  has the same periodicity as the potential. There is an infinite number of solutions, meaning here  $n \in [1, \infty)$ . The Bloch wavevector is not an ordinary wavevector – it appears in the extra function  $u_{k,n}$  which makes the Bloch mode  $E_{k,n}$  differ from a regular plane wave, but it is something quite similar.  $E_{k,n}$  is an eigenstate of the discrete translation operator associated with the lattice,  $T$ , defined by:

$$Ty(x) = y(x + T).$$

Operating on  $E_{k,n}$  with  $T$  yields

$$TE_{k,n} = e^{inkT} E_{k,n}$$

and  $e^{inkT}$  is the eigenvalue. Hence  $k$  (and  $n$ ) numbers the eigenvalues in a fashion similar to the regular wavevector for the plane wave case.

In two and three dimensions the Bloch wave in equation (2.7) becomes

$$E_{\mathbf{k},n}(\mathbf{x}) = u_{\mathbf{k},n}(\mathbf{x})e^{i\mathbf{k}\cdot\mathbf{x}}. \quad (2.8)$$

Equation (2.8) is the basis for analysis in later chapters when dealing with the band structure of CNF-PCs.

## The reciprocal lattice

The periodic function in equation (2.5) comes from the arrangement of different (dielectric) materials. In the present case, VACNFs are placed in a rectangular pattern so that there are CNFs standing with their centres at each point

$$\mathbf{p}_{m,n} = (ma_x, na_y) = m\hat{a}_1 + n\hat{a}_2. \quad (2.9)$$

<sup>4</sup>We still assume  $\mu$  is not different for the vacuum anywhere.

## 2.1. Waves in periodic media

---

In this expression  $a_x$  and  $a_y$  are the lattice constants and  $\hat{a}_1$  and  $\hat{a}_2$  denote the lattice vectors, which in the general case do not have to be orthogonal (that is, if the lattice is non rectangular). The area spanned by  $\hat{a}_1$  and  $\hat{a}_2$  is known as the primitive cell, or Wigner-Seitz cell.

If the CNFs have a radius of  $R$ , the explicit expression for  $\varepsilon(x)$  is

$$\varepsilon_{\text{CNF}}(\mathbf{r}) = 1 + (\varepsilon_{\text{CNF}}^{(0)} - 1) \sum_{m,n} \Theta(R^2 - (\mathbf{r} - \mathbf{p}_{m,n})^2),$$

where  $\Theta(x)$  is the step function defined by

$$\Theta(x) = \begin{cases} 0, & x < 0 \\ 1, & x \geq 0 \end{cases}$$

and  $\varepsilon_{\text{CNF}}^{(0)}$  denotes the dielectric function of the CNFs.

Belonging to the lattice defined by equation (2.9) there is a corresponding lattice known as the reciprocal lattice. It is defined by lattice vectors  $\hat{b}_i$  having the property

$$\hat{b}_i \cdot \hat{a}_j = 2\pi\delta_{ij}. \quad (2.10)$$

There by the name reciprocal. For a rectangular lattice, equation (2.10) gives the reciprocal lattice vectors

$$\begin{aligned} \hat{b}_1 &= 2\pi \left( \frac{1}{a_x}, 0 \right) \\ \hat{b}_2 &= 2\pi \left( 0, \frac{1}{a_y} \right). \end{aligned}$$

An arbitrary reciprocal lattice vector is denoted

$$\mathbf{G}_{\parallel} = m\hat{b}_1 + n\hat{b}_2,$$

where  $m$  and  $n$  are integers. The reciprocal lattice vectors play an important role in scattering from the PC which will be discussed in the next section. The Wigner-Seitz primitive cell of the reciprocal lattice is known as the Brillouin zone (BZ). High symmetry parts of the BZ are traditionally denoted by different symbols, however there is no consistency on which symbols denote which parts. The notation used in this work is depicted in figure 2.1. In the 1D case the Bloch wavevector,  $k$ , was in the range  $[-\pi/a, \pi/a]$ . In the 2D and 3D cases  $\mathbf{k} \in BZ$ .

## Band structure and band gaps of a PC

The band structure is basically another name on the dispersion relation in a periodic structure, usually described as a multi-valued function  $\omega = \omega(\mathbf{k})$ . There are several different ways to obtain the band structure, some of which will be described in chapter 3. Here it will simply be stated that in two dimensions the different branches of  $\omega$  consist of surfaces. Usually only values of  $\omega$  in high symmetry directions are plotted since this gives an adequate picture of the full  $\omega(\mathbf{k})$  [1, 14]. An example of a band structure in a PC is depicted in figure 2.2.

In figure 2.2 there are shaded regions where there is no frequency for any wavevector. This is due to  $\omega(\mathbf{k})$  flattening out towards the BZ edge. If there are no modes available for

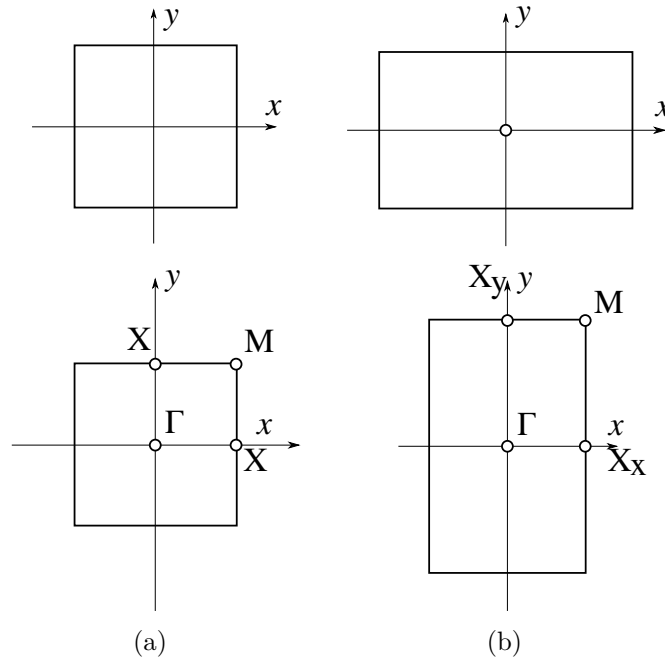


**Figure 2.1:** The Wigner-Seitz cell (top) with corresponding BZ (bottom) with the naming convention used in this work for different high-symmetry subsets. In (a) for a square and (b) rectangular lattice.

any  $\mathbf{k} \in [\Gamma, X]$  at a particular span of frequencies  $[\omega_1, \omega_2]$  the structure is said to exhibit a band gap for these frequencies. Light at these frequencies can not propagate in the PC. If a cavity is created in the PC by modifying or removing some part of the structure and an electromagnetic mode with frequency within the band gap is excited in the cavity, this mode can not escape. This was the idea behind Yablonovitch paper titled "Inhibited Spontaneous Emission in Solid-State Physics and Electronics" [2].

It is also interesting to note that since

$$\frac{d\omega}{dk} \rightarrow 0$$

at the BZ edge, the group velocity of these modes vanishes according to equation 2.4. This property is explored later in the thesis.

## 2.2 Diffraction from a two dimensional surface

When an incoming wave  $E_{in}$ , with wavevector  $\mathbf{k}$ , hits multiple objects placed in space at positions  $p_i$ , each object scatters the wave. The general problem of solving the resulting field configuration is very hard and one of the most extensively studied in different branches of physics, mathematics and electronics. For the special case of scatterers placed in a periodic pattern the problem simplifies significantly. There are diffraction conditions that state that scattering will result in a number of coherent beams going out from the structure [1]. Each beam direction is determined by interference between the outgoing waves from each scatterer. The condition for positive interference (the diffraction condi-

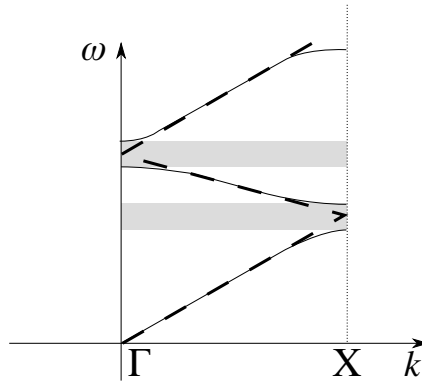


**Figure 2.2:** Sketch of how a band structure plot might look like. The solid thin line corresponds to the band structure of a PC. The shaded regions highlight the band gaps. The dashed thick line is the vacuum mode, corresponding to viewing the vacuum as a periodic structure with the same lattice constant as the PC – the light-line.

tion) is

$$\mathbf{k}' = \mathbf{k} + \mathbf{G}, \quad (2.11)$$

where  $\mathbf{G}$  denotes any reciprocal lattice vector, defined in the previous section and  $\mathbf{k}$  is the wavevector defined previously. The scattered wavevector is denoted  $\mathbf{k}'$ .

In this work, diffraction from two-dimensional surfaces is considered. Square and rectangular lattices will have reciprocal lattice vectors

$$\mathbf{G}_{\parallel} = (G_x, G_y) = 2\pi \left( \frac{m}{a_x}, \frac{n}{a_y} \right),$$

where  $m$  and  $n$  are integers. Let  $\hat{z}$  be the surface normal of the lattice. For an incoming wave with wavevector  $\mathbf{k} = k_{\parallel} + \hat{z}k_z$ , a diffracted wave will have a wavevector

$$\mathbf{k}' = \mathbf{k}_{\parallel} + \mathbf{G}_{\parallel} + \hat{z}k'_z = \mathbf{k}'_{\parallel} + \hat{z}k'_z. \quad (2.12)$$

There is no requirement for the  $z$ -component of the wavevector to be conserved since there is a material discontinuity in the  $z$ -direction (while in the  $(x, y)$ -plane  $k_{\parallel}$  has to be conserved up to a reciprocal lattice vector, which is what eq. (2.11) says). Light-matter interactions considered here are linear, requiring energy to be conserved over the scattering event:  $\omega' = \omega$ . This rewrites, via the free space dispersion relation  $k^2 = (\omega/c)^2$ , to

$$\begin{aligned} k_z'^2 &= k^2 - (\mathbf{k}_{\parallel} + \mathbf{G}_{\parallel})^2 \\ &= k^2 - (k_x + mG_x)^2 - (k_y + nG_y)^2, \end{aligned} \quad (2.13)$$

where the last line holds for a square or rectangular lattice and the top line is valid for any lattice configuration. This diffraction equation is used later when light scattered from CNF-PCs is studied.

For a wave not to be bound (to the surface), the  $z$ -component of its wavevector has to be real. This makes equation (2.13) set limitations on which  $\mathbf{G}_{\parallel}$  result in diffracted beams: only  $(m, n)$  rendering  $k_z'^2$  positive are possible to detect at a macroscopic distance away from the surface.

The tuple  $(m, n)$  is used to order the diffracted beams found in the experimental situation,  $(0, 0)$  being the specular beam. Orders with non-negative  $m$  and  $n$  are called forward scattered and non-positive, backward scattered.

## The form factor and the structure factor

It should be noted that the diffraction condition, equation (2.13), does not depend on the particular geometric shape of the scatterers. Only the translational symmetry comes into play. The scatterer shape is in diffraction theory known as the form factor. All scatterers present in a particular lattice considered together constitutes the structure factor. It controls the intensity of the diffracted beam, while the overall periodicity controls beam direction.

The integral

$$f_j = \int_{\mathbb{R}^3} \varepsilon_j(\rho) e^{-i\mathbf{G}\cdot\rho} dV \quad (2.14)$$

is the form factor of the  $j^{\text{th}}$  scatterer in the lattice basis. The dependence on shape and dielectric function of the scatterers building up the lattice is contained in  $\varepsilon_j$ .

The structure factor can be shown to be

$$S_G = \sum_j e^{-i\mathbf{G}\cdot\mathbf{r}_j} f_j,$$

which is a sum over the form factor of the different scatterers, each centred at  $\mathbf{r}_j$ , and fulfilment of the diffraction condition (2.12) is assumed. The structure factor controls diffraction intensity.

Any polarisation dependence in  $f_j$  comes from  $\varepsilon_j$  which in the general case is a tensor. In equation (2.13), it can also be seen that there is no signature of the polarisation of the electromagnetic beam. Hence beam direction is not determined by polarisation. If, however, the form factor is polarisation dependent, different polarised beams will diffract with different intensities.

A deformation of the lattice, as will be considered in detail later, by electrostatic actuation of the CNFs, will for some diffraction orders appear as a change in the periodicity (that is, in the diffraction condition of equation (2.13)). For others, it will appear as a change in the form factor.

## 2.3 Polarised light

Light consists of coupled electric and magnetic fields oscillating at very high frequencies. If the wave propagation is in an unbound loss-less material both the E- and B-fields are perpendicular to the direction of propagation, set by  $\mathbf{k}$ .

The polarisation state (ignoring light intensity and absolute phase which is not an observable) of the beam exiting from this set-up can be described by the Jones vector

$$\mathbf{E}^{\text{pol}} = \begin{bmatrix} \sin \theta e^{i\delta} \\ \cos \theta \end{bmatrix}. \quad (2.15)$$

If light falls on a surface with a polar angle  $\alpha$  to the surface normal, two polarisation cases can be considered: The electric field is parallel or perpendicular to the plane spanned by the surface normal and the light beam. These two cases are known as  $p$ - and  $s$ -polarised light respectively. In engineering literature these are often referred to as TM and TE modes. Also the terms E- and H-polarisation are used. These correspond to  $\theta$  being 0 or

90 degrees in equation (2.15). Other values of  $\theta$  and  $\delta$  create more general polarisation states known as elliptically polarised light. Variations of the naming schemes of different polarisation states exist depending on the situation. For instance in chapter three where the plane wave expansion method is discussed, the notation of E and H-polarisation is used and here it denotes the field component perpendicular to the symmetry plane.

In a reflection a polarisation state is transformed, and the transformation can be expressed using the Jones matrix

$$\mathbf{E}_{\text{out}}^{\text{pol}} = M_J \mathbf{E}_{\text{in}}^{\text{pol}}. \quad (2.16)$$

The elements of the diagonal of  $M_J$  are the Fresnel reflection coefficients and if there is polarisation conversion this is indicated by the off-diagonal elements of  $M_J$ .

If a light beam does not have a well defined polarisation state, that is, different photons have different polarisation, a more general description than the Jones description has to be deployed. The statistical properties of a partially polarised beam can be characterised by the Stokes vector. This is a four parameter vector completely characterising an incoherent partially polarised light beam. In a manner similar to how reflection at a surface for a well defined polarisation state can be described using a Jones matrix, it can be described by a  $4 \times 4$ -matrix operating on the Stokes vector. This matrix is known as the Mueller matrix. The Stokes vector description of a light beam works with intensities rather than amplitudes, as for the Jones vector description. Hence the Stokes nomenclature is not a pure generalisation of the Jones nomenclature. Mueller matrix calculus, the operation with Mueller matrices on Stokes vectors, cannot fully describe coherent light.

## 2.4 Surface Plasmon Polaritons

A surface plasmon polariton (SPP) is a confined mode that exists at the interface between a metal ( $\text{Re}[\varepsilon] < 0$ ) and a dielectric [63]. These cannot be excited on a flat surface by free-space electromagnetic radiation due to mode miss-match. Only  $p$ -polarised SPPs exist. Since these modes propagate along a metal surface which usually has a large degree of damping in the visible region, SPPs experience strong damping, and SPP excitations appear as dips in spectroscopic data. Several features of the optical properties of CNF-PCs discovered in Papers II-IV are linked to SPP excitation.

## 2.5 Properties of carbon nanofibers

There is a large body of papers on different properties of CNTs such as their optical, mechanical and electrical properties. Carbon nanofibers are not as heavily studied, but there are still several papers covering different properties. In general there are usually large spans in values reported for different parameters. The properties of importance for the present work are the Young's modulus,  $E$ , describing the stiffness of an object, and the dielectric constant,  $\varepsilon$ , describing light speed and damping for light propagating in the material. In this work, no attempts to characterise these have been performed, instead it is noted that there is no final conclusion on what controls these parameters in a particular case.

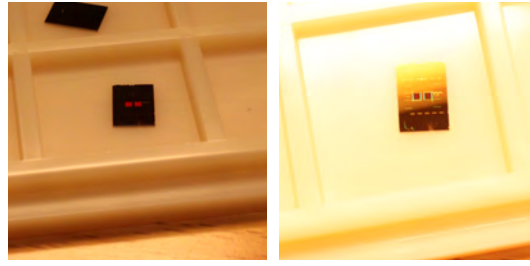


**Figure 2.3:** Left: Photograph depicting a CNF-PC in a chipbox where the camera was placed in an angle of diffracted light. Right: Photograph of the same sample from a direction where no diffraction occur. The PCs are the small squares on each chip, appearing brighter than the background to the left and darker to the right.

## Mechanical properties of carbon nanofibers

In [64] Zhang *et al.* determined the Young's modulus of CNFs to be in the range of 90 GPa and in [65] Eriksson and co-workers report a value of 410 GPa (This can be compared to e.g.  $\sim 200$  GPa for steel [66]). In [67] Ozkan *et al.* report an elastic modulus in the range of 200 GPa. In [68] theoretical considerations report a wide range of values from 30 GPa and up depending on the internal CNF structure.

The second moment of inertia,  $I$ , is a purely geometrical quantity of a beam and relates its shape to how rigid it is [66]. For a hollow beam with circular cross section it is

$$I = \frac{\pi}{4}(r_o^4 - r_i^4),$$

where  $r_o$  is the beam outer radius and  $r_i$  is a (possibly zero) inner radius. For typical CNF numbers  $I \simeq 40 \cdot 10^4 \text{ nm}^4$ .

## The dielectric function of carbon nanofibers

Carbon is an extremely rich material when it comes to the different forms it can take. It can exist as regular graphite, as diamond, and amorphous carbon, as different nanostructures such as CNTs, fullerenes and CNFs, not to mention all the molecular compounds it makes with other atoms forming the basis for life. All these different forms of carbon have very different optical properties. Diamond is isotropically transparent with a very high refractive index in the visible, while graphite is anisotropic and opaque. In modelling CNF-based structures the question of what dielectric function [69] to use to describe the CNFs naturally arises. It is not possible to simply measure from a film since the values will certainly be different from CNFs grown vertically free-standing.

By simply looking at a VACNF-covered surface it is clear that the imaginary part of  $\varepsilon$  is significant since the surface appears dark, see figure 2.3. There are several papers,[70, 71], discussing the dielectric function of CNTs and CNFs. However these are not conclusive. This is in line with other properties of CNFs and CNTs, such as stiffness and conductivity, which vary a lot between samples. In Paper I we were not primarily interested in capturing the exact behaviour of VACNF-based PCs, but rather to understand the effects of actuation. Hence in this work CNF dielectric functions  $\varepsilon = 10$  and  $\varepsilon = -\infty$ , corresponding to a strong dielectric and a perfect metal were used and compared. The use

## 2.5. Properties of carbon nanofibers

---

of such artificial dielectric constants was motivated by the fact that VACNFs are not the only candidate for building the kind of structures studied. Alternatives are to use other nanowire materials such as InP, Si, MoS or ZnO or to cover any chosen nanowire with any other material, e.g. by thin film deposition.

In Paper II and III the goal was to obtain as good a fit as possible to the experimental data without introducing too many parameters. Hence in these works a refractive index of  $n = 4.1$  was used, giving a dielectric constant of  $\varepsilon = 16.8$ .



# Chapter 3

## Modelling methods

This chapter describes the three methods used in modelling the VACNF-based PCs.

The transfer matrix method [72, 73] is well known for scattering and transmission/reflection computations. It was used together with the Kronig–Penney model [1] in Paper I to investigate how a one-dimensional dielectric stack with changing inter-dielectric distances affects the band structure of this 1D model of a PC.

In Paper I, the plane wave expansion method [14] was used to obtain the band structure of 2D pillar-based PCs.

The primary tool for modelling the CNF PCs in this work has been the finite-difference time domain (FDTD) method. FDTD algorithms are widely used and there are several ready-made packages available. However, the algorithm family is still being actively developed to increase accuracy and speed. In this work the free and open source package Meep [74] was used for transmission computations in Paper I. For Papers II and III the implementation Lumerical [75] was used to obtain band structure and far-field diffraction patterns.

### 3.1 Transfer matrix method

The transfer matrix method is very useful to obtain the band structure in one dimensional systems with piecewise constant potential (the Kronig–Penney model). It is a general analytical method applicable to different types of wave equations. The idea is to start with eigensolutions to the wave equation in the constant-potential regions. These are usually relatively easy to find, as described in chapter 2 for a one-dimensional electromagnetic system. The physical details, e.g. Maxwell’s equations, of the particular problem at hand are then used to relate solutions in different constant regions. This sets the boundary conditions for each constant-potential region. The equations describing these relations are usually matrix equations, and can for the different potential steps, be joined together to yield an equation for the whole system (thereby the name). This final equation, together with boundary conditions for the whole system (e.g. periodic boundary conditions), can then be solved to find the eigenvalues of the whole system, and hence the band structure.

## 3.2 Plane wave expansion

The plane wave expansion method is a computational way to obtain the band diagram of a PC, or in general any periodic system. The basic idea is to go to Fourier space and then solve the wave equation there. For a simple lumped finite linear system, like an electric circuit, going to Fourier space is simply done with a Fourier transform of the differential equation that needs to be solved, i.e. equation (2.6). However, it is not quite as straightforward here as the periodic  $f(x)$  multiplies the unknown function  $E$  in equation (2.6). So, if trying to do a Fourier transform directly, the term  $f(x)E(x)$  will result in a convolution in Fourier space, which is not wanted.

Instead  $f(x)$  is expressed as a Fourier sum which can be done since  $f$  is periodic. Bloch's theorem states that the unknown function,  $E(x)$ , is also periodic, and hence can also be expressed as a Fourier sum. These two sums will be over two independent indices, giving rise to a matrix equation in  $k$ -space. The matrix equation will involve "infinite matrices"<sup>1</sup>, indexed by reciprocal lattice vectors. However, for a sufficiently well-behaved dielectric function, elements with higher index decay towards zero, making it possible to introduce a cut-off and only consider a finite approximation of the matrix. The finite (but large) matrix can then be exactly diagonalised on a computer. The procedure is described in more detail by Sakoda [14], but the main equation that needs to be solved in two dimensions is

$$M_{\mathbf{k}}E_{\mathbf{k}} = \frac{\omega^2}{c_0^2}E_{\mathbf{k}} \quad (3.1)$$

where  $M_{\mathbf{k}}$  is a matrix that depends on polarisation and has the form

$$M_{\mathbf{k}}(\mathbf{G}, \mathbf{G}') = \widehat{\varepsilon}^{-1}(\mathbf{G} - \mathbf{G}')|\mathbf{k} + \mathbf{G}'|^2$$

for the E-polarisation and

$$M_{\mathbf{k}}(\mathbf{G}, \mathbf{G}') = \widehat{\varepsilon}^{-1}(\mathbf{G} - \mathbf{G}')(\mathbf{k} + \mathbf{G}) \cdot (\mathbf{k} + \mathbf{G}')$$

for the H-polarisation.  $\widehat{\varepsilon}^{-1}(\mathbf{k})$  is the (spatial) Fourier transform of the inverse of the dielectric constant. Depending on the implementation,  $\widehat{\varepsilon}^{-1}$  can be calculated either analytically or via the fast Fourier transform of the real space representation.

With the plane wave method, the band diagram of a PC is obtained (the eigenvalues of the matrix  $M_{\mathbf{k}}$  for each selected wavevector  $\mathbf{k}$ ). The modes in  $k$ -space (these are the eigenfunctions,  $E(\mathbf{k})$  in equation (3.1)) can also be obtained and can be inverse Fourier transformed to get the real space modes. The method can also give information about the density of states by counting the number of eigenvalues in an interval  $d\omega$ . The method was used in Paper I to obtain band structures of model systems considered in that work.

The main drawback of the plane wave method is convergence speed. In order to get good numerical accuracy, many reciprocal lattice vectors have to be included in the matrix  $M_{\mathbf{k}}$ . In two dimensions this is not a major issue on a modern computer where matrices of  $500 \times 500$  are easily diagonalised, which is enough to give high accuracy. In three dimensions convergence is a larger problem and can require parallelism. Another drawback is that the method only gives information about infinite systems, not slabs which is often

<sup>1</sup>They are not really matrices since the indices run from 0 to  $\infty$ .

more appropriate to consider for PCs. Particularly limiting is also that dielectric materials with damping can not be handled, also since only infinite systems are considered. Several of these problems can be addressed by instead using a time-based method which will be described in the next section.

## 3.3 Finite-difference time-domain method

If one is interested in solving differential equations numerically, there are two main approximations to choose between when starting. Either the differential operator is approximated by a discrete version which renders a difference equation that can be treated on a computer or the unknown solution is approximated by a function that can be differentiated analytically (known as the Galerkin method). That is, the solution is expanded in some basis where the differential operator can be applied analytically to each basis function. The resulting regular (typically matrix, non-differential) equation can be solved by some means on a computer. FDTD is the resulting algorithm if the first of these approximations is selected and implemented in the time domain. The second method results in what is known as the finite elements method (FEM). The methods have different advantages and disadvantages. FDTD was selected in this work due to its simplicity and well established position in computational electromagnetics.

This section will introduce the concepts related to FDTD computations required to appreciate the results on CNF-based PCs presented later. More in-depth discussions of the FDTD algorithm can be found in Taflove [76] and Bondeson [77].

The basic idea in the FDTD method is to let

$$\frac{df}{dx}(x) \rightarrow \frac{f(x+h) - f(x)}{h} \quad (3.2)$$

for some finite  $h$ . Corresponding approximations are done for higher order and dimension derivatives. If the time-dependence was left untouched before equation (2.3) approximations like (3.2) can be applied to the differentiation operators and yield

$$h(k, n+1) = 2h(k, n) - h(k, n-1) \left( \frac{c\Delta t}{\Delta x} \right)^2 (h(k+1, n) - 2h(k, n) + h(k-1, n)), \quad (3.3)$$

where  $k$  is the spatial index and  $n$  is the temporal index.  $\Delta x$  and  $\Delta t$  are the spatial and temporal steps. The only term depending on  $n+1$  is on the left hand side, so by specifying an initial condition for two time steps and the whole space, equation (3.3) can be used to step in time and obtain a solution for later times. This idea can be generalised to approximate the full Maxwell's equations (ME). This is the full FDTD algorithm for electromagnetics and is implemented in e.g. the packages Meep and Lumerical.

### Sources

Initial conditions in space can be introduced in different ways. A common way to select initial conditions is to use the sources in ME to generate fields. Usually the source is set to have a particular spatial shape and temporal content corresponding to a desired

computation. A Gaussian source has the temporal shape

$$s(t) = e^{i\omega_0 t} e^{-\frac{(t-t_0)^2}{(2T)^2}} \quad (3.4)$$

and frequency content

$$S(\omega) = 2T\sqrt{\pi} e^{-i(\omega-\omega_0)t_0} e^{-T^2(\omega-\omega_0)^2}$$

and is often a convenient choice. Equation (3.4) describes a wave packet centred at  $\omega_0$  and peaked at time  $t_0$  with temporal width  $2T$ . By using a source such as equation (3.4) a computation for several frequencies can be performed in a single run.

## Resolution

The most prominent approximation deployed in the FDTD method is of course the discretisation of space and time. A discretisation comes with a selected time step,  $\Delta t$ , and space step,  $\Delta x$ . These can not be selected independently. The Courant stability [76] criterion controls the relation between  $\Delta t$  and  $\Delta x$ .

Two methods are commonly deployed to test the computational result in FDTD. A simple method is to perform a computation with increasing resolution,

$$h = h_0, 1/2h_0, 1/4h_0 \dots$$

and increase the resolution until no difference can be detected in the result. Another method is to perform the computation for a number of resolutions. The result, say  $r_h$ , is saved for each computation. A fit, *e.g.* in the least square sense, is made to  $r_h$ , resulting in a function  $r_h^{\text{fit}}$ . If the fit converges it could be expected that the limit  $r_h^{\text{fit}}, h \rightarrow 0$  is the best approximation.

## Boundary conditions

FDTD works in ordinary time and space. Therefore it is required to have some boundary conditions in time and space. Dirichlet or Neumann boundary conditions [58] are not adequate to apply in most physical situations. For example the Dirichlet condition that the E-fields should be zero at the boundary corresponds to doing the computation surrounded by perfect metal. If the simulation is run in some structure where the fields decay rapidly enough towards the edges this is adequate, but usually this is not the case, especially not in PC simulations. In many situations it is desirable to perform the computations in free space, in principle requiring an infinite computational cell. A solution to this problem was given by Berenger in 1994 with the introduction of what is known as perfectly matched layers (PMLs) [78]. This is a non-physical material that, analytically, does not reflect the electromagnetic fields at a boundary to any physical material<sup>2</sup>. This is achieved by an analytical continuation of ME into complex coordinates where field components are decaying. A coordinate transformation is then performed that takes the complex coordinates to real ones and gives a region where fields are attenuated. So, if the computational cell is surrounded by PMLs the particular boundary conditions used do

<sup>2</sup>The numerical approximation of a PML can have some reflections coming from the discretisation, which is one reason why care has to be taken when discretising.

not matter since all fields decay strongly towards the edge and usually then the Dirichlet boundary condition is used. It is important to realise that PMLs are usually only damping in one direction, that is, they can allow for waves to travel in one direction while damping in another – they are anisotropic. So fields can sneak by an obstacle that is tangential to the PML and diffract back into the computational cell on the other side, distorting the computational results. In an FDTD simulation where one wants to simulate a system surrounded by free space and is not interested in the far-field, the computational grid can be surrounded by a PML of some appropriate thickness. There are also other methods to damp out the fields towards the edges, generally known as absorbing boundary conditions, but PMLs are today the standard way to do this.

### Transmission computations

In Paper I we were interested in obtaining the transmission for different frequencies through a CNF-PC. To obtain this using the FDTD method, first a geometry is set up and a normalisation computation is performed. In this run, transmission through the computational cell from the source to a defined output is computed and the result,  $f_r^0$ , at the output is recorded and stored. Next, the structure of interest is introduced in the computational cell and a new computation with the same input source is executed. The computations are executed until all field components in the computational cell have decayed below some threshold. The field at the output,  $f_r$ , is again recorded. Then the fields are Fourier transformed in time to obtain their spectral contents  $F_r^0$  and  $F_r$ . The transmission coefficient is obtained by taking

$$T = F_r/F_r^0.$$

Usually in these computations a Gaussian source such as equation (3.4) is a good choice due to its smooth spectral content.

There is one point of importance that should be noted when performing these computations. The power input by the source depends on the local density of states (LDOS) in the structure. So, to have a proper normalisation, it is important that the LDOS does not change between the two computations. If e.g. a geometry such as that depicted in figure 6.4 is considered, the distance  $S_1$  has to be large enough so that when the PC structure is inserted, it does not affect the LDOS at the source.

### Band structure computations

The band structure of a periodic system can be obtained in FDTD computations by solving the fields for the Wigner-Seitz cell of the structure and enforcing periodic boundary conditions. It is known that the modes are Bloch modes, and hence equation (2.8) holds. This sets the form of the periodic boundary conditions, enforcing a particular phase relation, set by the Bloch wavevector  $\mathbf{k}$ , at the edges. Fields are excited by an arbitrary source (containing the relevant frequency components), finite in time and placed somewhere in the structure. The computation is started and run for some time. After the system has reached a steady state, the field intensity,  $f_r$ , is recorded at an arbitrary point in the structure. The recording is Fourier transformed, rendering  $F_r$  which contains resonant frequencies of the structure for the particular Bloch mode wavevector. The computation

is repeated for all wavevectors,  $\mathbf{k}$ , of interest to obtain the band structure. This type of computation was performed in Paper II. It should be noted that this works since the LDOS of the periodic structure only will allow electromagnetic energy at frequencies allowed by the structure to be input by the source.

## Far-field computations

It is not possible to obtain the far fields directly in an FDTD computation since it would require an enormous computational cell. Instead there are analytical transformation equations [76] relating the near-field, solved in the FDTD computation, to the far-field. This was used in Paper III to obtain the diffraction pattern from FDTD computations on PCs.

## Modelling carbon nanofiber actuation in FDTD

This section covers the actuation profile of CNFs used in the modelling and how the curved structure is introduced in the FDTD computational cell.

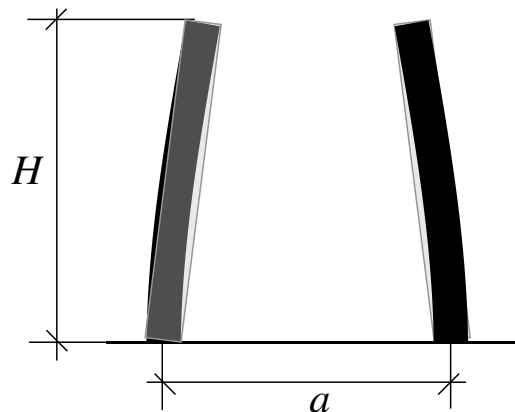


**Figure 3.1:** Bending profile for two CNFs actuated according to the profile found in equation (3.5) with realistic parameters set to  $R/H = 0.106$ ,  $a/H = 0.29$  and  $\frac{1}{2} \frac{F_0}{EI} / H^2 \simeq 0.15$ . Over the left CNF is sketched the profile approximation of a straight cylinder tilted an angle. The same cylinder is placed below the right CNF for visual aid.

The bending of CNFs is described by the Euler-Bernoulli beam equation

$$\frac{d^2}{dz^2} \left( EI \frac{d^2}{dz^2} x(z) \right) = P(z),$$

where  $E$  denotes the Young's modulus and  $I$  the second moment of inertia of the CNFs. The load  $P(z)$  should be evaluated by solving the Poisson equation [58] to determine the charge distributions in the CNFs in the presence of applied external voltages. The two equations are coupled: the beam equation determines the device geometry which influences the charge distributions and, consequently, the bending forces on the CNFs. For metallic CNFs, most of the charge is located in the tip of the CNF and the load is therefore concentrated at the tip,  $P(z) \approx F_0 \delta(z - H)$ . The CNF profile is then approximately given

### 3.3. Finite-difference time-domain method

---

by the analytic expression

$$x(z) = \frac{1}{2} \frac{F_0}{EI} \left( Hz^2 - \frac{z^3}{3} \right). \quad (3.5)$$

This is the profile used for the CNFs in situations when actuated CNF profiles are considered. The main approximation in the electromechanical analysis is that the cross sections and Young's moduli of the CNFs are independent of bending, which is valid if the minimal radius of curvature is large, *i.e.* the maximum deflection is small compared to the CNF length, which it typically is in our case. The bending profile is illustrated in figure 3.1 for two CNFs.

In the FDTD simulations, the set of points constituting the bent CNF is approximated by  $N$  short straight cylinder segments:

$$CNF = \bigcup_{i=0}^{N-1} C_R((x(z_i), z_i), (x(z_{i+1}), z_{i+1})),$$

where  $z_i = \frac{i}{N}H$  and  $C_R(\text{start}, \text{stop})$  denotes a cylindrical shaped set of radius  $R$  with ends at start and stop. The number of segments  $N$  was increased until further increase did not yield any difference in the computational result. As can be seen in figure 3.1, for a weakly actuated CNF, using only one cylinder is a fairly good approximation.



# Chapter 4

## Carbon nanofiber fabrication

This chapter describes the CNF growth fabrication process. The PC fabrication process can be divided into two main parts: substrate processing and VACNF growth. The substrate processing covers all processing done to the substrate prior to CNF growth. This follows, to a large degree, standard micro-fabrication technology and is not described here. Some details concerning the processing can be found in the appendix.

CNTs and CNFs can be fabricated in mainly three different ways: Arc discharge, laser vaporisation and CVD [79, 80]. In the present work, CVD was used. This is the most promising method for commercial production and a much used method for industrial production of many compounds. In a CVD process the feedstock for production is delivered via one or several process gases which react chemically in the gas phase and/or on the surface present in the process chamber, leading to deposition. The process can be assisted in several ways, e.g. thermally, via catalysis or with the aid of a plasma. Control parameters are typically gas composition, flow rates, pressures, process time and other timing parameters. In the rest of this chapter the CVD processes used in the present work will be presented.

CVD VACNF growth is not a mature technology and when the work covered in this thesis was started, there were no commercially available tools for CNF fabrication. The samples reported on in Papers II and III were fabricated in a home-made set-up of the group. During my working time, a new commercial system, the Aixtron Black Magic 2 inch R&D [81] was purchased, and the VACNF growth performed for Paper IV was done in the new system. In this work CNF growth was catalysed by nickel (Ni) seeds [82] which is the most common catalyst substance used for CNF growth. Titanium-nitride (TiN) was used as the metal underlayer.

There is a large body of reports from studies [83, 84, 85, 86, 87, 88] on growth of CNFs and VACNFs and many questions that were unsolved a number of years ago [89] are today resolved. However VACNF growth can still not be considered a mature technology. Today studies focus on particular details in connection to the growth. The view emerging is that VACNF fabrication is a very complicated process where details such as substrate morphology, air exposure time and initial growth phase conditions strongly affect the final result [38]. The aim of the present work was to study optical properties of VACNF arrays. Thus no controlled investigations on VACNF growth were performed. Rather what is presented here are practical details dealt with during the work.

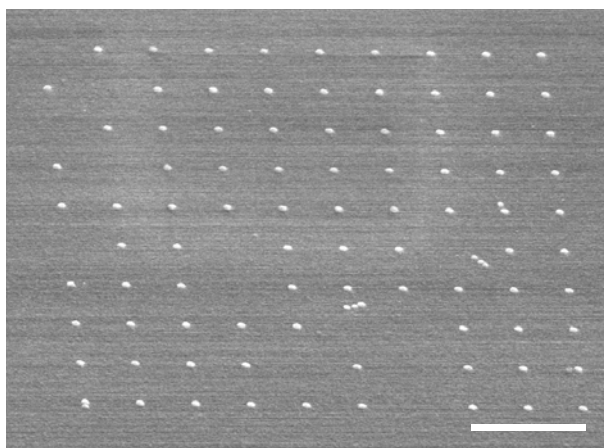


**Figure 4.1:** Ni dots on Mo after heating the substrate. Note that particles have disappeared and also that some particles have moved around on the substrate surface.

## 4.1 Selecting metal underlayer

Growth on different metal underlayers has been studied in several papers. In particular Mo, W, Ti, Pt, Pd, NiCr, Nb, Cr were considered in [90]. A few years ago Melechko *et al.* presented an extensive review [91] covering several aspects of both fabrication and applications. Early in this work, W was selected as an underlayer material, but was later abandoned due to poor mechanical adhesion between CNFs and W. It was expected that the samples produced would require post-growth processing and free standing CNFs on W cannot be processed by further lithographic steps since the CNFs cannot withstand the resist spinning step. They are ripped off from the surface. It was also anticipated that there could be a potential problem when actuating the VACNFs if they were not well attached to the substrate surface. Consequently, Mo was instead selected.

During the work on growth on Mo it was found that a large part of the Ni catalyst particles diffused, both on the surface, and down into the surface, see figure 4.1. This was, at least partly, due to problems of depositing a dense enough Mo underlayer which was e-beam evaporated. Hence, a second material switch was made, now to titanium nitride (TiN) for which there are several studies showing good growth [92, 93, 94]. This was the material used as underlayer for the work presented in Papers II-IV. The growth process, as pointed out above, is sensitive to the metal underlayer and when varying it, also the VACNF growth procedure has to be modified. This point has not always been considered in earlier works.

## 4.2 Growth conditions

The growth performed for Papers II and III was done in the purpose built PECVD chamber mentioned above. This process is denoted A and described in more detail below. On this system, to a large degree manually controlled, it was difficult to obtain reproducible results. Because of the fairly simple substrate preparation process required for the work presented in Papers II and III, where non-tunable structures were considered, a low yield fabrication process was acceptable.

## 4.2. Growth conditions

---

Samples used in Paper IV required significantly more pre-growth processing when electrodes were to be fabricated. It was also required that the metal underlayer would have a high conductivity to successfully achieve actuation. During the course of the thesis work, a new PECVD system was purchased, the Aixtron Black Magic system. This is a system which to a much higher extent is computer controlled and hence rendered higher reproducibility of the results. Sample fabrication for the work presented in Paper IV was done using the new Aixtron system. This growth process differed to a significant degree from the process used in the home-built system, and will be described separately below, denoted as growth process B.

To grow a single CNF the catalyst metal was prepared as an isolated dot. It has previously been suggested [95] that an optimal dot size is  $50 \times 50 \text{ nm}^2$  and 10 nm high, giving a catalyst volume of  $25 \cdot 10^3 \text{ nm}^3$ . Larger dots tend to split up into several dots, and smaller dots do not grow as straight CNFs. This dot size was used in growth process A. In process B,  $70 \times 70 \times 15 \text{ nm}^3$  was found to yield better results. Optimal dot size is one of the parameters that vary with growth process and metal underlayer.

### Growth process A

The growth procedure for growth on a TiN underlayer consists of the following steps, see figure 4.2 for an illustration of the different chamber parts. Samples were mounted on the sample holder with a local resistive heater. The sample holder doubles as one of the electrodes for inducing the plasma, the other one being placed above the sample. After the holder has been inserted in the vacuum chamber, the chamber can be pumped down to below  $10^{-7}$  torr. The process is not critically dependent on such a low pre-pressure however, and no correlation was found between growth quality and pressure below  $10^{-3}$  torr. The heater was turned on, and the temperature ramped to 500 °C with a rate of 100 °C/min. At the same time, ammonia was introduced into the chamber at 60 sccm. At 4 torr the DC-plasma was ignited, which occurs simultaneously with the sample reaching 500 °C in our set-up. A plasma current of  $\sim 4 \text{ mA/cm}^{-2}$  was applied for 2 min to clean the substrate and activate the catalyst particle. It has also been found that a pre-growth heating step lets the Ni catalyst particle settle into a crystalline shape that is beneficial to the growth [96]. Actually, in growth processes B, described below, the sample is kept at a high temperature for a very long time (up to one hour) to increase this effect. During this step, the temperature was ramped by 50 °C/min. At 600 °C, acetylene was introduced into the chamber at 15 sccm and the ammonia flow was reduced by 33%. At 700 °C, the temperature was kept constant and the growth time measurement was started. 1  $\mu\text{m}$  long fibers grew in approximately 20 minutes.

### Growth process B

The growth process presented here was developed by Ghavanini [96] for fabricating varactors based on VACNFs, and was carried out in the Aixtron system. This system has all the same components as the home-built system described in process A. However some significant differences are:

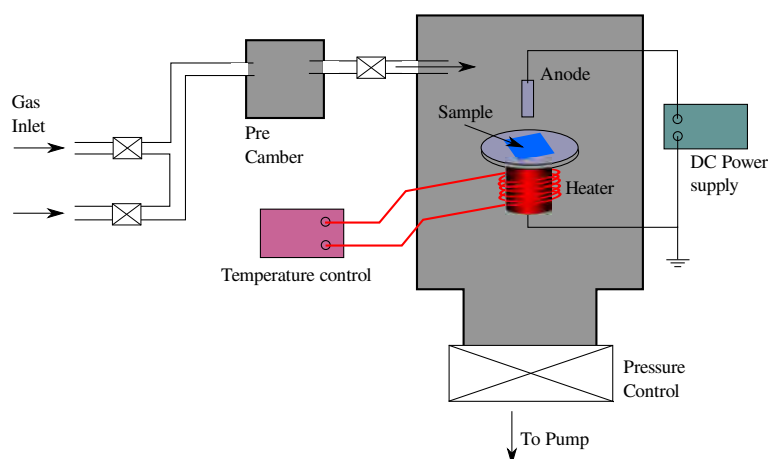


**Figure 4.2:** Sketch of the PECVD chamber used in the fabrication of VACNFs using process A.

- The Aixtron system is fully computer controlled, eliminating timing issues and other human factors in the process.
- The heater in the Aixtron system is made from a thin carbon plate with the thermocouple immediately connected to the heater plate. This is expected to improve reproducibility of the temperature.
- Gases in the Aixtron system are introduced to the process chamber through a shower-head, improving gas distribution. In the home-built system gases are introduced in a pre-chamber and allowed to diffuse to the sample, see figure 4.2.
- The Aixtron system uses a bell-jar chamber that does not allow as low a pressure to be reached as the home-built set-up which uses a stainless steel vacuum chamber.
- The Aixtron system uses a pulsed DC-source for the plasma. The source used in the home-built system is a pure DC source, see below for a discussion on what consequences this has.

There is a problem with growing on partly insulating substrates with a DC-PECVD system. From the DC, large voltages build up, discharge, and destroy the sample, see figure 4.3 depicting this effect after growth using process A. There have been a number of suggested solutions to this problem, e.g. performing the metal patterning after the CNF growth [97] or using a sacrificial layer of metal covering the whole surface and removing it after growth [96]. These processes have the disadvantage of requiring post-growth processing in the sample which often damages the CNFs. In the Aixtron system the problem has been solved by using a pulsed plasma source where voltage polarity is switched for short times to discharge the system. It is not completely clear how well this works, but it was the method used in fabricating samples for Paper IV, which were fabricated in the Aixtron system. Another possibility, useful probably only in research, is to use the properties of a semiconductor as an isolating underlayer. In the growth process the substrate is heated to above 500 °C which makes the semiconductor conducting and

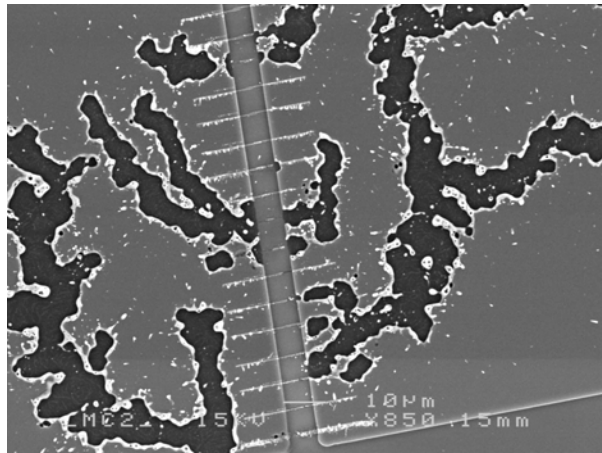


**Figure 4.3:** Discharge destruction of sample surface from growth at a partially isolating substrate in process A.

hence removes the discharge problem. In the measurement situation the substrate is kept at room temperature and the semiconductor is insulating. This approach has not been tested.

The growth procedure in process B was as follows: The sample was mounted on a holder in the system. A thermocouple, used to measure the temperature, was mounted on the holder. A pre-program where all gas lines were pumped and the holder was heated and cleaned using an ammonia plasma was executed. Next, the holder was allowed to cool, thereafter the sample was mounted and the system was pumped down to 0.15 mbar. After this the sample was heated to 750 °C with a ramp rate of 25 °C/min while the system was kept in nitrogen atmosphere at 3 mbar. At 750 °C, the heating was stopped and the sample was cooled to 700 °C at 25 °C/min. This temperature was kept for 30 min. The nitrogen flow was turned off and the sample cooled by 25 °C/min to 580 °C. The system was then pumped for 30 s and then NH<sub>3</sub> was introduced to the chamber at 100 sccm. The system was kept at 4 mbar and after 30 s the plasma was ignited and kept at 60 W for 30 s. Acetylene was introduced into the chamber at 25 sccm and parameters kept fixed for 1 min. After this the plasma power was lowered to 40 W, ammonia flow set to 480 sccm and C<sub>2</sub>H<sub>2</sub> to 80 sccm. The temperature was ramped to 620 °C at 25 °C/min and the growth time measurement was started. 1 µm long fibers were grown in approximately 45 min. All steps performed in this system are set and executed from a script by a controlling computer.

### **Fabrication limitations and reproducibility**

Generally in CNF growth the catalyst particle is consumed during the growth. This is attributed to etching by the cleaning gas (here NH<sub>3</sub>) and that small nano-droplets of the particle are released inside the CNF. This process limits the height of the CNFs. In CNT growth there have been reports of growing CNTs of virtually infinite length [98, 99], and hence it should be possible to overcome this catalyst particle consumption by tuning the fabrication process.

In this work the PC lattice constant is controlled in the e-beam lithography process.

This allows for large dynamics in selecting lattice parameters and it should be possible to fabricate samples with lattice constants down to 150 nm for the tunable structures. The critical part is alignment between following lithography steps which require high quality alignment marks to achieve high resolution patterns.

The CNF diameter is controlled by the catalyst particle, and hence can also be varied in the lithography step. As noted previously, however, there are limitations on how small or large the CNF can be. A too-large catalyst particle split up into several particles and a too-small particle will not yield a straight VACNF. Exact limits are process dependent, but typically the CNF diameter can be varied between  $\sim 40$ -80 nm.

In both processes A and B reproducibility and yield are issues. In process B, however, reproducibility is much better than in process A. It is not know what cause fluctuations in the process. Two samples coming from the same batch and grown directly after each other in time in the VACNF process can give very different results. One sample may consist of perfectly straight CNFs while the next may not displaying any regularity whatsoever. However, samples grown simultaneously consistently yield similar results. It can therefore be interpreted that it is the growth process that is the critical step and not the sample pre-treatment. By the end of the experiments the yield in process A and B respectively was around 20% and 50%. Initially the yields were significantly lower.

# Chapter 5

## Measurements

In the work of characterising the CNF-PCs two main methods have been deployed. An optical set up was constructed where light with different incoming and exiting angles to the sample can be recorded. This set up was used to study diffraction from the PCs. The second characterisation tool used was ellipsometry, which was done in a collaboration project with the Applied optics group in Linköping.

### 5.1 Diffraction

Diffraction is an interference phenomenon that occurs when radiation interacts with a periodic structure. It can be viewed as an extension of the two-slits experiment seen already in high-school. In chapter 2 the theory of diffraction from CNF-PCs was developed. Here a set-up to measure diffraction angles and intensity will be described. The measured angles should be compared to equation (2.13) and the measured intensities to predictions from equation (2.14).

#### Optical set-up

There are several different ways to set up diffraction measurements. In [100] a near-field technique is used that has the advantage of being able to detect diffraction for the exact same microscopical area when varying the incoming polar and azimuthal angles. On the other hand, it has the disadvantage of not being able to measure all four angles simultaneously. In many cases it is enough with a simple screen to project the pattern on to [40, 101]. In this work we were interested in investigating large area effects, and not scattering from single particles. Also we wanted to be able to look at both angles and intensities of the diffracted beam. These requirements led to an approach with a rotation stage and goniometer for both incoming and exiting light.

For a beam diffracted from a substrate, there are four angles characterising the interaction. These are denoted  $D = \{\theta_{\text{in}}, \theta_{\text{out}}, \nu_{\text{in}}, \nu_{\text{out}}\}$  and are illustrated in figure 6.18. They correspond to writing equation (2.13) in polar form. These angles are not directly measured in the lab set-up. The reason is that it is very hard to vary four angles simultaneously with respect to the same centre. The actual lab set-up is displayed in figures 5.3 and 5.4 with a sketch displaying measured the quantities in figure 5.2. Measured quantities are denoted  $M = \{\alpha_{\text{in}}, \alpha_{\text{out}}, \varphi_{\text{in}}, h\}$ .

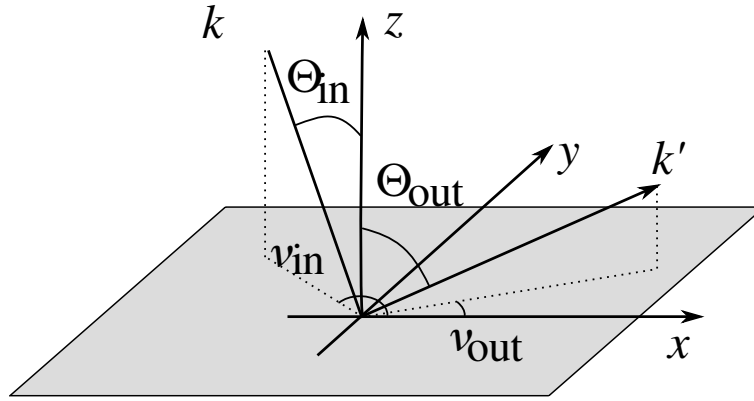


**Figure 5.1:** The quantities measured in a diffraction measurement.  $\Theta$  denotes polar angles and  $\nu$  denotes azimuthal angles, measured from the  $x$ -axis. The sample normal is defined as the  $z$ -axis. On square samples there is no difference between the  $x$ - and the  $y$ -axis, but for non-square samples (e.g. rectangular and tunable PCs) the two in-plane directions are not equivalent.

There are two coordinate systems used in the measurement of the diffraction angles. A spherical coordinate system in the substrate frame is used for the incoming beam. For the scattered beam, a cylindrical coordinate system is used, centred in the lab system frame (same as the optics). In this setting  $R$  is the fixed distance between the PC and the linear scale that measures  $h$ , see figure 5.2. In Cartesian coordinates, as defined in figure 5.2, the normal to the sample is  $\hat{n} = (\sin \alpha_{\text{in}}, 0, \cos \alpha_{\text{in}})$ . Further, the vector  $\bar{d}$  denotes the difference between the sample and a detected diffraction spot. It is  $\bar{d} = (-R \sin \alpha_{\text{out}}, h, -R \cos \alpha_{\text{out}})$ .  $M$  is related to  $D$  via

$$\begin{aligned} \theta_{\text{in}} &= \alpha_{\text{in}} \\ \cos \theta_{\text{out}} &= \frac{1}{|\bar{d}|} \hat{n} \cdot \bar{d} = \left(1 + \frac{h^2}{R^2}\right)^{-1/2} \cos(\alpha_{\text{in}} + \alpha_{\text{out}}). \\ \nu_{\text{in}} &= -\varphi_{\text{in}} \\ \nu_{\text{out}} &= \tan^{-1} \frac{h}{R \sin \alpha_{\text{out}}} + \varphi_{\text{in}}. \end{aligned} \quad (5.1)$$

The experimentally obtained angles  $\theta_{\text{in|out}}$  and  $\nu_{\text{in|out}}$  can now be compared to predicted angles. Predicted angles are obtained from equation (2.13) by expressing the wavevectors in polar coordinates.

## Sample alignment

In this section numbered optical components refer to the enumeration found in figures 5.3 and 5.4. A particular component is referred to as [figure number]-[component number]. To get accurate measurements it is important to have a well aligned sample and set-up. Initially stages 5.3-3 and 5.3-5 are adjusted to align the holder. Linear  $xy$ -stages 5.3-3 are used to fine-tune the rotation centre of 5.3-4, to make this centred vertically straight above 5.3-1. Linear stage 5.3-5 is responsible for centring the sample surface straight above rotation centres of 5.3-1 and 5.3-4. The position of 5.3-5 depends on the thickness of the sample chip. This does not vary between samples, and hence in principle 5.3-3 and 5.3-5 require to be calibrated only once.

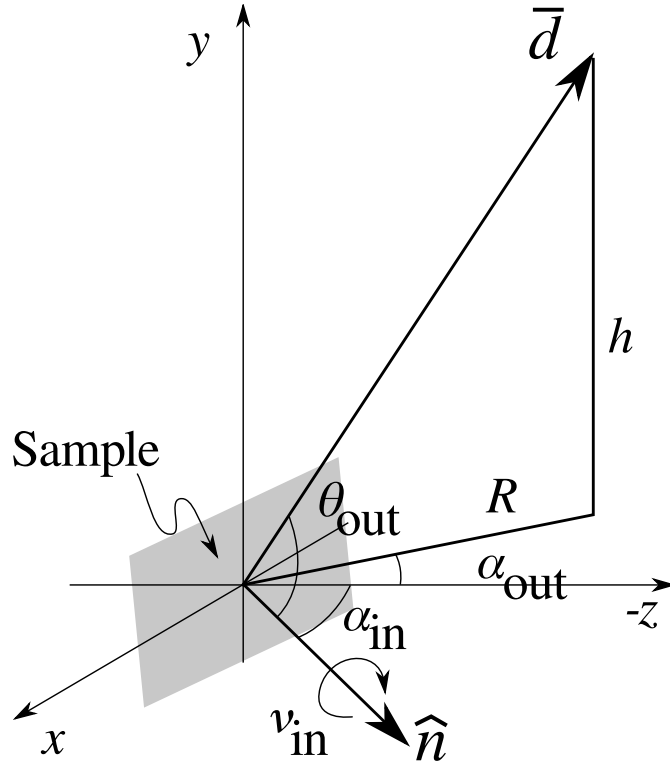


**Figure 5.2:** Angles in the diffraction set-up.

Part	Description
1	Holder of optics for detection of diffracted beam. This angle is denoted $\alpha_{\text{out}}$ . At the end of the arm is mounted either a linear scale used for measuring $h$ or a collector lens coupling light to a fibre to a spectrometer for intensity measurement.
2	Vertical displacement of sample holder to allow for independent variation of $\alpha_{\text{in}}$ and $\alpha_{\text{out}}$ .
3	Alignment table to centre $\alpha_{\text{in}}$ vertically over $\alpha_{\text{out}}$ .
4	Rotation table controlling $\alpha_{\text{in}}$ .
5	Alignment table to align sample surface vertically over $\alpha_{\text{in}}$ and $\alpha_{\text{out}}$ .
6	Magnetic table for mounting magnetic probe holders for contacting tunable CNF PC.
7	Rotation table controlling $\nu_{\text{in}}$ .
8	Electrical contacts for actuation probes.
9	Alignment table for aligning sample centre over rotation table $\nu_{\text{in}}$ centre.
10	Optional 10x magnification lens with built-in light-source for contacting probes.
11	The sample.

**Table 5.1:** Description of the different parts of the diffraction holder, displayed in figure 5.3.

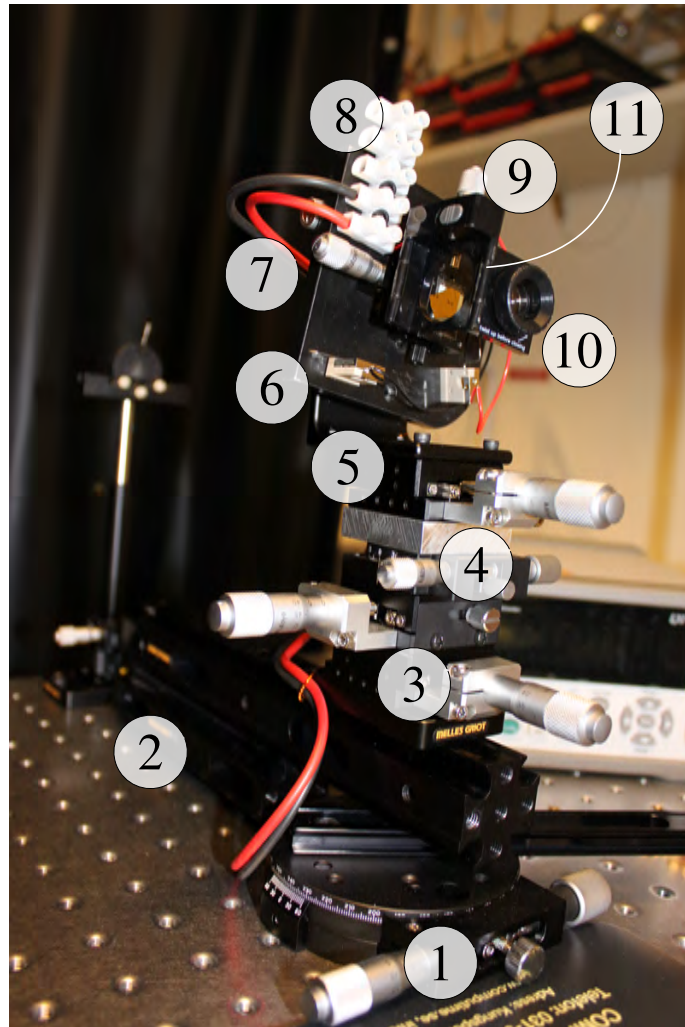


**Figure 5.3:** *The sample holder in the diffraction set-up. Each number is described in table 5.1.*

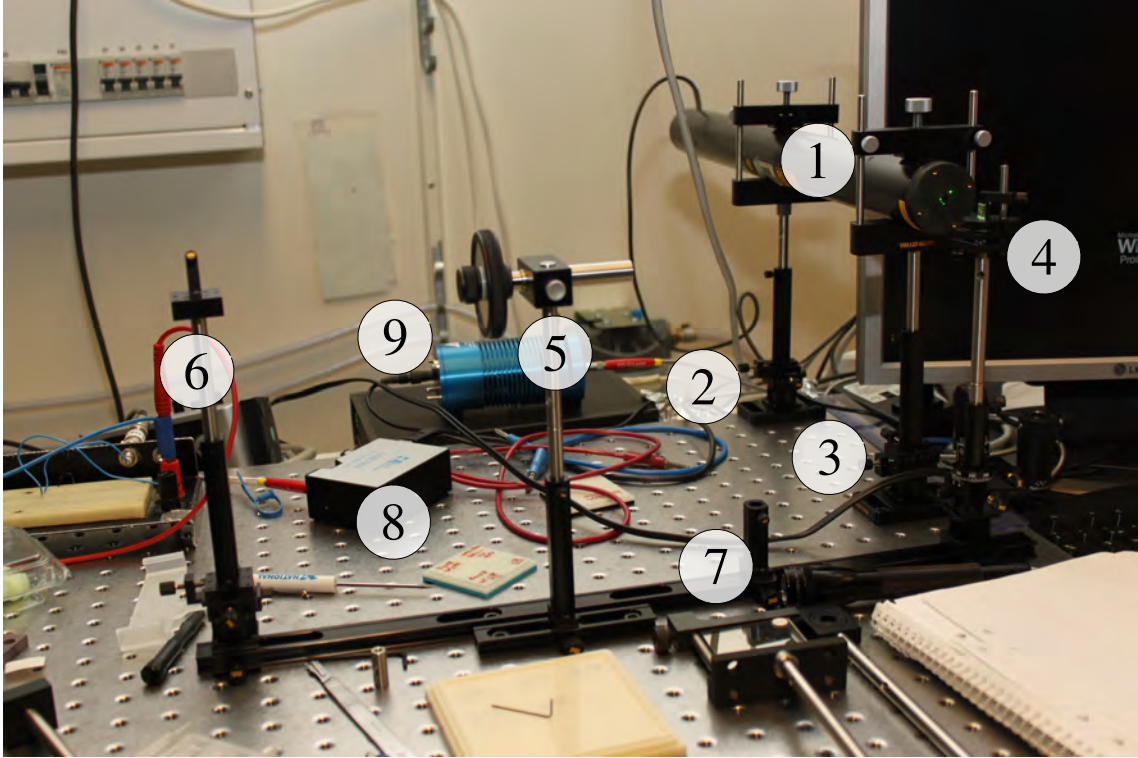


**Figure 5.4:** Optical components in the incoming light path. Each number is described in table 5.2.

Part	Description
1	542 nm HeNe-laser.
2	Back laser holder including $xyz$ linear stages for laser alignment.
3	Front laser holder including $xyz$ linear stages for laser alignment.
4	Mirror for beam deflection including $xyz\varphi\Theta$ stages for beam alignment.
5	Neutral density-filter (Nd-filter) for controlling laser intensity on sample.
6	Aperture for controlling beam width and stray light, including $xyz$ linear stages for aperture alignment.
7	Extra holder for additional optical components, including extra ND filter, polariser and beam stop.
8	Spectrometer for detecting intensity of outgoing beam.
9	Optional white light source to replace the laser.

**Table 5.2:** Description of the different optical components along the incoming light path. The components are displayed in figure 5.4.

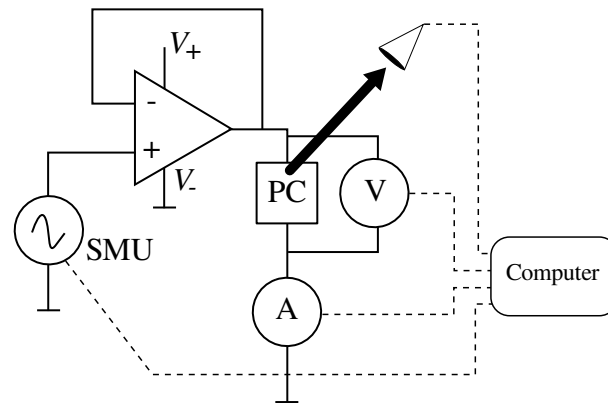


**Figure 5.5:** *The electrical network used to power and analyse the PC.*

The laser spot has to hit the centre of rotation of the rotation stage 5.3-7. This is achieved by adjusting the laser holders 5.4-2 and 5.4-3. The height from the optical table to the centre of rotation of 5.3-7 is measured. The laser output is set to the same value by adjusting the front pole holder 5.4-3. Next the beam is made parallel to the table by measuring the beam height at a distance away from the table and adjusting the beam direction using 5.4-2. The mirror 5.4-4 is mounted and the procedure for aligning the beam to the table is repeated. Also rotation is used to align the beam to hit the centre of 5.3-7. Finally stray light is removed using aperture 5.4-6.

Samples are held on the sample holder using simple double-sided tape. The sample chip is mounted and centred using  $xy$  linear stages 5.3-9 to have the sample region aligned with the beam and  $\nu$  rotation centre 5.3-7.

The equipment used in the lab is mainly from CVI Melles Griot's MicroLab series. These provide compact opto-mechanical components. However, the  $z$  stage in the integrated  $xyz$  linear stages is very unstable. I would discourage from using it in any set-up that requires high accuracy.

## Electrical set up for tunable CNF-PCs

After CNF growth, the resistivity on the sample surface decreases significantly. This is believed to be due to amorphous carbon deposition on the surface. For non-electrically connected samples the deposition is not an issue. However, on samples with actuation, where there are parts on the surface that should be electrically isolated this becomes problematic. Typically on the samples investigated in this work resistance between contacting pads (see figure 6.27) changes from  $R \approx 10^4 \Omega$  before growth to  $R \approx 10^2 \Omega$  after growth.

Due to the low resistance, applying a voltage on the PC samples drains a significant current from the voltage source. The source-measure-unit (SMU) available in the lab cannot deliver the current required and hence a power amplifier has to be used. The amplifier used in the experiments is simply a high power operational amplifier (actually several op-amps connected in parallel) connected as a voltage follower. This works very well and is a simple way to construct a power amplifier. The whole electrical set-up is depicted in figure 5.5.

## Optical noise

The intensity measurements are very noise sensitive. The main source of noise is mechanical vibrations in the building, partially from the ventilation system. To minimise this, the optical table is mounted on damping cushions and measurements are performed without any person moving in the room. In particular the optical fibre should be protected from any mechanical vibrations. This is done by clamping it to the optical table and minimising cables between instruments with moving parts and the optical table. This issue is particularly important when looking at the tunable structures where very small intensity variations are measured.

## 5.2 Ellipsometry

Ellipsometry is a technique for recording polarisation changes in a light beam interacting with a sample. An in-depth introduction to the subject can be found in the "Handbook of Ellipsometry" [102]. The basic idea in reflection ellipsometry is to irradiate a surface with a light beam of one or several frequencies, with a well defined polarisation state and inclination angle, but not necessarily coherent. By recording the polarisation state of the specular beam, much information about the surface can be extracted.

In standard ellipsometry, the measured quantity is

$$\rho = \frac{R_p}{R_s} = \tan \Psi e^{i\Delta},$$

where  $R_p$  and  $R_s$  are the complex valued Fresnel reflection coefficients for  $p$ - and  $s$ -polarisations, respectively [61]. It is assumed that there is no conversion between polarisation states in the interaction with the surface. The last equality expresses  $\rho$  as two angles conventionally used in ellipsometry. The magnitude difference between  $R_p$  and  $R_s$  is captured by  $\Psi \in [0, \pi/2]$  while  $\Delta \in [0, 2\pi]$  contains the phase difference. By measuring the ratio and not  $R_p$  or  $R_s$  directly the technique becomes very robust. There is in general no problem to perform measurements in the visible region in a well-lit room since noise cancels out in the quotient.

### The basic ellipsometry set up

A reflection ellipsometry measurement starts by preparing a well defined polarised state from a regular white light source by using a polariser and possibly a compensator (or phase retarder). A compensator is a device that delays the phase of one of the polarisations compared to the other. This device can be realized by a material with birefringence, e.g. quartz. Next, the polar and azimuthal angles of light inclination and detection are set, see figure 5.7. Depending on how many elements of the Jones and/or Mueller matrix one is interested in, different levels of complication are required in the detection (and source). To obtain the full Mueller matrix, the polarisers and compensators on both the radiation source and the detector have to rotate in relation to each other and the sample. The ellipsometer used here was the VASE from J.A. Woollam Co. [103] which is a computer controlled commercial instrument where no manual parameter control is required.

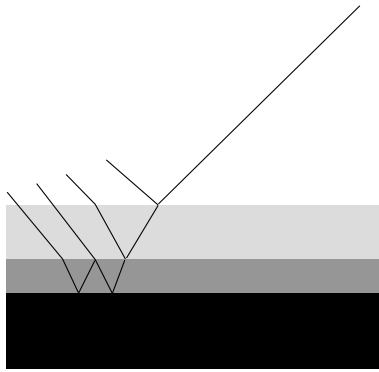


**Figure 5.6:** Reflection against a stack for three material interfaces. At each interface there is a reflection governed by the Fresnel equations. All these add up to a total reflection coefficient which is probed in the ellipsometry set-up. Not all of the reflections are depicted in the sketch.

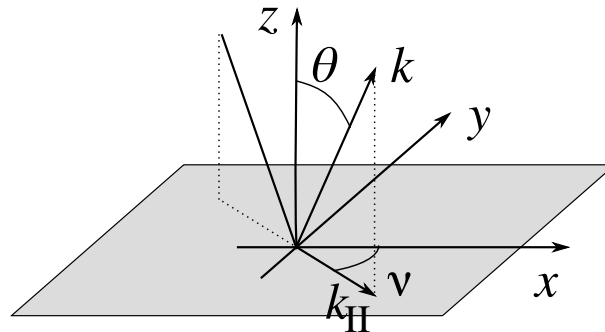


**Figure 5.7:** Relevant geometric quantities in an ellipsometry measurement.

If there are multiple interfaces, as depicted in figure 5.6, multiple reflections occur. Equation (2.16) can be used to build up the resulting outgoing polarisation state after the interaction with the material. The resulting matrix  $M_j^{tot}$  can then be related to the measured  $\rho$  via the Fresnel equations and some *a-priori* knowledge of the material stack such as layer thickness and/or dielectric functions. Missing material parameters can be extracted by fitting procedures (this is the most common use of ellipsometry measurements). There are commercial programs available to perform this kind of analysis. Ellipsometry was used in Papers II and IV to characterise the optical properties of CNF-PCs.

# Chapter 6

## Introduction to and summary of appended papers

This thesis summarises the work contained in four papers published during my time as a PhD student. The papers are of slightly different characters but describe a coherent progression towards the understanding and realisation of tunable CNF-based PCs. Paper I is a purely theoretical work where it is shown that tunability can be achieved via the electrostatic actuation scheme suggested and in principle detected in the kind of systems under consideration. It also provides some insight into how a displaced lattice affects the band structure. Modelling was performed using FDTD and analytical methods. Paper II mainly consists of experimental work where the optical properties of static structures were investigated using ellipsometry. FDTD provided the theoretical framework for describing features in the detected spectrum. It was found that ellipsometry is a powerful tool to study PCs. In Paper III the diffractive properties of static structures were investigated experimentally and modelled using FDTD and simple diffraction and interference theory. It complements the ellipsometric results in Paper II which focus on the specular beam. Papers I-III serve as a foundation for the observations performed in Paper IV on tunable structures. Finally, Paper IV covers measurements on tunable VACNF-based PC.

### 6.1 Paper I – Nanowire-based tunable photonic crystals

Paper I studies theoretically and consecutively one, two and three dimensional tunable PC systems where tunability is achieved by mechanical deformation, starting with a 1D crude model to obtain an initial understanding.

#### One-dimensional case

The 1D system under consideration is depicted in figure 6.1 and consists of two potentials that can be shifted in position relative to each other. The shift is denoted  $d$ , and setting  $d = 0$  corresponds to the undisturbed system where the unit cell is built up from two identical parts and the lattice is periodic with period  $a$ . To get a qualitative idea of how a shift  $d$  in the basis of the lattice affects the dispersion relation in the system, the dispersion relation for the Kronig–Penney model is calculated using the transfer matrix method ,

see figure 6.1 depicting the dielectric function.<sup>1</sup> The equation to solve is Hill's equation, equation (2.6) with

$$f(x) = \frac{\omega^2}{c^2} \varepsilon(x) = \frac{\omega^2}{c^2} n^2(x).$$

The transfer matrix method is used to solve this piecewise constant potential differential

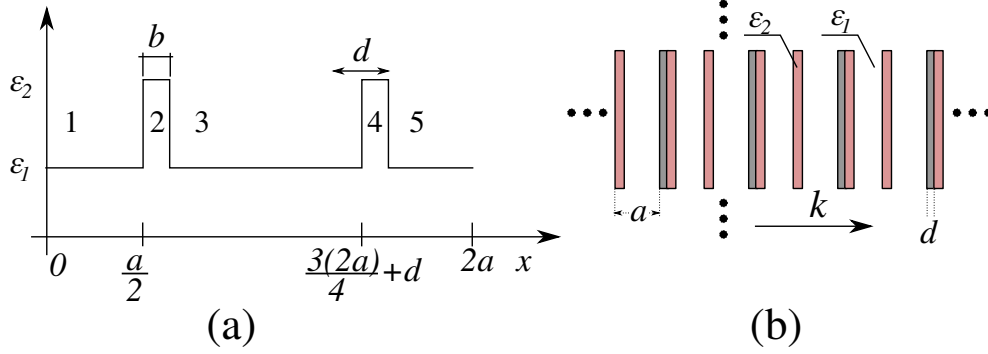


**Figure 6.1:** Model system in one dimension. (a) one unit cell and (b) schematic illustration of the whole system.  $2a$  is the period of the system,  $b$  the width of the high- $\varepsilon$  regions and  $d$  the shift of the second high- $\varepsilon$  region.

equation. The regions of constant  $\varepsilon$  in figure 6.1 are numbered 1 to 5. In a region  $i$ , the amplitudes of the two independent solutions,  $e^{ikx}$  and  $e^{-ikx}$  are denoted  $A_i$  and  $B_i$  respectively. These are placed in a column vector:

$$v_i = \begin{pmatrix} A_i \\ B_i \end{pmatrix}.$$

Propagation through the system can then be described as matrix operations on  $v_i$ . The unit cell in the PC is depicted in figure 6.1 and only normal incidence is considered. E-field boundary conditions require that the field should be continuous at the boundary between regions of different dielectric constant, that is

$$E(\text{bound}^-) = E(\text{bound}^+) \quad (6.1)$$

and the derivative must also be continuous

$$\left. \frac{dE}{dx} \right|_{\text{bound}^-} = \left. \frac{dE}{dx} \right|_{\text{bound}^+}. \quad (6.2)$$

For the transfer between the first and second region in figure 6.1(a), equations (6.1) and (6.2) give

$$A_1 e^{ik_1 x_0} + B_1 e^{-ik_1 x_0} = A_2 e^{ik_2 x_0} + B_2 e^{-ik_2 x_0} \quad (6.3)$$

$$n_1 (A_1 e^{ik_1 x_0} - B_1 e^{-ik_1 x_0}) = n_2 (A_2 e^{ik_2 x_0} - B_2 e^{-ik_2 x_0}), \quad (6.4)$$

<sup>1</sup>It is noteworthy to point out that this model was introduced to describe ordinary crystals where it is a very crude approximation. In PCs, however, it is actually much better since PCs most of the time consist of slabs of dielectrics put together which gives step-like changes in the "potential".

where  $k_i = \omega^2 n_i^2 / c_0^2$  and  $x_0 = a/2$ . This can be written in matrix form, using  $v_i$ , as

$$\begin{pmatrix} 1 & 1 \\ n_1 & -n_1 \end{pmatrix} \begin{pmatrix} e^{ik_1 x_0} & 0 \\ 0 & e^{-ik_1 x_0} \end{pmatrix} \begin{pmatrix} A_1 \\ B_1 \end{pmatrix} = \begin{pmatrix} 1 & 1 \\ n_2 & -n_2 \end{pmatrix} \begin{pmatrix} e^{ik_2 x_0} & 0 \\ 0 & e^{-ik_2 x_0} \end{pmatrix} \begin{pmatrix} A_2 \\ B_2 \end{pmatrix}. \quad (6.5)$$

Matrices containing refractive indices will be called *refractive matrices* and matrices containing phase factors *phase matrices*. Next the matrices on the right can be inverted to give an expression for  $A_2$  and  $B_2$  in terms of  $A_1$  and  $B_1$ . Putting together the two refractive matrices and replacing  $x_0$  by  $a/2$  gives

$$\begin{pmatrix} e^{-ik_2 a/2} & 0 \\ 0 & e^{ik_2 a/2} \end{pmatrix} \frac{1}{2n_2} \begin{pmatrix} n_2 + n_1 & n_2 - n_1 \\ n_2 - n_1 & n_2 + n_1 \end{pmatrix} \begin{pmatrix} e^{ik_1 a/2} & 0 \\ 0 & e^{-ik_1 a/2} \end{pmatrix} \begin{pmatrix} A_1 \\ B_1 \end{pmatrix} = \begin{pmatrix} A_2 \\ B_2 \end{pmatrix} \quad (6.6)$$

Equation (6.6) provides a way to get amplitudes for the two solutions  $e^{ikx}$  and  $e^{-ikx}$  in region 2 provided amplitudes in region 1 are known.

The same type of equations as (6.3) and (6.4) can be set up at the interface in the point  $a/2 + b$ , and then be rewritten as a matrix equation in the same manner as (6.6). This yields

$$\begin{pmatrix} e^{-ik_1(a/2+b)} & 0 \\ 0 & e^{ik_1(a/2+b)} \end{pmatrix} \frac{1}{2n_1} \begin{pmatrix} n_1 + n_2 & n_1 - n_2 \\ n_1 - n_2 & n_1 + n_2 \end{pmatrix} \begin{pmatrix} e^{ik_2(a/2+b)} & 0 \\ 0 & e^{-ik_2(a/2+b)} \end{pmatrix} \begin{pmatrix} A_2 \\ B_2 \end{pmatrix} = \begin{pmatrix} A_3 \\ B_3 \end{pmatrix} \quad (6.7)$$

Similarly, all solutions between steps in the dielectric function can be joined. After this, equations like (6.6) and (6.7) can be put together to relate fields in regions furthest apart. The result after moving from the left in the first low  $\varepsilon$  region to the right in the second low  $\varepsilon$  region in figure 6.1 results in a matrix equation relating the field at point  $x = 0^+$  and the point  $x = (3\frac{2a}{4} + d)^-$ :

$$\begin{pmatrix} e^{-ik_1(a/2-b+d)} & 0 \\ 0 & e^{ik_1(a/2-b+d)} \end{pmatrix} \frac{1}{2n_1} \begin{pmatrix} n_1 + n_2 & n_1 - n_2 \\ n_1 - n_2 & n_1 + n_2 \end{pmatrix} \begin{pmatrix} e^{ik_2 b} & 0 \\ 0 & e^{-ik_2 b} \end{pmatrix} \frac{1}{2n_2} \begin{pmatrix} n_2 + n_1 & n_2 - n_1 \\ n_2 - n_1 & n_2 + n_1 \end{pmatrix} \begin{pmatrix} e^{ik_1 a/2} & 0 \\ 0 & e^{-ik_1 a/2} \end{pmatrix} \begin{pmatrix} A_1 \\ B_1 \end{pmatrix} = \begin{pmatrix} A_3 \\ B_3 \end{pmatrix} \quad (6.8)$$

Denote the matrix in the middle row  $M$ . It is given by

$$M = \frac{1}{4n_1 n_2} \begin{pmatrix} (n_1 + n_2)^2 e^{ik_2 b} - (n_1 - n_2)^2 e^{-ik_2 b} & 2i(n_2^2 - n_1^2) \sin k_2 b \\ 2i(n_1^2 - n_2^2) \sin k_2 b & (n_1 + n_2)^2 e^{-ik_2 b} - (n_1 - n_2)^2 e^{ik_2 b} \end{pmatrix}.$$

This matrix can be simplified by taking the limit where  $b \rightarrow 0$  while  $\varepsilon b = C = \text{constant}$ . This makes the high- $\varepsilon$  layers in figure 6.1 become delta-functions. The matrix  $M$  then takes the form

$$M = \begin{pmatrix} 1 + i\frac{1}{2n_1}C & i\frac{1}{2n_1}C \\ -i\frac{1}{2n_1}C & 1 - i\frac{1}{2n_1}C \end{pmatrix}.$$

By applying the same calculation through the whole structure, the full matrix for the unit cell looks like

$$\begin{aligned} \begin{pmatrix} A_5 \\ B_5 \end{pmatrix} &= \\ v_5 = T v_1 &= \begin{pmatrix} e^{-ik_1(2a/4-d)} & 0 \\ 0 & e^{ik_1(2a/4-d)} \end{pmatrix} \\ M \begin{pmatrix} e^{ik_1(a+d)} & 0 \\ 0 & e^{-ik_1(a+d)} \end{pmatrix} M \begin{pmatrix} e^{ik_1 2a/4} & 0 \\ 0 & e^{-ik_1 2a/4} \end{pmatrix} \begin{pmatrix} A_1 \\ B_1 \end{pmatrix} & \end{aligned} \quad (6.9)$$

Now a physical interpretation can be assigned to the different matrices. We start with the amplitudes  $v_1$  and then we propagate these with the first phase matrix a distance  $2a/4$  in a medium with constant refractive index  $n_1$  (resulting in "wavevector"  $k_1$ ). Then the field hits the delta-functions and gets some additional phase due to this. But the wave also gets reflected at these points, thereby changing the amplitudes. Next it propagates between the two delta-functions, and so on.

To be able to find the eigensolutions to the system, Bloch's theorem can be used to relate the fields in the two points  $x = 0$  and  $x = 2a$ . This gives us one more equation relating  $v_1$  and  $v_2$ . The theorem says that

$$E(x + 2a) = e^{iK2a} E(x), \quad (6.10)$$

which gives that also

$$\frac{dE}{dx}(x + 2a) = e^{iK2a} \frac{dE}{dx}(x). \quad (6.11)$$

In matrix form, using  $v_i$ , this becomes

$$v_5 = e^{iK2a} v_1.$$

Putting this together with (6.9) gives an eigenvalue equation

$$T v_1 = e^{iK2a} v_1, \quad (6.12)$$

with  $T$  depending on  $\omega$  and the dielectric constants. The eigenvalues of  $T$  give the Bloch wavevectors depending on frequency. Following Yeh [72] and expressing  $T$  as

$$T = \begin{pmatrix} A & B \\ C & D \end{pmatrix} \quad (6.13)$$

and then noting that the matrix  $T$  is unimodular, that is,  $\det T = 1$ , we get that

$$e^{iK2a} = \frac{1}{2}(A + D) \pm \sqrt{\left(\frac{1}{2}(A + D)\right)^2 - 1},$$

and further, via the fact that the product of the two roots of this equation equals 1,

$$K = \frac{1}{2a} \cos^{-1} \frac{1}{2}(A + D). \quad (6.14)$$

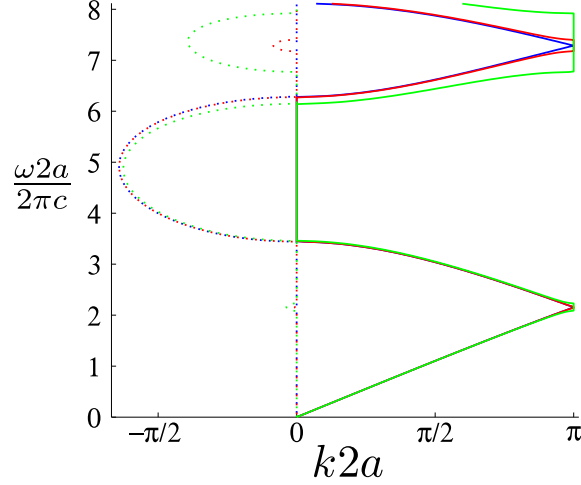


**Figure 6.2:** Result from the transfer matrix analysis in a limit of the Kronig-Penney model. Solid line represents real part of  $K(\omega)$  and dashed represents imaginary part. Blue line corresponds to a displacement  $d = 0$ , red  $d = 0.01$  and green  $d = 0.05$ .

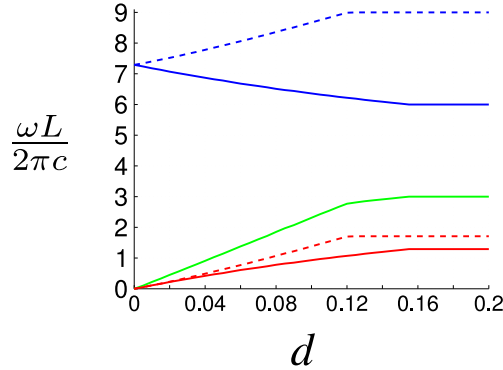


**Figure 6.3:** Scaling of the second gap that opens around  $\omega 2a/2\pi c \sim 7$  using a one-dimensional Kronig-Penney model. Blue solid and dashed lines are lower and upper band edge, green is total gap width and the red curves represent lower and upper band edges from the centre frequency  $\omega \simeq 7.3$  in absolute numbers. It can be seen that the upper band edge increases more than the lower decreases.

Explicitly written out, equation (6.14) gives

$$\cos(K2a) = \cos(n_1 2a\omega/c) - \frac{C\omega}{n_1 c} \sin(n_1 2a\omega/c) + \frac{C^2 \omega^2}{4n_1^2 c^2} [\cos(n_1 2d\omega/c) - \cos(n_1 2a\omega/c)]. \quad (6.15)$$

The result from plotting for  $n_2^2 b = C = 0.5$  is depicted in figure 6.2. Remember that  $b$  denotes the width of the high-index region, see figure 6.1(a), and  $n_2$  the refractive index of that region.  $C$  is thus a measure of the size of the potential well.

For  $d = 0$  there is no bandgap at  $K = \pi$  (for  $k$  normalised with  $2a$ ), which is expected since the lattice period is actually  $a$ , so we expect the first gap to appear at  $K = 2\pi$ , which in the reduced zone becomes  $K = 0$ . For a small value of  $d$ , a small gap opens at  $K = \pi$ . This is depicted by  $K$  becoming imaginary in this region, which corresponds to damped modes.

Also the next gap that was closed for  $d = 0$  at  $K = \pi$  can be seen to open up for  $d \neq 0$ . Here the effect of the shift is much stronger and  $K$  obtains a large imaginary part. The dependence is seen to increase for higher bands. This can be explained in the following way: In the  $\delta$ -function model essentially what we have is a system with two potential wells of the same depth but different widths, separated by delta functions. In each well there are modes coming from the boundary conditions of reflecting on the delta functions. A solution in one of the regions is (from earlier)

$$E_n(x) = A_n e^{ik_n x} + B_n e^{-ik_n x},$$

with

$$k_n^{-1} = \frac{c}{\omega n}.$$

It can be seen that for higher frequency this is a faster oscillating function with the period determined by  $k^{-1}$ . When the width of the well is changing, it can be expected that the solution amplitudes will be more sensitive the shorter the "wavelength"  $k^{-1}$  in the well is. Since moving one of the delta functions will create one well that is wider and one that is narrower we could expect both shorter and longer wavelengths should be affected, and indeed, the gaps open both to higher and lower frequencies. If looking closer at e.g. the first gap at  $K = 0$  the upper band edge is affected more, see figure 6.3. This follows also from the reasoning since higher frequency means shorter  $k^{-1}$  which means more sensitive to changes. The sensitivity can also be read from equation (6.15) where  $d$  multiplies  $\omega$ , so for higher frequencies the effect in the  $\cos(2d\omega/c)$  term will be stronger for higher  $\omega$ .

For the first bandgap at  $K = 0$  it can be seen that it is slightly affected by the shift. This might also be an interesting region to work in; we have a fully developed stopband and when making a small shift the band edge is slightly shifted in frequency with the lattice deformation. This should provide for very fine frequency switching. After looking at this simple model system we have an idea of what to expect in two dimensions.

## Two-dimensional case

In two dimensions it is not possible to use analytical methods in the same way as was done in one dimension. Instead FDTD is used to investigate the optical properties and in particular transmission coefficients interest us. Inherent in the FDTD method is that it is not possible to work with truly infinite systems, but instead slabs are considered.

A setup consisting of  $m$  fibres in the  $x$ -direction, as depicted in figure 6.4, is considered. In the  $y$ -direction periodic boundary conditions are used, thereby simulating an infinite system in this direction. This makes it possible to work with true plane waves as the incoming radiation in the simulation.

The transmission coefficient is defined as the ratio between the incoming and transmitted fluxes through the system. The system is excited from the left, see figure 6.4, at the

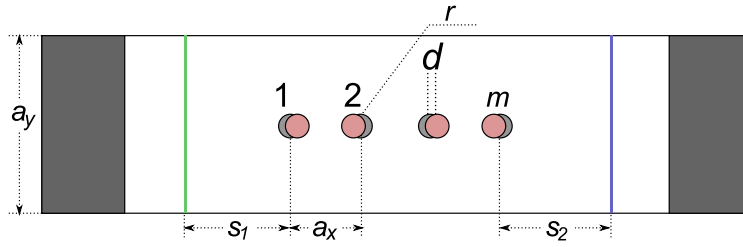


**Figure 6.4:** The set-up of the 2D FDTD simulation.  $m$  denotes the number of fibres,  $a_x$  and  $a_y$  the lattice constant in each dimension. The shaded areas in the ends in the  $x$ -direction are PMLs. The green line denotes the source and the blue the observation plane. Between the source and the beginning of the PC there is a distance to guarantee that the PC structures do not affect the coupling of modes from the source to the computational grid. There is also a distance between the PC and the observation plane.

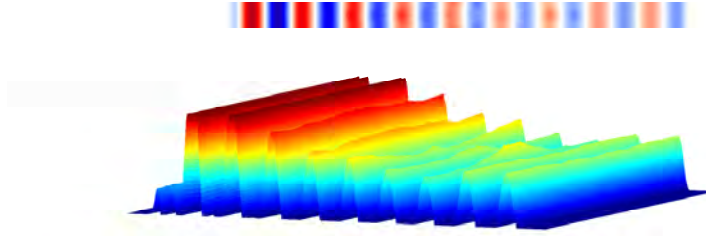


**Figure 6.5:** Field-pattern from an FDTD calculation displayed as an image and as a surface. In the lower plot only the positive amplitude is displayed to make it clearer.

green line by a current source. In the following only E polarised light is considered, that is light with the electric field perpendicular to the plane shown in figure 6.4 (parallel to the infinite rods in the  $z$ -direction). The transmitted flux is recorded where the blue line is depicted to the right in figure 6.4. The field from a typical run is shown in figure 6.5. In the figure, different regions can be seen: There is a strong field region near the source. To the left of the source the field quickly decays into the PML. In the middle there is a region with a lower amplitude which is in the PC. It can be seen that apart from parts of the power being reflected, the amplitude is also concentrated towards the high- $\epsilon$  regions, that is, the cylinders in the middle of the figure. To the right of the PC is the right air frame and, then finally the PML damping out the fields. It can further be seen that the PC slab is not thick enough to behave as a crystal. The field pattern is different for each period through the slab indicating that the field has not reached steady state yet, that is, the field pattern is not in Bloch modes which are the eigenmodes of an infinite PC system.

In the following sections, the transmission dependence of parameters like CNF width and dielectric constant are discussed. The focus is on the behaviour around the band gap, in dimensionless frequency, centred around  $\omega = 1$ . The band gap centre is not exactly at 1 since the presence of the rods shifts the gap. The larger the dielectric constant and the filling factor, the larger the shift. These first parameters have been studied earlier, but are displayed here for completeness. In the following we look only at the square lattice case where  $a_x = a_y = a$ . If not stated otherwise, the parameters used in all computations are the ones displayed in table 6.1. In the simulations performed there is no difference between

Fundamental working unit	1 $\mu\text{m}$
Lattice constant, $a$	0.5 $\mu\text{m}$ .
CNF radius, $r$	25 nm.
Dielectric constant, dielectrics	10
Dielectric constant, metals	$-\infty$
PML-layer	1 $\mu\text{m}$ .
Distance between source and PC	10 $\mu\text{m}$ .
Light polarisation	E
Number of CNFs considered, 2D	10
Number of CNFs considered, 3D	4
Resolution	256 pixels/ $\mu\text{m}$

**Table 6.1:** *Compilation of parameters used in the FDTD computations.*

results from computations at resolutions of 128 and 256 pixels/ $\mu\text{m}$ , and 256 pixels/ $\mu\text{m}$  are used. Frequency dependent dielectrics are not considered in this work. The lower number of CNFs in three dimensions is due to computational limitations.

### Transmission dependence of crystal thickness

One important parameter to play with in these structures is the number of unit cells to use,  $m/2$  in figure 6.4. In particular it becomes more important when dealing with metallic structures that will always have at least a small imaginary part in the dielectric function, resulting in losses. Therefore there will be a trade-off between switching sharpness and damping in the transparent regime. A thicker PC (larger  $m$ ) will give more pronounced band gaps but, at the same time, increase damping for propagating modes. In figure 6.6 the transition from slab to crystal behaviour is displayed. The transition depends on the dielectric constant, which is also apparent in the figure, and the transition is faster in the metallic case than in the dielectric.

In the bandgap the wave at a particular frequency is damped out exponentially with distance so that the amplitude of the field in the PC goes as

$$E_s(\omega) \sim e^{-s/s_0(\omega)},$$

where  $s$  is the travelled distance and  $s_0(\omega)$  denotes some characteristic distance of damping in the system. In the passband region on the other hand, the exponential damping factor is not present (ignoring imaginary parts of  $\varepsilon$ ). Instead a decrease in amplitude is due to coupling between the PC eigenmode and the air eigenmode. This only occurs at the boundary between the PC and air and results in a constant decrease in amplitude, independent of PC thickness.

As an introductory example, consider the result in figure 6.6. There are two different numerical artefacts in the plots which should be noted. First in the dielectric case there is an enhanced transmission around the band gap. This is due to a change in the LDOS due to the presence of the PC and therefore more power is injected into the simulation from the source. In turn, this is due to a too small distance between the current source and the PC. In the depicted simulation a shorter distance than the value of 10  $\mu\text{m}$  as stated in table 6.1 has been used. This illustrates the importance of a large enough distance between

source and structures that changes between runs. Despite this the result is qualitatively correct. Since a transmission larger than one is un-physical this problem is often easily detected and can be corrected by increasing the source-PC distance if quantitative results are required. In the metallic case the transmission goes above 1 for the lower frequencies. This is due to the field amplitudes being very low here. The figure illustrates the problem of trying to use too much of the bandwidth in the pulse to get transmission information. To get transmission coefficients for a broad band of frequencies typically 2-5 runs (with corresponding normalisation runs) with different centre frequencies of the Gaussian pulse have to be run and then joined together.

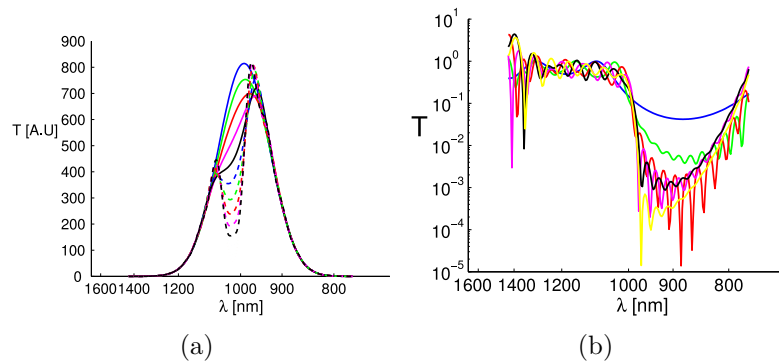


**Figure 6.6:** *Scaling of the PC slab behaviour with the number of fibres in (a) dielectric and (b) metallic case. Curves start with 4 fibres and increase with two in each curve in the order: solid blue, green, red, pink black, dashed blue, green, red, pink, black. In the dielectric case the transmission is not normalised with the incoming power, therefore the Gaussian shape of the pulse is seen. The stopband appearing is clearly seen. In the metallic case the plot is logarithmic to make the difference clearer.*

It is also clear when looking at the two curves in 6.6 that the bandgaps in the two cases are placed at different energies. This comes from the fact that the dielectric constant is different in the two cases. The position of the bandgap moves with the dielectric.

### Transmission dependence of CNF radius

The CNF radius is controlled via the size of the catalyst particle. It is not possible to change the diameter very much. Too small catalyst particles result in poor growth, while too large particles result in growth of several CNFs from a single catalyst dot, which is undesirable, see chapter 4 for a more complete discussion. In the simulations performed the only case considered is a radius of 25 nm. A larger filling factor generally increases the sensitivity of a PC, which is desirable. Therefore a larger radius would be beneficial. For CNFs it can probably be increased to 40 nm in a controllable way. There are also other nanowires that are possible to fabricate with a larger radius that might be interesting in future applications.

### Transmission change due to lattice change

In a computer simulation, CNFs placed on the computational grid can be moved around in any way one is interested in and then transmission properties can be studied as described

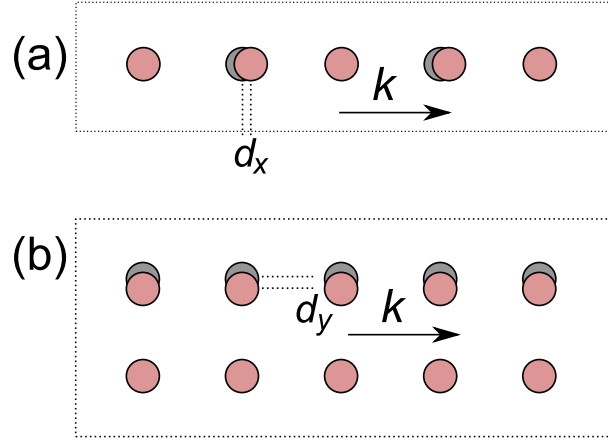


**Figure 6.7:** One unit cell row of the modified PC in two dimensions. We consider the two situations where the CNFs are shifted in either the propagation direction (a) or in the transverse direction (b).

previously. This is, however, not consistent with possible experimental realisations. In an experiment typically to bend a CNF, a voltage is applied to it, and then some other object is grounded to provide electrostatic attraction between the CNF and the other object, thereby bending it. To bend all CNFs in a lattice there are of course many ways to connect voltages. In this work the two most obvious such ways have been studied: Ground the substrate and apply  $\pm V$  volt to each second row pair, either in the direction of propagation or perpendicular to the direction of propagation, see figure 6.7.

In two dimensions the above described experimental set-up is modelled by a change in the lattice from simple square to rectangular with a basis, see figure 6.7. The curvature when bending the CNFs can not be captured in 2D. Instead the whole rod is shifted a distance  $d$  from its original position, either for the propagation direction (figure 6.7(a)) or perpendicular to the propagation direction (figure 6.7(b)). Bending is included in the full three-dimensional simulation described later.

Due to the small radius of the rods, the distortion from a free wave is very small in the CNF PCs considered. There is a small gap at the zone boundary, located at a normalised frequency  $\omega \simeq 0.5$ . This roughly corresponds to a vacuum wavelength of  $\lambda \simeq 1000$  nm if the lattice constant is set to 500 nm. The next gap in the undisturbed system is located around  $\lambda \simeq 500$  nm. If a distortion is introduced so that the unit cell doubles in, say, the  $x$ -direction a gap appears between the  $\Gamma$ - and the M-points in the band diagram. This corresponds to frequencies  $\omega \simeq 0.25$  and  $0.75$ . It should be stated that when discussing band gaps here, the general definition of a band gap, where there are no frequency modes for any wavevector or polarisation in a frequency region, is not used. Rather what is meant here is that at the BZ edge there is a frequency span  $\omega_1 - \omega_2$  in which there are no available states for a particular polarisation. To open up true band gaps other geometries must be considered.

For a system with lattice constant  $a$  the first band gap appears at  $k_{\text{Bloch}} = \pi/a$ . If this is translated to a vacuum wavelength this gives  $\lambda = 2a$ . This is not exactly true since there is no exact correspondence between the vacuum wavelength and the Bloch wavevector, but it is used as a rule of thumb when selecting what frequencies to excite the system with. For the first bandgap opening in one dimension it could be seen that the effect of

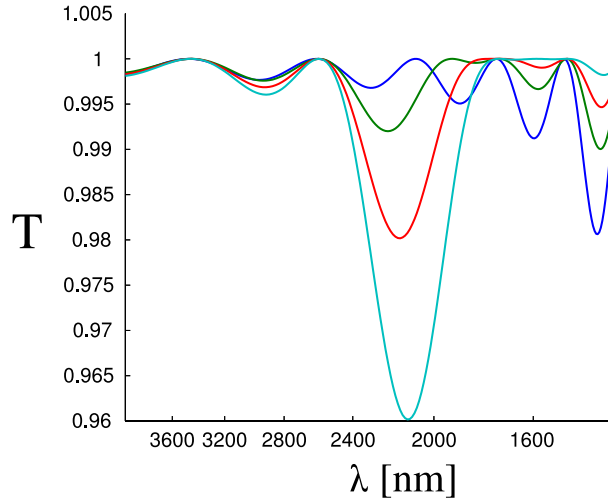


**Figure 6.8:** First gap opening for a ten rows of CNFs modelled as dielectrics with  $\epsilon = 10$  with a diameter of 50 nm and an undisturbed lattice spacing of 500 nm. The curves correspond to a shift  $d$  as displayed in fig. 6.7 of: 0 nm (blue), 20 nm (green), 40 nm (red), 60 nm (light blue). The curve is plotted against vacuum wavelength instead of frequency to make the interpretation more clear.

a lattice distortion was rather weak. The same thing is seen in two dimensions where the effect from a shift is weak around the first bandgap that opens, see figure 6.8. Therefore focus is on higher frequencies.

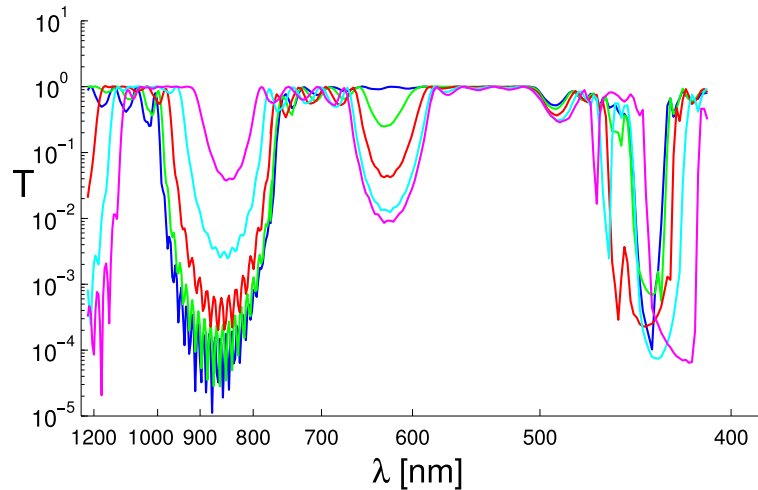


**Figure 6.9:** Change in transmission due to a lattice deformation in the propagation direction. The lattice is composed of ten rows of CNFs modelled as perfect metals with a diameter of 50 nm and a lattice spacing of 500 nm. The curves correspond to a shift  $d$  as displayed in fig. 6.7(a) of: 0 nm (blue), 20 nm (green), 40 nm (red), 60 nm (light blue), 80 nm (magenta). The curve is plotted against vacuum wavelength instead of frequency to make the interpretation more clear.

Results for the perfect metallic case with shift in the propagation direction are shown in figure 6.9. The dielectric case is shown in figure 6.10. The results for a transverse shift in the metallic system are depicted in figure 6.11. For the metallic PCs the transmission drops to zero in the long wavelength limit. This is not seen in the figures, but appears for

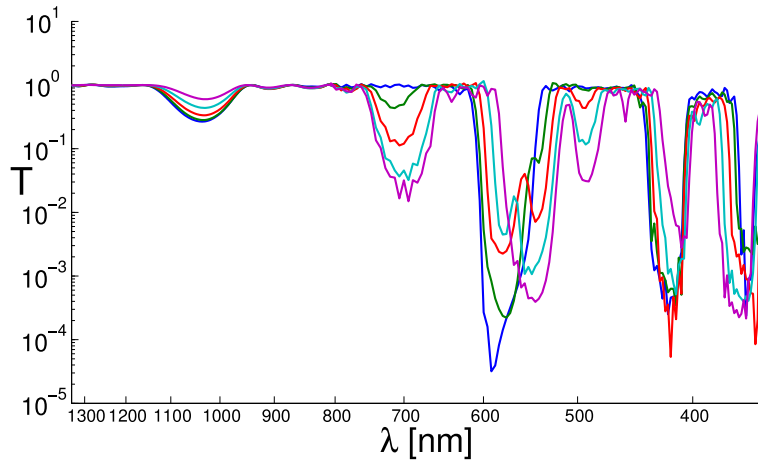


**Figure 6.10:** Change in transmission due to a lattice deformation in the propagation direction. The lattice is composed of ten rows of CNFs modelled here as dielectrics with  $\varepsilon = 10$  with a diameter of 50 nm and a lattice spacing of 500 nm. The curves correspond to a shift  $d$  as displayed in fig. 6.7(a) of: 0 nm (blue), 20 nm (green), 40 nm (red), 60 nm (light blue), 80 nm (magenta). The curve is plotted against vacuum wavelength instead of frequency to make the interpretation more clear.

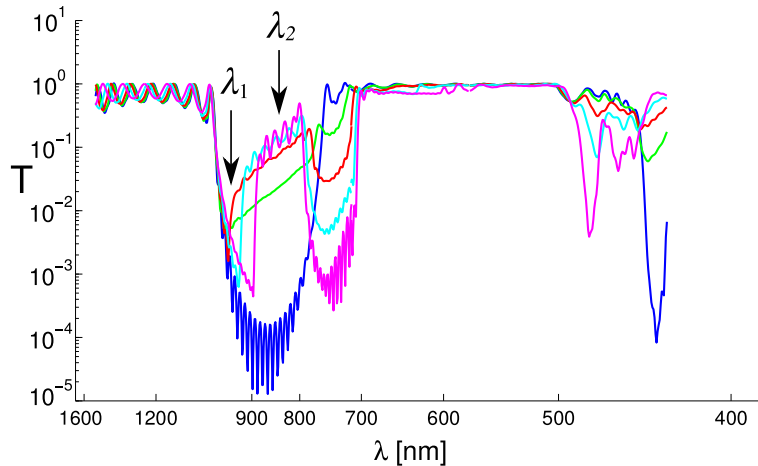


**Figure 6.11:** Change in transmission due to a lattice deformation perpendicular to the direction of propagation. The lattice is composed of ten rows of CNFs modelled here as perfect metals with a diameter of 50 nm and a lattice spacing of 500 nm. The curves correspond to a shift  $d$  as displayed in fig. 6.7 (a) of: 0 nm (blue), 20 nm (green), 40 nm (red), 60 nm (light blue), 80 nm (magenta). The curve is plotted against vacuum wavelength instead of frequency to make the interpretation more clear

longer wavelengths. Here the metal completely screens the field from propagating.

There are many similarities in the figures 6.9–6.11 and some differences. The drop that appears in the longitudinal case for both metallic and dielectric systems around 600 and 700 nm is not present in the transverse case. This indicates that the drop is related to the opening of a bandgap in the frequency spectrum due to a changed Brillouin zone, similar to what happened in the one-dimensional case. The gap in the dielectric system is located at a wavelength that correspond to where the second gap is located ( $\omega \simeq 0.75$ ),

and the lack of this opening in the transverse case strengthens the hypothesis that this is actually a bandgap that opens when the unit cell of the system is changed. The drop in transmission around 1050 nm in the dielectric and 900 nm in the metallic system is present in all systems. It is located at a wavelength that indicates that it should be the first gap in the undisturbed system. In the one-dimensional case this gap was very large, but in two dimensions it only shows as a small effect in the dielectric case. In the metallic systems however, the gap causes a drop of two orders of magnitude in the transmission.

The transverse displacement results are shown in figure 6.11. The first thing to note is that the bandgap that opens in the longitudinal direction around  $\lambda = 650$  nm does not open at all in the transverse case. In the transverse case the Brillouin zone does not change in the  $x$ -direction, wherefore it is not expected that a new stop band appears here. There is a complicated feature in the transmission for  $\lambda = 700 - 1000$  nm. There are very sharp edges and the drop in transmission splits into two when the lattice is deformed. The sharp edges that move a little with this shift are interesting features to use in applications with e.g. tunable filters.

To understand this unexpected behaviour, the transmission dependence on the thickness of the PC slab is investigated. In a bandgap the transmission drops exponentially with PC thickness, while a propagating mode in the PC is not affected by the thickness. In figure 6.12 transmission at wavelengths  $\lambda_1 \approx 950$  nm (a wavelength longer than where the peak in the gap appears, see fig. 6.11) and  $\lambda_2 \approx 830$  nm (a wavelength within the new peak, that is, a wavelength affected by the shift in the lattice, see fig. 6.11) in PC slab systems with  $d = 80$  nm is displayed against PC slab thickness. The plots are normalized to transmission 1 in systems consisting of 4 rows of CNFs for clarity. It can be seen that for  $\lambda_1$  the decrease in transmission is exponential, while  $\lambda_2$  is more or less not affected by the PC width.  $\lambda_2$  is thus not located in a band gap. These wavelengths are propagating undamped in the PC. The small constant decrease in transmission for frequencies around  $\lambda_2$  seen in figure 6.11 is instead due to coupling between the air mode and the mode in the PC.

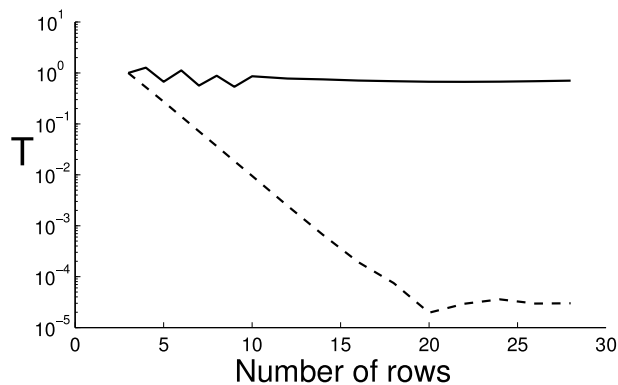


**Figure 6.12:** Transmission as a function of PC width in propagation direction in two dimensional simulation for wavelengths  $\lambda_1 \approx 950$  nm (a wavelength longer than where the peak in the gap appears, see fig. 6.11, dashed) and  $\lambda_2 \approx 830$  nm (a wavelength within the new peak, that is, a wavelength affected by the shift in the lattice, see fig. 6.11, solid) in PC slab systems with a perpendicular shift of  $d = 80$  nm. Transmission is normalized to 1 for a system of 4 CNFs. For a system of around 20 CNFs the transmission is down at the noise floor of the computation and does not decrease further with wider PCs.

In all cases it can be seen that higher frequencies are more sensitive to a lattice distortion in the same way as in the one-dimensional system. Many of the features can be addressed to changes in the band diagram. From an application point of view many features look very promising: sharp edges in some parts of the transmission that shift a little with shifted  $d$  and transmission that drops very much with a small shift are attractive features for filters and switches.

Coupling between modes in the PC and in vacuum is also important as mentioned above. To analyse this further one needs to go into group theory for the symmetries of the system, the modes in the PC and the plane waves which are used to excite the modes in the PC slab. This has not been investigated in this work but is discussed in Sakoda [14]. Also other boundary effects can play an important role in coupling between the PC modes and the vacuum modes. This is investigated e.g. by Vlasov [104].

### Three-dimensional case

So far only one- and two-dimensional systems have been discussed. The results look promising and the natural thing to do next is to consider the full three-dimensional nature of the problem by doing a full three dimensional-simulation. In this system the rods are of finite height and have to be standing on a substrate. The effects from the curvature of the CNFs as well as effects from the finite height (tip and fixed bottom) and the surroundings (substrate and lid) can be studied in these systems.

In three dimensions the computational burden increases significantly. Simulations were performed on a workstation PC with 4 GB of RAM which was the limiting factor. Therefore only a small system consisting of four rows of rods in the propagating direction and periodic boundary conditions in the transverse direction, see figure 6.13 was considered. With this system size one simulation takes roughly 24 h to complete.

In the  $z$ -direction light was partly confined by PECs. Because of the broken symmetry in the  $z$ -direction, true incident plane waves cannot be considered any more. The light source is instead a finite plane which extends all over the computational cell in the  $yz$ -plane. In the bottom there is a PEC simulating the substrate which extends all over the computational cell. In the top there is also a PEC, but this only extends distances  $s'_1 = s'_2 = a/2$  from the centres of the first and last CNTs in the PC. This is a model of a top lid to confine light in the system. Between the tip of the fibres and the lid there is an air gap. The fibers are set to a height  $H = 1 \mu\text{m}$  and the gap height between the CNF tip and the lid is 300 nm. In the far end the flux is recorded in the usual way to obtain a measure of the transmission. It is clear however that the transmission might be different at different heights. Therefore flux is recorded at a number of different heights,  $h_i = 100, 300, 500, 700, 900$  nm. The width of each flux-plane is such that they touch. That is, the first flux plane extends from  $z = 0$  to  $z = 200$  nm, the second from  $z = 200$  to  $z = 400$  nm and so on. This means that the flux at height  $h_i$  represents the average flux through a 200 nm thick slice centred at the height  $h_i$ . The simulation is terminated in the same way as in two dimensions: By PMLs in the  $x$ -direction and periodic boundary conditions in the  $y$ -direction.

In three dimensions it is important to incorporate the CNF deflection into the simulation. The CNF profile is given by equation (3.5). The constant  $F_0/2EI$  is chosen so that the tips of the CNFs are displaced a distance  $dx$  to compare to the two-dimensional

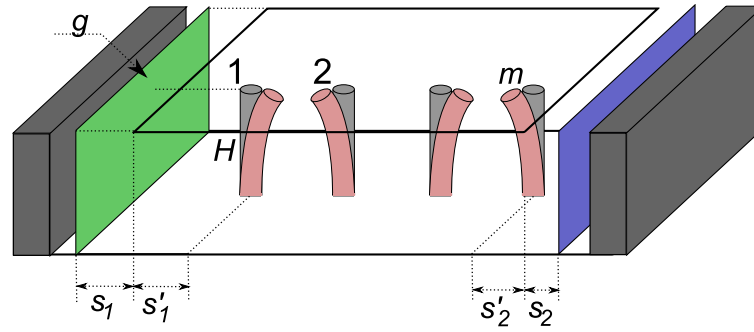


**Figure 6.13:** The setup in the three dimensional simulation,  $m = 4$ .

system. When the flux recording regions are placed  $0.5 \mu\text{m}$  away from the last CNF and at different heights,  $h_i$ , the results are as depicted in figure 6.14. As expected, the transmission closest to the substrate is not much affected by the bending. This is not surprising as the CNFs do not move here. At  $h_i = 500 \text{ nm}$  it can be seen that the system is quite sensitive to bending and transmission increases several times. Higher up transmission again is not very affected. This is also not surprising since we have an air gap there. It can further be noted that close to the substrate surface the transmission curves are quite smooth and show strong suppression at well defined frequencies. Even though the PC slab is only four fibres thick there is almost a difference of 100 times between the bottom of the stop band and the transmission bands. Close to the tip of the CNFs, however, the curves are irregular and the two stop bands are hardly resolvable at all. In the middle regions at  $300 \text{ nm}$  height the dip around  $\omega = 2.3$  is still resolved but it is not much affected by the bending of the fibres. The wider gap between  $\omega = 2.6$  and  $\omega = 2.8$  is, however, more strongly affected and we see the transmission go up. At  $500 \text{ nm}$  height the narrow stop band around  $\omega = 2.3$  is no longer detectable but the wide gap is still there and also quite strongly affected by the bending.

The results in figure 6.14 clearly indicate that it should be possible to detect a difference in transmission also in a three-dimensional system. The effects due to bending are sensitive to the detector height, a parameter that did not come in to play in the two dimensional system. It will probably also be the case that the curves smooth out the further away from the PC slab the detection is done as diffraction will equal out the difference at different heights.

In the simulations performed here a top lid is used to confine light to the substrate. This is not necessarily needed. For a small PC system like the one considered the diffractive effect of light might be small enough not to require  $z$ -confinement. The whole system is only approximately  $7 - 9$  wavelengths long, depending on where the start is considered. Computationally however, the lid is an improvement since an open system would require a much large computational cell and would hence not be possible on a workstation PC.

### Performance analysis

The performance of the device considered can be characterized by the voltage required to electrostatically bend the CNF and the speed limit with which this can be done. The required voltage for metallic nanowires can be estimated to be less than  $20 \text{ V}$  [105]. The tuning speed is limited by the resonance frequency of the CNF. It can be estimated e.g.

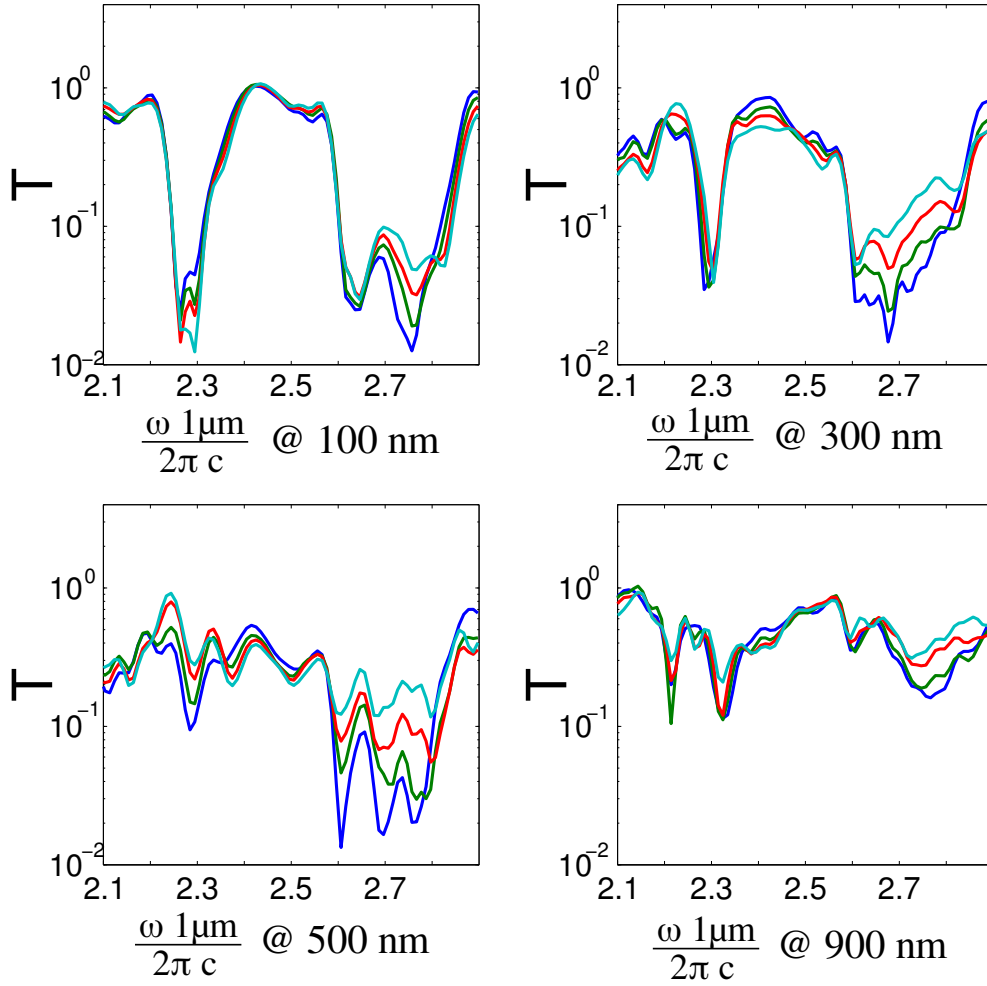


**Figure 6.14:** Results from a three dimensional simulation of four PEC CNFs for the flux recorded at different heights above the substrate (detector height denoted together with the  $x$ -axis label) and different bending of the CNFs. Blue is no bending, green 20, red 40, light blue 60 nm in the tip.

for carbon nanofibers via the cylinder cantilever model where

$$f = \frac{1}{\sqrt{2\pi}} \frac{r}{H^2} \sqrt{\frac{E}{\rho}},$$

where  $\rho$  is the density, which has been reported to be in the range  $0.015 - 1.8 \text{ g cm}^{-3}$  [57] and  $E$  is the Young's modulus. With the values used in the simulation, a Young's modulus of  $E = 300 \text{ GPa}$  and a density of  $1.8 \text{ g cm}^{-3}$  we obtain  $f \approx 73 \text{ MHz}$  as an upper bound on the frequency. The switching speed is determined by the Q factor of the CNF resonator. A too high Q-value makes the CNFs vibrate which is not desirable. This can be controlled electrically e.g. by a dissipating element that lowers a too high Q-value. Based on recent measurements [65] a switching time of  $[f/Q]^{-1} \approx 1 \text{ } \mu\text{s}$  can be estimated to be readily achievable.

For dielectric CNFs, the load  $P(x)$  arises from CNF polarization, and similar changes in geometry require larger applied voltages than in the case of metallic CNFs.

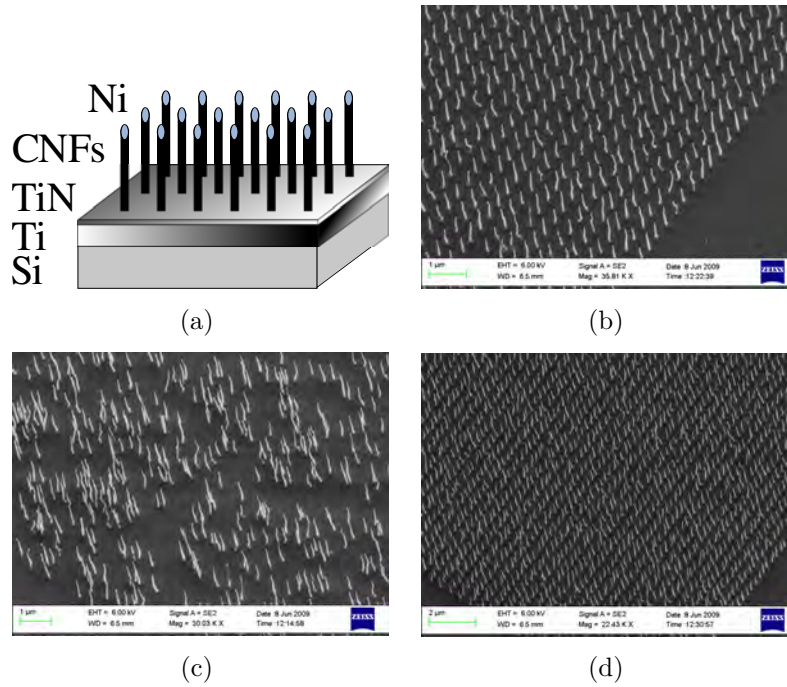


**Figure 6.15:** (a) sketch of the sample structure. (b) square lattice with lattice constant 500 nm (c) random sample of corresponding to 500 nm lattice constant CNF density. (d) rectangular lattice.

## 6.2 Paper II – Optical properties of carbon nanofiber photonic crystals

Papers' II and III main motivations were to provide us with a foundation on optical responses from the CNF-based PCs. Both the papers deal only with static structures. For the work in this paper, ellipsometry was used to characterize the structure. It turns out that ellipsometry can be used to probe, at least parts of, the band structure of the PC. There have been a few studies similar to this one previously published [106, 107].

CNF-PC samples with lattice constants of 300, 400 and 500 nm were fabricated using method A, described in the growth section. Both square and rectangular primitive cells were considered. Also structures with randomly placed CNFs with average densities corresponding to one of the periodic structures were fabricated as reference samples, see figure 6.15 for sample illustrations.

Ellipsometry measurements were carried out on the different lattices, varying the azimuthal angle. These measurements were performed by me and R. Magnusson in collaboration. This was done since we were interested to see if the anisotropy of the samples could be detected. The ellipsometer used was a dual-rotating-compensator ellipsometer from J A Woollam Co., Inc. This instrument is capable of measuring the full Muller matrix, but for the present study, only  $\Psi = \tan^{-1} |R_p/R_s|$  was considered.

Very strong response was indeed found which could be linked to the lattice structure of the PC. In the structured lattice case clear peaks appear that were not present for the irregular case. This is illustrated in figure 6.16. If looking e.g. at the large peak around 550 nm for the black line in figure 6.16(a) corresponding to the square PC,  $\Psi$  has a value

of approximately  $20^\circ$ , while the background is  $\Psi \sim 5^\circ$ . This corresponds to an increase of over 4 times in  $R_p$ . Panel (a) in figure 6.16 depicts the raw  $\Psi$ -data for both the pure TiN substrate, a random sample and a square lattice with lattice constant 500 nm for two different azimuthal angles. It can be noted that  $\Psi < 45^\circ$ , indicating that  $p$ -polarised light is reflected less than  $s$ -polarised. This is linked to the excitation of SPPs at the surface, which is much stronger for  $p$ -polarisation, see discussion in the next section. It

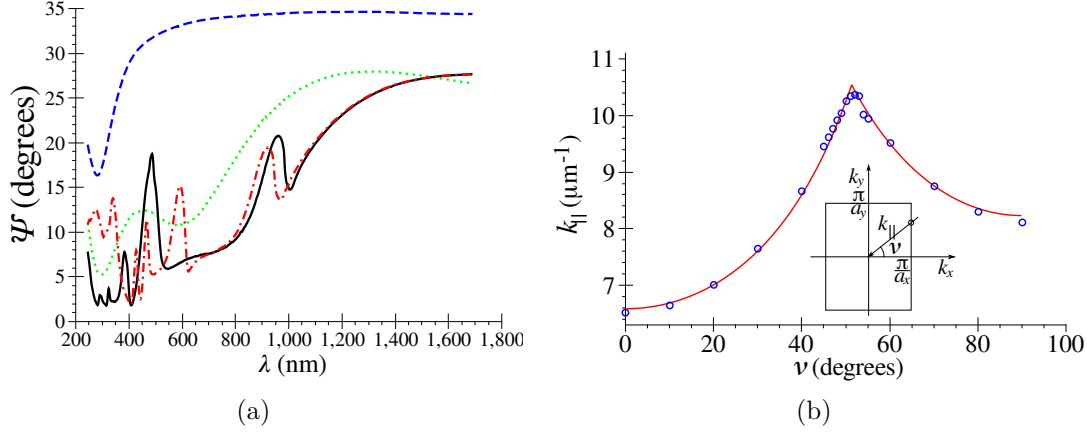


**Figure 6.16:** (a) Ellipsometry parameter  $\Psi$  for the TiN substrate (dashed), randomly placed CNFs (dotted) and for a PC with lattice constant 500 nm at  $0^\circ$  azimuthal angle (solid) and at  $15^\circ$  azimuthal angle (dash-dotted). (b) Wave vector of the lowest frequency peak of a rectangular sample as it is rotated from 0 to  $90^\circ$  azimuthal angle, circles. The solid line is the geometric construction of the distance from  $\Gamma$  to the BZ edge. The inset show the BZ of the rectangular sample and how the rotation  $\nu$  was performed.

can also be noted that these peaks move as the sample is rotated, illustrated by the  $15^\circ$  azimuthal rotation step in the graph. Also note that the low frequency peak moves down in frequency as the sample is rotated away from the symmetry direction while the next lowest does the opposite. In panel (b) of the same figure the longest wavelength peak position is recorded for a set of rotation angles of a rectangular lattice  $400 \times 500 \text{ nm}^2$ . The wavevector at the peak is  $\mathbf{k}^{\text{peak}} = 2\pi/\lambda_{\text{peak}}$ . The in-plane wavevector,  $\mathbf{k}_{||}$ , is the part of  $\mathbf{k}^{\text{peak}}$  parallel to the surface. For the data depicted in figure 6.16(a) the polar angle was set to  $\theta = 70^\circ$ , implying  $k_{||}^{\text{peak}}(\omega) = k^{\text{peak}}(\omega) \sin 70^\circ$ . If this peak is positioned at the BZ edge, when the azimuthal angle  $\nu$  is varied, we expect the peak position to shift according to

$$k_{||} = \begin{cases} \frac{k_{(10)}^{(0)}}{\cos \nu}, & \tan \nu \leq \frac{500 \text{ nm}}{400 \text{ nm}} \\ \frac{k_{(01)}^{(0)}}{\sin \nu}, & \tan \nu > \frac{500 \text{ nm}}{400 \text{ nm}}. \end{cases} \quad (6.16)$$

Here  $k_{(10)}^{(0)}$  is the wavevector of the first peak for a rotation angle  $\nu$  such that the specular beam in the ellipsometer is in the (1, 0)-direction (numbered by reciprocal lattice vectors). The parameter  $k_{(01)}^{(0)}$  is similarly obtained for a specular beam in the (0, 1) direction. From the geometry of the BZ it follows that

$$k_{(01)}^{(0)} = \frac{5}{4} k_{(10)}^{(0)}. \quad (6.17)$$

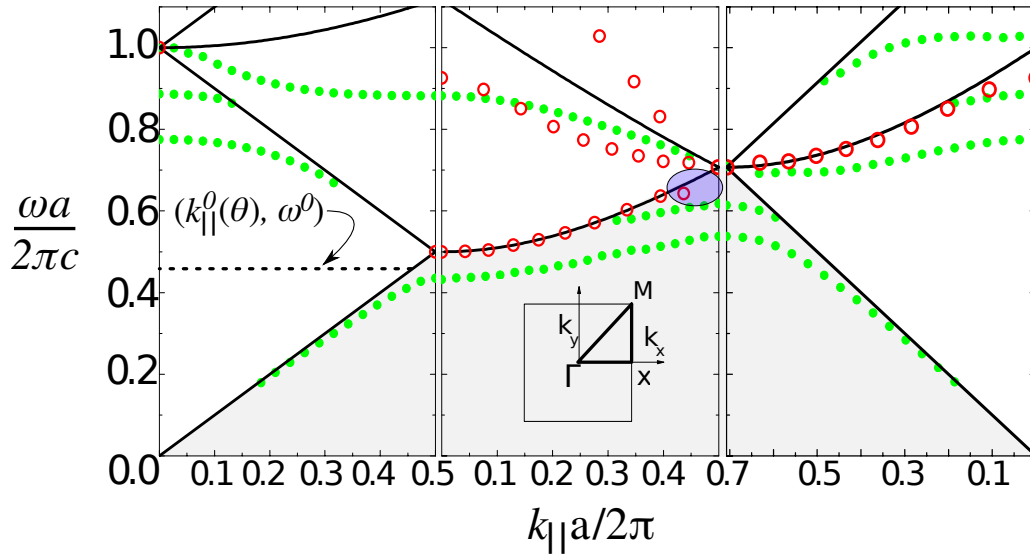


**Figure 6.17:** Band structure (solid green circles) of a 2D square PC consisting of dielectric pillars with radius of  $0.05a$  and a refractive index of 4.1, calculated using FDTD computations. The red circles mark peak maximum for different rotations. Solid black lines are light lines and the shaded region correspond to  $k_{PC}(\omega) > k_{vacuum}(\omega)$ , inaccessible for vacuum modes to excite. Inset shows the BZ of the square lattice with high symmetry points marked and the irreducible BZ highlighted.

The red solid line in panel (b) is the predicted peak position according to equation (6.16). Remarkably, the agreement between the peak position and this prediction is excellent. Hence it can be concluded that there is something happening at the BZ edge that make  $p$ -polarised light reflect more strongly at the edge. Computing  $k_{||}^{\text{peak}}$  we also see that  $k_{||}^{\text{peak}} = k_{||}$ .

The above discussion concerns only  $p$ -polarised light though the measured quantity is  $\Psi \sim \frac{r_p}{r_s}$ . This is motivated by the fact that a PC consisting of high-index dielectric pillars (here CNFs) embedded in a low index material (here air) affect  $p$ -polarised light much more than  $s$ -polarised [13].

One can ask what is special with the BZ edge? The answer is that the dispersion relation in the PC experiences the largest deviation from the vacuum dispersion at the BZ edge. As stated in the theory section, the group velocity is proportional to the dispersion relation derivative. Further, as also noted, the refractive index is related to the propagation speed. The refractive index discussed in the theory section concerns homogeneous materials, but here we define an effective refractive index,  $n_{eff}$ , related to propagation speed in the PC. Further the refractive index controls reflections, according to the Fresnel equations, and a large refractive index miss-match at an interface results in a large reflection.

If the arguments above are correct, one should expect peaks at frequencies where the PC band structure is flat. To test this hypothesis, the band structure of our CNF PC was computed using FDTD. This was done by our collaborators in London. The result of the computation is depicted in figure 6.17 where also ellipsometry peaks have been marked for the reduced zone. The results seem to verify our hypothesis.

It was initially believed, and also claimed in the paper, that we could probe the band

structure below the light line in a way similar to what was done by Paraire and co-workers [108]. However this was not a correct assumption, and the kind of analysis carried out by Paraire et *al.* was not performed. Peaks as described by Paraire et *al.* should appear at entirely different  $(\omega, k)$ -tuples, which was not addressed in this study. The peak encircled in figure 6.17 appearing below the light line was miss-placed due to a data-handling error and should be placed at the light line as expected.

The part of the wavevector parallel to the surface controls the coupling to the PC modes. Since  $k_{\parallel} = k \sin \theta$ , different parts of the band structure of a sample can be probed by varying the inclination angle while the energy (= frequency) is constant. That is, for a fixed  $\omega$  is it possible to get any  $k_{\parallel} < \omega/c_0 = k$ . This corresponds to the region above the light line and is illustrated in figure 6.17 by the dashed line spanning a set of  $k_{\parallel}^0$  for a fixed  $\omega^0$ . Below the light line,  $k_{\parallel}$  is larger than any  $k$  in vacuum, making this region in-accessible for these kind of vacuum coupling techniques.

### 6.3 Paper III – Diffraction from carbon nanofiber arrays

Paper III should be viewed as complementary to Paper II. The same static samples were investigated, but now diffracted beams were recorded instead of the specular one. Paper III presents investigations on diffraction from a square lattice of VACNFs with a lattice constant of  $a = 500$  nm. The measurement set-up described in section 5.1 was used to measure diffraction angles for several diffraction orders and inclination angles. See figure 6.18 (a) and (b) for a SEM micrograph of the sample and a sketch of the measured angles. A few results are depicted in figures 6.18 and 6.19, verifying equation (2.13).

It was expected that diffraction intensities would play an important role when looking at the tunable structures, and hence we were interested in measuring that already for the static structures. Results from measuring intensity variations in the diffracted beam as the inclination angle is varied are displayed in figure 6.20. To understand the intensity variations a simple interference model was developed based on the form factor of the scatterers in the lattice. Equation (2.14) expresses the form factor of the scatterer. A simple model where  $\varepsilon$  takes the form

$$\varepsilon(x, y, z) = \Theta(H - z)\Theta(z)\delta(x, y)$$

was used. Polarisation or frequency dependence in  $\varepsilon$  was not included, but the model was designed only with the particular geometry in mind.

The idea was that a photon enters the PC structure, scatters against the CNF and exits. In this process it accumulates a phase which depends on the optical distance travelled, denoted  $\Delta l$ . The outgoing beam intensity is then the result of interference between all outgoing waves which can be expressed as

$$I_{m,n} \sim \sum_k e^{i\Delta l_k} = \int_0^H dz (e^{i\Delta l_1} + e^{i\Delta l_2}).$$

The last equality comes from the fact that from equation (2.13), the sign on  $k'_z$  is not determined. Hence there are two diffracted beams, going in different directions in the  $z$ -dimension. Below the CNFs, however, is the substrate that will reflect the beam with

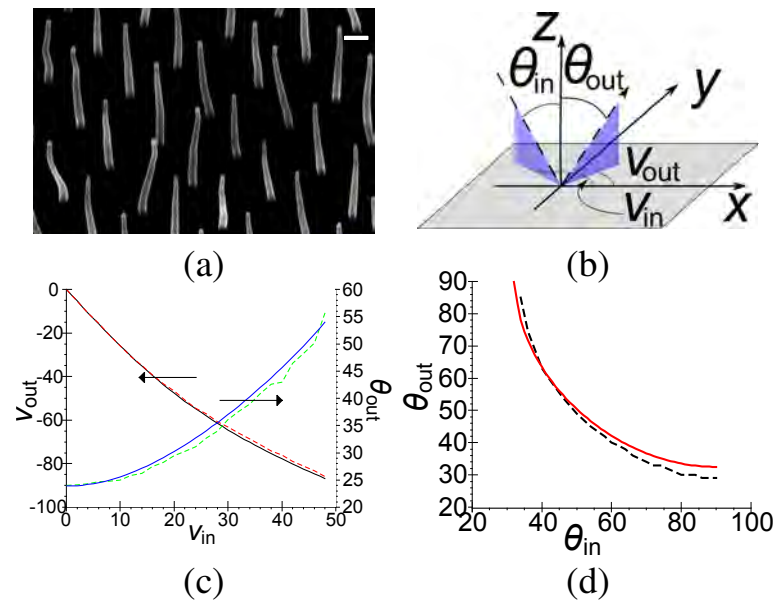


**Figure 6.18:** (a) SEM micrograph of a CNF lattice. Scale bar is 200 nm. (b) Definitions of the measured angles. The grey plane represents the sample surface and the dashed line the incoming and reflected light. The inclination angle,  $\Theta_{in}$ , and exiting angle,  $\Theta_{out}$ , are measured from the sample normal. Azimuthal angles,  $\nu_{in}$  and  $\nu_{out}$ , for the incident and diffracted light respectively, are measured from the x-axis. (c) Theoretical (solid) and experimental (dashed) relation between the diffracted and incident azimuthal angles for the  $(m, n) = (-1, 0)$  order and  $\Theta_{in} = 43^\circ$ . (d) Diffracted versus incident inclination angles obtained from theory (solid) and experiment (dashed) for  $(m, n) = (-1, -1)$  and  $\nu_{in} = 45^\circ$ .

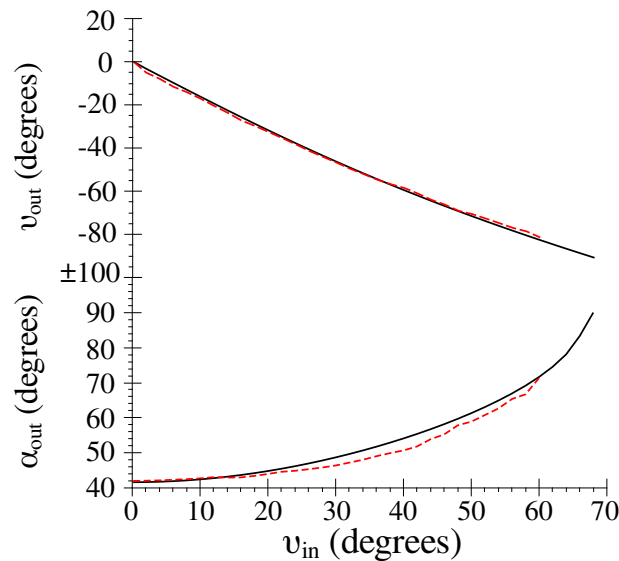


**Figure 6.19:** Diffraction angles (dashed measurement, solid theory) for the  $(-1, 0)$  order with fixed  $\Theta_{in} = 25^\circ$ .

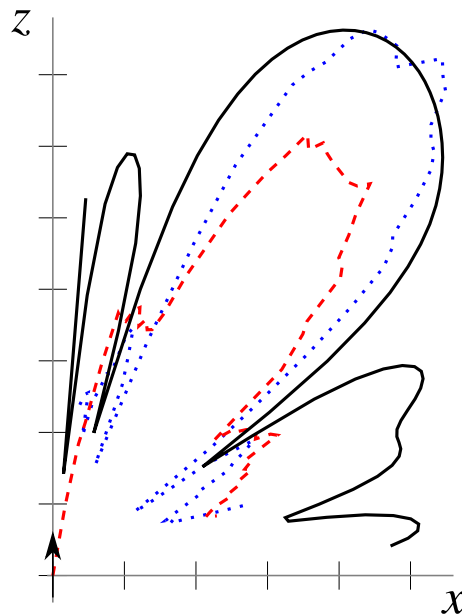


**Figure 6.20:** Diffracted beam intensity as a function of inclination angle for the backscattering order  $(-1,0)$  keeping  $\nu_{\text{in}} \equiv 0$  and varying polar inclination angle,  $\theta$ . Dashed correspond to  $p$ -polarisation, dotted to  $s$ -polarisation and solid to theory. Scale is arbitrary logarithmic.

a negative  $k'_z$ . Since  $k'_x$  and  $k'_y$  are the same in both cases, the two beams propagate in the same direction, causing them to interfere. The situation is illustrated in figure 6.21 for a situation where also CNF actuation is taken into account which is discussed more in-depth in connection to Paper IV.

The distances  $\Delta l_1$  and  $\Delta l_2$  are determined from points such that the phase of incoming and outgoing light relative to each other does not vary. This is illustrated by the dashed and dotted lines in figure 6.21. The distances can be computed by some geometric constructions. The predicted intensity variations are plotted together with the measurements in figure 6.20. The only free parameter in the model is the absolute intensity, which has been set so that maxima agree in the plot. The model seems to capture the intensity variations very well, but does not include any polarisation dependence. To see if the polarisation dependence can be understood the system was modelled using FDTD. This was done by our collaborators in London. The near field is plotted in figure 6.22 for the two polarisations. As can be seen, the intensity is much higher for  $p$ -polarised light. This is because the CNFs make it possible for the incoming  $p$ -polarised light to excite SPPs on the TiN surface. The SPPs are hybridised with a PC-type mode which makes them extend all over the CNF height as can be seen in the figure.  $s$  polarised light can not excite SPPs to the same extent and hence, does not experience the same damping as the  $p$ -polarised mode does.

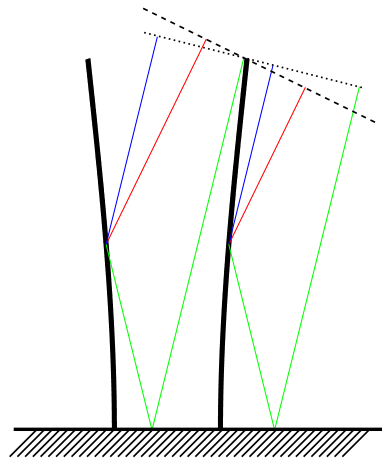


**Figure 6.21:** Sketch illustrating the optical distances travelled for the four different cases of scattered waves in the diffraction set-up with actuated CNFs for diffraction order  $(-1,0)$ . Thick solid black denotes the actuated CNFs, dashed and dotted black lines are help-lines. Solid red lines are incoming light, blue and green are directly scattered light and scattered light reflected in the substrate respectively.

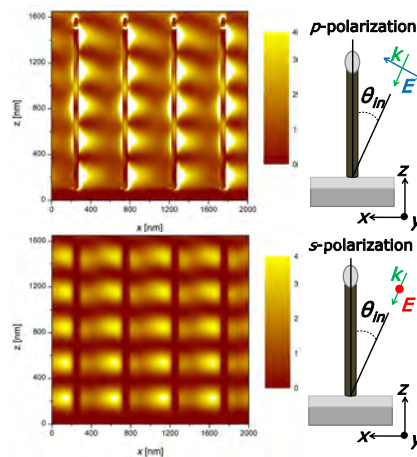


**Figure 6.22:** Near field maps within the plane of incidence ( $\Theta_{in} = 30^\circ$ ) corresponding to the  $(-1, 0)$  diffraction order for incident  $p$  (upper panel) and  $s$  (lower panel) polarisation (see right schematic pictures). Both panels consist of four PC unit cells and show the electric field intensity in linear scale.

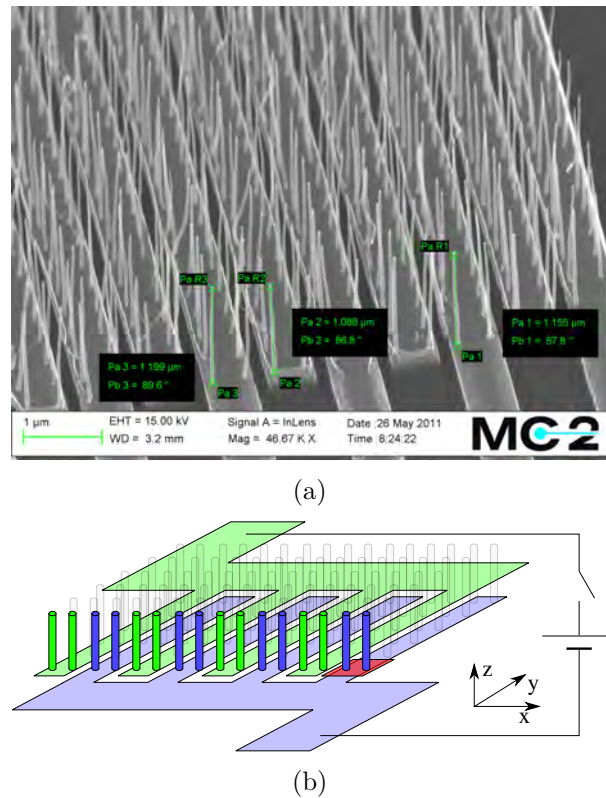


**Figure 6.23:** (a) SEM micrograph of a tunable CNF sample. The image depicts a corner of the sample which in total measures some  $1 \times 1 \text{ mm}^2$ . (b) Sketch of the tunable system. All but the first row of CNFs are shaded for clarity. The shaded rectangle in the lower right corner denotes the BZ.

## 6.4 Paper IV – Carbon Nanofiber Tunable Photonic Crystal

The last paper included in the thesis describes measurements on tunable samples. The same type of measurements as carried out in the work reported in papers II and III were performed also on tunable samples. In this way the results obtained in earlier work can be used as a foundation for understanding some of the results obtained here.

Samples, as depicted in figure 6.23(a), were fabricated using the process B described in chapter 4 and in the appendix. The distance between adjacent VACNFs was 400 nm. This distance was selected to increase the electrostatic coupling (compared to the 500 nm lattice constant mostly used in the previous works) between the CNFs while still keeping the distance large enough for feasible fabrication as well as staying within the visible part of the spectrum. We wanted to use the same diffraction set-up as in Paper III with the green HeNe (543.5 nm) laser. A smaller lattice constant could be interesting in future applications, providing a higher filling fraction (of CNFs), and hence increase the effect in the PC.

A voltage difference over adjacent meanders was applied in order to make each second pair of VACNFs repel and each second pair attract each other. The actuation profile of a bent VACNF is known from previous work, and presented in equation (3.5). Considering

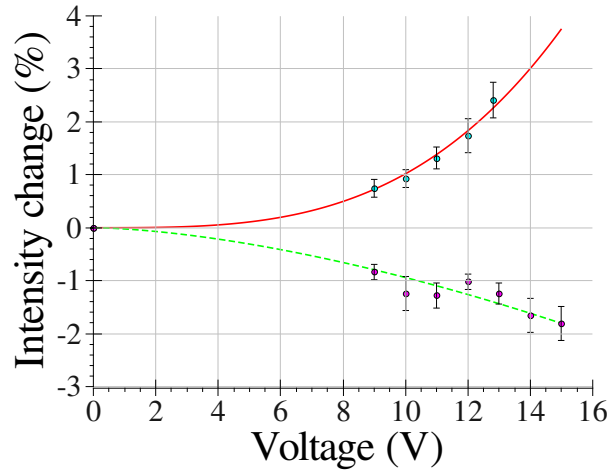


**Figure 6.24:** The relative intensity change for  $p$ -polarisation (solid) and  $s$ -polarisation (dashed) when applying voltage pulses and measuring the intensity in the  $(0,-1)$  diffraction order. Curves are fits of the function  $I_{p|s}(V) = \alpha_{p|s}(V/1V)^{\beta_{p|s}}$  to the data points. Error bars are sample standard deviation.

small deflections, which is expected here for the applied voltage range, the actuation profile can be approximated as the VACNFs being tilted an angle  $\varphi$  around their base. This is depicted in figure 3.1.

The ellipsometry and diffraction measurements were performed in the same manner as was reported in Papers II and III. In a static square PC however, there is a  $C_4$  degeneracy coming from the  $90^\circ$ -rotation symmetry. Due to the meanders, the tunable system as a whole does not possess this symmetry, but it is changed to  $C_2$  symmetry.

In the diffraction experiment, the meanders can also take part in the diffraction. But not necessarily it depends on which diffraction order is considered. If the directions are defined as in figure 6.23(b), diffraction which includes the reciprocal lattice vector  $\hat{b}_1$  includes effects from the meanders. To avoid that the electrodes take part, the order  $(m, n) = (0, -1)$  is selected for investigation in the diffraction measurement. Consequently (see figure 6.23(b)), the VACNFs are actuated perpendicularly, in the azimuthal angle, to the light propagation. This further implies that the periodicity, as experienced by diffracted photons, does not change when a voltage is applied. The lattice constant is  $a_{\text{CNF}} = 400$  nm, independently of voltage since light is diffracted in the  $x$ -direction. This is to be compared with the diffraction orders with  $m \neq 0$ , which experience that the lattice constant of the VACNF lattice doubles in the  $x$ -direction when the VACNFs gets actuated. However, the full lattice (VACNFs + meanders) always has a lattice constant  $a_{\text{full}} = 800$  nm, independently of voltage, since the meanders have a lattice constant of  $a_{\text{meanders}} = 800$  nm.

In total, from the discussion in the previous paragraph, the perpendicular actuation used in the diffraction experiment amounts to a change in the structure of the unit cell of the lattice, when seen by the  $(0, -1)$  order.

Results from applying voltage pulses of 2 s on followed by 2 s off and measuring the normalised average intensity change for each polarisation  $\overline{\delta I}_{p|s} = \frac{1}{N} \sum_{i=1}^N \delta I_{p|s,i}$ , with  $N = 10$  and  $\delta I_{p|s}(V) = \frac{I_{p|s}(0) - I_{p|s}(V)}{I(0)_{p|s}}$ , in the diffracted beam is depicted in figure 6.24. The

error bars denote sample standard deviation  $s_{p|s} = \sqrt{\frac{1}{N-1} \sum_{i=1}^N (\delta I_{p|s,i} - \overline{\delta I_{p|s}})^2}$ .

As can be seen, the intensity increases for  $p$ -polarisation and decreases for  $s$ -polarisation. This is expected as, when applying a voltage, the VACNFs effectively get tilted and thus change their alignment with respect to the light polarisation. With no voltage applied, the CNFs are aligned with  $p$ -polarised light (actually the CNFs lie in the incidence plane, but are not aligned with the  $p$ -polarisation. The angle between the E-field of  $p$ -polarised light and the VACNFs correspond to the incidence angle.). The intensity of the diffracted  $p$ -polarised beam is lower than the  $s$ -polarised beam. When the voltage is applied, the alignment changes from being completely aligned with the  $p$ -polarisation to being partially aligned with the  $s$ -polarisation. The diffraction intensity changes accordingly.

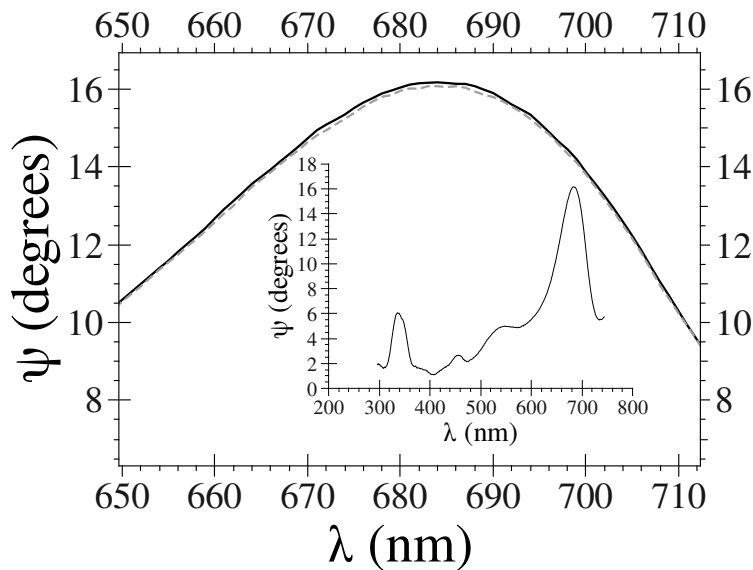


**Figure 6.25:** Difference in ellipsometric parameter  $\Psi$  for 0 V (solid) and 17 V (dashed) as a function of wavelength. The inset depicts the whole spectrum recorded in the ellipsometer for no applied voltage.

The ellipsometry measurements were performed in the direction where the CNFs are deflected in the specular direction. This was selected to make comparison to earlier results easier. The ellipsometry measurements are not as sensitive as the diffraction measurements, but still, actuation can be detected. This is illustrated in figure 6.25. It should be noted that there is only a difference in  $\Psi$  at the peaks of the ellipsometry measurements. The peaks in turn appear at the band edges and we address the sensitivity at the band edges to the divergence of the effective refractive index. In the theoretical computations in Paper I, we saw much larger effects from actuation. It is however expected to be much smaller here since the interaction volume of the light is much smaller. Light enters, reflects at the surface and exits within only a few wavelengths, while in Paper I, the light was confined to propagate in the PC plane.

### Voltage drop over meanders

To achieve uniform actuation in a tunable PC it is important to have a uniform voltage drop over the whole electrode. To verify this, the electrodes were modelled using infinites-

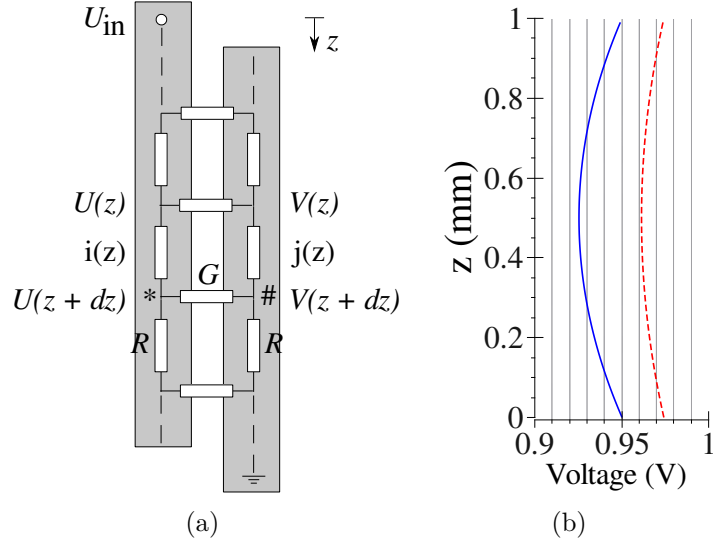


**Figure 6.26:** (a) Resistor model of the electrodes in the tunable PC structure.  $R$  denotes line resistivity in an electrode,  $G$  denotes line conductivity between electrodes (leakage). (b) Voltage drop between electrodes for the parameters found in the sample (dashed) for model with only two electrodes and (solid) for model with many electrodes.

imal resistance elements in an analysis inspired by the derivation of the transmission-line equation [60]. Two sections of the electrode meander were modelled as a resistor net as in figure 6.26(a).  $Rdz$  is the differential resistance in an infinitely short meander segment, while  $Gdz$  is the differential conductivity of an infinitely short segment of the gap between the sections. The voltage in the left and right section respectively is denoted  $U(z)$  and  $V(z)$ . Corresponding currents are  $i(z)$  and  $j(z)$ . The boundary conditions in the system are

$$\begin{aligned} U(0) &= U_{in}, & V(L) &= 0 \\ i(L) &= 0, & j(0) &= 0. \end{aligned} \quad (6.18)$$

Nodal analysis and Ohm's law yields that the voltage between the sections (that is, voltage over  $G$ ) as a function of  $z$  is given by

$$u(z) = U(z) - V(z) = Ae^{kz} + Be^{-kz}, \quad (6.19)$$

with  $k = \sqrt{2RG}$ . The coefficients  $A$  and  $B$  are found from the boundary conditions, equation (6.18). The solution for values of  $R$ ,  $G$  and  $L$  from the samples and 1 V applied, is plotted in figure 6.26(b).

The voltage drop is not constant, but the difference between the maximum voltage drop and the minimum is small (difference of 3-4 % for the full model, see below). Even if the force felt by the CNFs depends on the voltage to some higher power, this difference is very small, indicating that the CNF bending uniformity due to the voltage difference affects operation less than the overall sample quality.

It should further be noted that the model here only takes into account two electrode sections, while in the true structure there are several sections, as in figure 6.27. This can be accounted for by  $G \rightarrow 2G$ , which is valid as long as  $G$  is small. The resulting voltage distribution is found in figure 6.26(b) as a solid line. Note that the voltage-drop difference

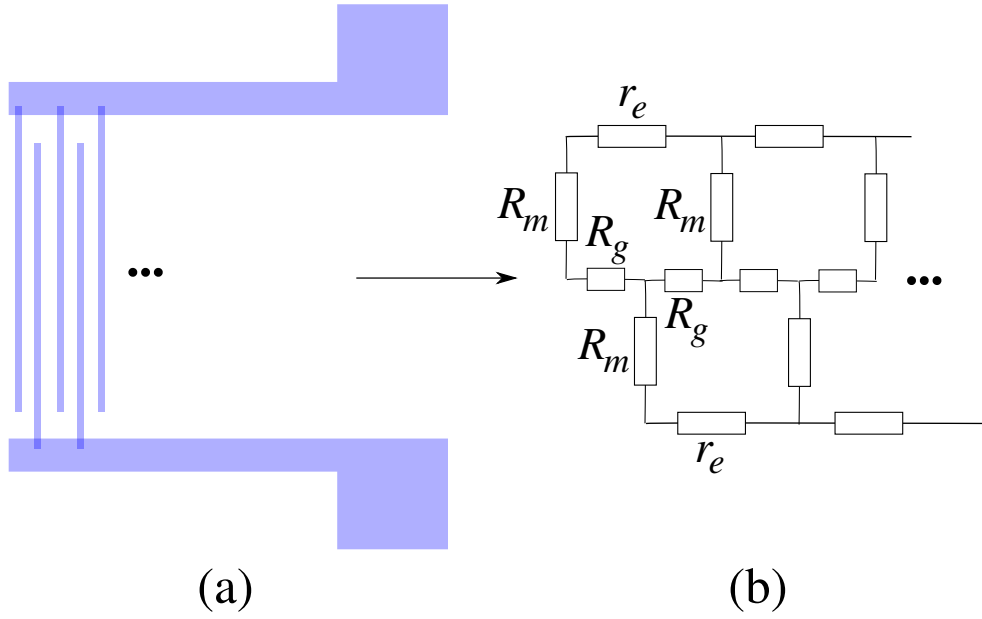


**Figure 6.27:** The geometry of electrodes (a) in the tunable PC and (b) the corresponding resistance net model.

between the edges and the middle is slightly larger for the many-sections model, but that the largest effect is an overall decrease in the voltage-drop.

With this at hand, a simplified resistance net model of the meander structure was made to get the value of  $G$ . Surface resistivity is defined as

$$\rho_s = \frac{U/l}{I/d},$$

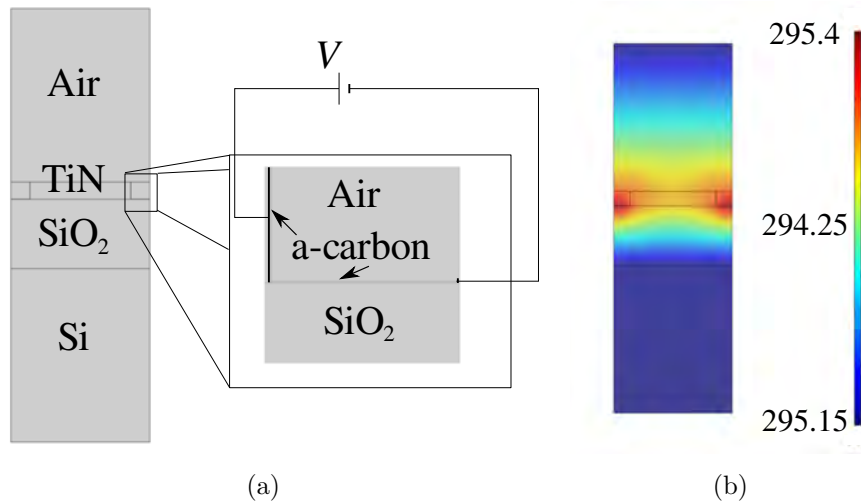
where  $U$  denotes the voltage drop over a length  $l$  and  $I$  is the current in a film of width  $d$ . Surface resistivity as measured using a 4-probe surface resistivity measuring unit for the TiN deposited in this work has a surface resistivity of  $\rho_s = 0.8 - 0.9 \Omega/\text{sq}$ .

Figure 6.27(a) depicts the electrode net underlying the CNFs that form the PC. The resistivity in the conductor connecting the contacting pad and the PC electrodes is denoted  $r_e$ , and is much smaller than any other resistance in the system, and can be ignored.

The total resistance,  $R$ , between the two pads is measured, and is usually found to be between 1 and 10  $\text{k}\Omega$  before CNF growth. After growth this value changes to  $\sim 100 \Omega$ . Using the lumped model depicted in figure 6.27(b) and assuming periodic boundary conditions (that is, there is an  $R_g$  connecting the first and last section as well), the net can be approximated as  $2N$  resistors  $2R_m + R_g + 2R_m$ , where  $N$  denotes the number of electrode pairs, in parallel. This results in an equation for the gap resistor

$$R_g = 2NR - 4R_m,$$

The gap resistance,  $R_g$  is found to be in the range of 1  $\text{M}\Omega$  before growth. Further, by multiplying by  $a/l$ , where  $l$  denotes electrode length and  $a$  is the lattice constant, the resistance "felt" by a single CNF pair is around 1  $\text{G}\Omega$ . More importantly, it can be seen that  $R_g$  is the dominant resistance in the system, which guarantees that the voltage drop will be over the gap. This is the assumption used above in modelling the voltage drop along an electrode pair.



**Figure 6.28:** (a) Model of the sample for investigating joule heating. (b) Temperature distribution in the sample when 15 V is applied between the edges as depicted in (b).

## Heating

Possible effects from heating are thermal expansion and change of the refractive index. These are not desired here, and we want to make sure that we are not observing heating effects. During CNF growth, a thin layer of amorphous carbon deposits on the sample surface. This makes the conductance between electrodes much higher than on a sample that has not been grown on. Before growth, the resistance between the contact pads is  $10^3 - 10^4 \Omega$ , but after growth it is some  $150 \Omega$ . When applying 10 - 15 volts in the actuation experiment this amounts to an applied power  $P = U^2/R \approx 1 \text{ W}$ . The sample is  $1 \text{ mm}^2$  and a power density of  $1 \text{ Wmm}^{-2}$  is not high. To accurately account for any joule heating that might occur in the system however, we were interested to see what heating effect this power has on the sample.

A model, with parameters taken from the sample, was considered in COMSOL Multiphysics, see figure 6.28(a). The dimensions were taken from the sample (except Si and amorphous carbon thickness) and temperature boundary conditions were set to  $20^\circ\text{C}$  at the top and bottom. At the sides, boundary conditions were set to isolating, but could equally well have been set to periodic. The resistivity of the carbon layer was set to match the resistance in the sample, making the actual thickness of the layer less important. The geometry is depicted in figure 6.28(a). The carbon layer was placed on the SiO<sub>2</sub>-substrate and a voltage is applied over the layer, simulating the voltage in the sample.

When applying 15 V to the sample in the model, the maximum temperature increase was  $\sim 2^\circ\text{C}$ , indicating that no significant heating is taking place. This situation is depicted in figure 6.28(b).

The increase in temperature should be compared to the thermal expansion coefficient of the system which, for SiO<sub>2</sub>, is reported to vary between 0.5 to  $4.1 \text{ ppm } K^{-1}$  [109]. Thus a 2 degree temperature increase corresponds to a lattice coefficient deformation of  $\sim 8 \text{ ppm}$ . This effect is negligible under the present circumstances.

## Applying a too high voltage

The snap-in position of an electrostatically actuated rectangular beam is approximately  $1/3$  of the distance between the beams [110]. Which voltage this corresponds to is not easily determined. Hence it is easy to apply too high a voltage, resulting in permanent damage to the sample. This situation is depicted in figure 6.29 where 20 V was applied between the pads of one sample. From the figure it is clear that two things happen to the

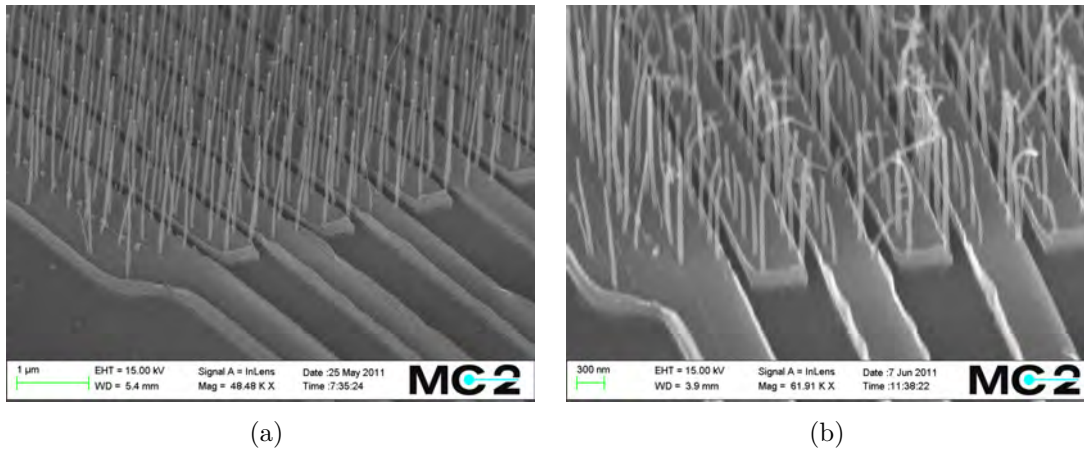


**Figure 6.29:** SEM micrograph of the same area of a sample before (a) and after (b) 20 V was applied between the pads.

VACNFs: First, A significant part of the VACNFs get burnt away and second, the VACNFs are plastically deformed, keeping part of the bent structure. The change in the VACNF structure is also reflected in the optical response, which is seen to drop significantly at the moment when a too high voltage is applied. From this, we decided to work below 20 V in the experiments.

# Chapter 7

## Conclusions and outlook

This final chapter covers a retrospective view of the work I have performed during my time as a PhD student, a look forward to possible extensions and some concluding remarks.

Future improvements can be divided into two categories: First there are concrete improvements that could have been implemented directly in connection to the work reported. Simply, things I should have done differently. Next there are improvements of more visionary character that would be very nice to implement, and that would maybe render new results suitable for publication.

### 7.1 Conclusions

Vertically aligned carbon nanofibers have been used as building blocks to fabricate static and tunable photonic crystals (VACNF-PCs) in two dimensions. We have shown that compact integrated VACNF-PC devices could be useful as optical components in future integrated communication systems. We have also successfully performed measurements on non-integrated devices to characterise the optical properties of the VACNF-PC devices to provide a foundation for future work.

Both ellipsometry and diffraction measurements can be used to characterise the kind of systems considered here. These tools are convenient from an experimental point of view since they do not require microscopical manipulation or light focusing.

The main obstacle for using VACNF in integrated systems lies in the CNF fabrication process where two problems are prominent: compatibility with other process standards such as CMOS and reproducibility. These two issues are entangled since reproducibility can be improved by modifications in the growth process. These modifications, however, deal with high temperatures and other harsh environment parameters which in turn affects compatibility. Both the issues might be possible to remedy by switching to a different nano-wire material which may offer easier integration and better known fabrication processes.

### 7.2 The work seen in retrospect

If I had the opportunity to change any central decision in the work that I have been describing in the previous chapters, it would be to make a more structured study of the growth process. The growth has been problematic and I did not realise that, instead

of keeping the aim at the PC device I had initially in mind, I should have focused on understanding the growth better. Maybe then, in structuring the growth process, some valuable new insights could have emerged.

Initially in this work I also spent much time on fabricating wave guides for coupling light into the PC in the  $xy$ -plane. This would have been very nice if it had worked out but, seen in retrospect, was the wrong end to start with. Trying to fabricate a device with both a wave guide and a VACNF PC was too complicated a task. Instead I should have started directly with making PCs for diffraction and ellipsometry as was started later.

## Improvements of the optical set-up

An improvement in the optical set-up for measuring diffraction described in chapter 5 is to replace the fiber-spectrometer intensity measurement construction with a CCD chip. If a CCD chip was mounted where the collector lens is mounted today, both small angle variations of the beam and intensity variations could be measured without any mechanical adjustment of the set-up. This would have made a more stable and a dynamic set-up.

If redesigning the set-up, I would also select regularly sized optical components instead of the miniaturisation components used. The miniaturisation components are nice and compact, but there is not as large a selection of components and some do not hold the level of quality one would wish.

It would also have been beneficial to have had a larger focus on mechanical stability of the optical set-up as it turned out to be very sensitive when working with the tunable PCs and the main source of noise.

An interesting parameter to measure in the diffraction set-up is the cross-polarisation. That is, consider a Jones matrix

$$J = \begin{bmatrix} C_p & C_{ps} \\ C_{sp} & C_s \end{bmatrix}.$$

The off-diagonal terms correspond to conversion between  $p$  and  $s$ -polarisation. With a polarisation filter on the detector arm for the exiting beam the off-diagonal elements could be measured. This is a very simple improvement that would have been nice to implement from the beginning. To make even more accurate measurements also quarter-wave retarders could have been introduced, opening up for measuring the full Jones matrix. Such a system set-up resembles an ellipsometer, but works with non-specular reflections.

## 7.3 An outlook

To go from a slab-type of structure which has been the main focus of this work and to really view the system as a photonic crystal, confinement in the  $z$ -dimension has to be achieved. There are a number of ways to do this. The most obvious one from a theoretical perspective was presented in paper I where a metallic lid was used to confine the light. This is however not the only way to achieve confinement, and in practice not a good option.

In a thesis project [111] we investigated the possibility to use a conventional dielectric waveguide to confine light. Then, by introducing holes in the wave guide and placing CNFs

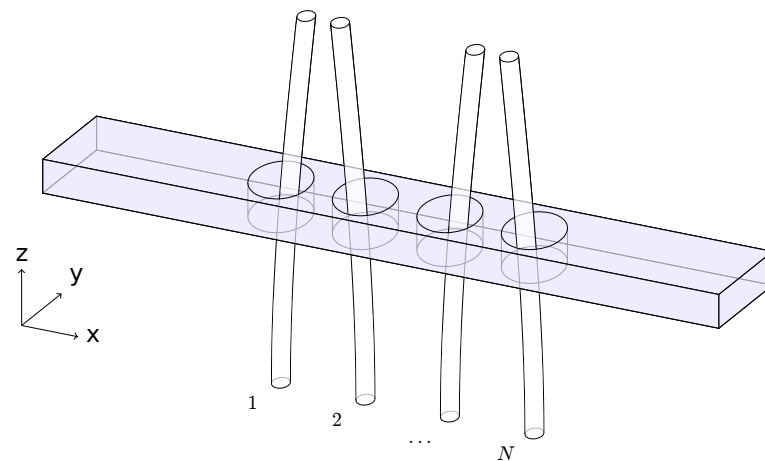


**Figure 7.1:** A sketch of a possible photonic crystal system consisting of a waveguide with holes and CNF piercing the holes. Reproduced from [111].

through the holes we were interested to see if electrostatic actuation of the CNFs could affect light transmission. The system is depicted in figure 7.1. Results are depicted in figure 7.2. As can be seen however, the system is only weakly tunable by this method.

The insensitivity in this system to the CNF position in the hole is due to how a waveguide works: Light is confined by a high refractive index material that guides light. The largest part of the light energy is hence present in the high index guiding material. Outside of the dielectric region there is an evanescent field extending out to the vacuum. Since the major part of the field energy exists inside the dielectric however, the modes are not very sensitive to disturbances outside of the dielectric.

We believe large tunability could instead be achieved by considering the "inverse" structure, depicted in figure 7.3. By applying a voltage, the distance between the dielectric slabs sitting in the tip of the CNFs will change due to the actuation of the CNFs. This structure would sacrifice speed for tunability since the high mass in the tip will for sure lower the resonance frequency significantly. However since now the high-refractive-index material is displaced we believe this design should provide for much better figures of merit. The approach introduced also opens up for many exciting designs where the dielectric can have any shape suitable for integration, *e.g.* a suspended planar PC of some kind with differently shaped displaceable tips.

In [112] an electrically pumped PC-based laser is reported. Lasing in PCs is based on creating a cavity in the PC with a certain resonance frequency depending on the cavity shape. Now this shape can be deformed in ways similar to what has been presented here, opening up for tunable nano-lasers.

Another more speculative application is motion sensors, where actuation is provided not by electrical means but by some mechanical motion. It can be a liquid flowing by the device, hence providing a liquid flow detector on the nano-scale for lab-on-chip devices. In these kind of devices, the geometry probably would look similar to what is depicted in figure 7.3 but with suitable modifications. It may be possible to displace the whole device, providing a vibration, rotation or acceleration sensor.

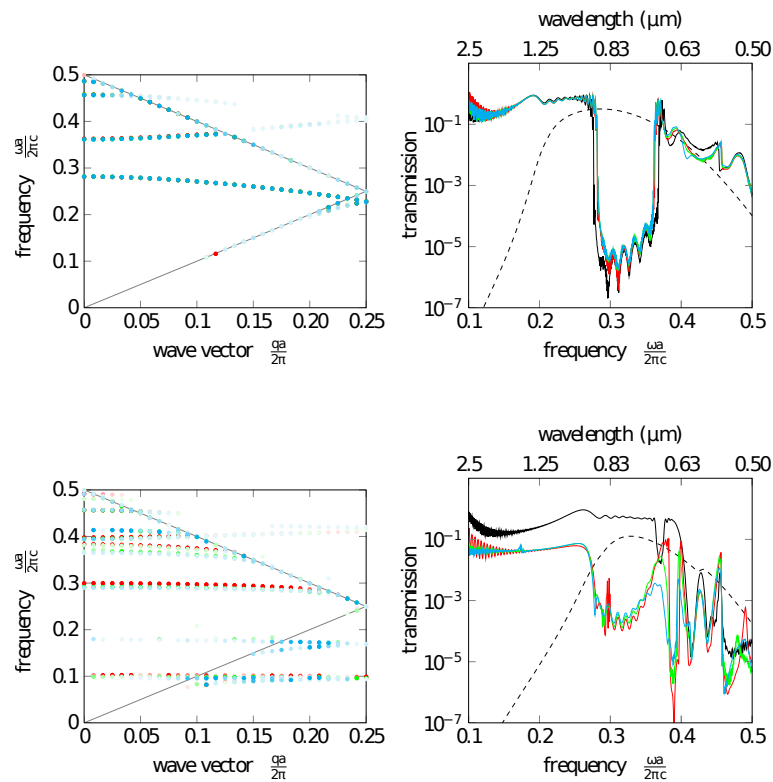


**Figure 7.2:** Results for the system depicted in figure 7.1. Left is the band structure of the infinite system. Right is transmission through the waveguide with 20 holes for different actuations, 0,  $0.05a$  and  $0.1a$ . The black curves correspond to the situation where no CNFs are available. Top figures correspond to the situation where the  $E$ -field has an even symmetry in the  $z$ -direction and an odd symmetry in the  $y$ -direction. Bottom is the opposite. Reproduced from [111].

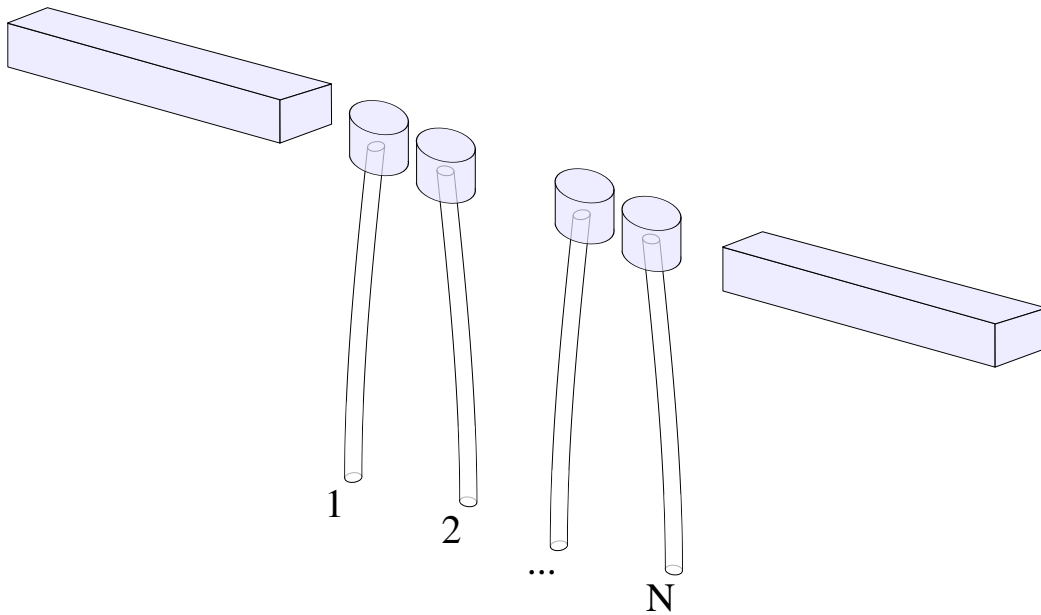


**Figure 7.3:** Improved tunable transmission wave guide structure. Blue indicate dielectric sitting on the tips of CNFs, acting as support for the dielectric slabs and used for electrostatic actuation.

# Acknowledgement

When you write your thesis, you at the same time sit and reflect back on the years spent as a PhD student. I realise that I come out as a very different person from when I started. There are so many things you learn and now it feels hard to imagine a life without these experiences.

There is a vast number of people guilty for this transformation. I want to start by thanking my supervisor and examiner, Jari and Eleanor. You gave me the opportunity to explore physics as a PhD student and you helped me in understanding many things in the process. Thank you! I should also give a thanks to Peter who engaged in my work and gave me good advises.

Next I would like to thank Yury. I am deeply thankful for having been given the opportunity to get to know you and your family. The other people in the CMT group, in particular Caroline, Gustav, Aurora: it's been a pleasure! In my other group, Eleanors group at GU, I'd like to thank Anton; it was great fun to teach with you! Erika, Anders, Sasa and Niklas: I have very much enjoyed your company!

I would also like to send a special thanks to Farzan. You've been a great friend and colleague! Then there is all the staff in the clean room who I should address a special thanks to - always giving valuable input on the work there. I also want to thank Andreas for the short but, for me, very instructive period we worked together. Further, I must also express my gratitude to Antonio. It has been a great pleasure collaborating with you. You have thought me a lot and been a good friend. My visit in London was a much enjoyable trip! Another very fruitful collaboration has been with Roger and Hans in Linköping. Thank you Roger for helping me with the ellipsometry measurements and Hans for always being very encouraging!

Of course, I also want to thank my parents and brothers for always supporting me. Also, during my time as a PhD student, our son Alvin came to us, filling my life with a joy not describable! Last, but not least, I want to express my very deepest love to you Anna. I am so very thankful that I get to spend my life with you!



# Appendix A

## Substrate processing

An exhaustive introduction to microfabrication can be found in the book by Campbell [113]. In the following section there will be some remarks about the particular process requirements associated with the substrate preparations for fabricating VACNF-based PCs.

Standard Si wafers were used as carrier substrates in the work where no particular requirements on electric isolation were required. On these substrates suitable materials, usually metals, were deposited to provide good growth conditions for VACNFs. This was the case for the work reported in Paper II and III.

For tunable systems a metal underlayer is also required for contacting the CNFs. In addition, for contacted systems the electrodes need to be isolated, and hence carrier substrates with 400 nm thermally grown oxide were used. This was the case for the work presented in Paper IV. The following sections are not meant as exhaustive descriptions of micro- and nano-fabrication, but rather point out a few details in connection to the CNF-based PC fabrication carried out in the project.

### Electron-beam lithography

Electron-beam lithography (EBL) was used in all the work for defining patterns. EBL has the advantage of being very flexible: A pattern can be redefined at every exposure. It is slow compared to optical lithography and other techniques. The resolution required in this work, with lattice constants down to 300 nm, however requires the use of EBL due to the limitations in the optical lithography equipment available in the lab. The EBL system used was a JEOL JBX-9300FS [114] set to 100 kV working voltage.

In EBL, electron scattering makes the beam very wide compared to the defined pattern dimensions. The beam contributes to the dose at points  $> 10 \mu\text{m}$  away from the defined point [115, 116]. This is known as the proximity effect and requires a proximity correction in certain cases. The Ni seed pattern was defined using MMA-MAA which in combination with the pattern type (low density) does not require proximity correction. For the electrode pattern in Paper IV, which was defined using UV5, the proximity effect has to be accounted for. This was done using a commercially available simulation software implementing the MonteCarlo method to compute the beam shape using the particular material stack as input data. The beam shape was then used together with the pattern, creating a dose compensation map which was fed to the EBL computer when exposing.

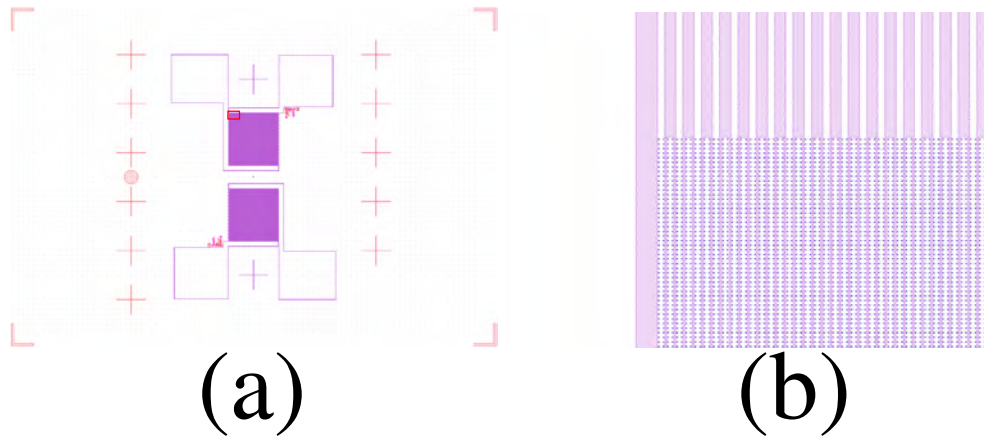


**Figure A.1:** The layout geometry used for the tunable system. In (a) the whole chip,  $10 \times 7 \text{ mm}^2$  is depicted. Red crosses are alignment marks. Purple is the layout inverse since a positive tone resist was used. The large squares outlined by purple are the contact pads and the area that looks solid purple is the PC. There are two samples (top, bottom) on each chip. To the right (left) on the top (bottom) sample there is a small region not quite distinguishable on the image. These are test structures used in fabrication. (b) is a close up of the region outlined by the red rectangle in (a). Blue dots mark Ni seed placement and purple marks inverted electrode structure.

The requirement to use proximity correction in the electrode pattern definition is due to the small dimensions in the pattern and the high pattern density together with the fact that the pattern is very large, causing proximity contributions from a large area, see figure A.1.

## Metal deposition

The two methods, lift-off and etching, used for depositing patterned metal layers are depicted schematically in figure A.2. Metals were either evaporated (Au, Ni, W, Mo) or sputtered using reactive sputtering (TiN). For patterns defined by lift-off, evaporation is required. This is because evaporation is performed at low pressure, causing high directivity of the metal vapour. For etching, any deposition method is valid and the one most appropriate for the application was used.

Lift-off is the technique of evaporating a material on an already patterned resist layer. Where there are holes in the resist, the metal deposits directly on the substrate, while where there is resist, the metal deposits on the resist, see figure A.2 left 5 and 6. After metal deposition, the resist is removed, lifting off the metal layer where it is not wanted.

For the lift-off steps, two-layer resist systems were developed and used. The bottom layers function was to form an undercut to improve lift-off release, see figure A.2. For Ni dots Zep and MMA-MAA copolymer [117] were used. These have a required exposure dose of approximately  $600 \text{ } \mu\text{C}/\text{cm}^2$  For defining alignment marks for the EBL, 100 nm gold was used. Such large structures were defined using UV5 and LOR [118]. UV5 requires a dose around  $22 \text{ } \mu\text{C}/\text{cm}^2$ . UV5 was selected for the etching processes used to define the TiN electrodes, due its good selectivity in that process.

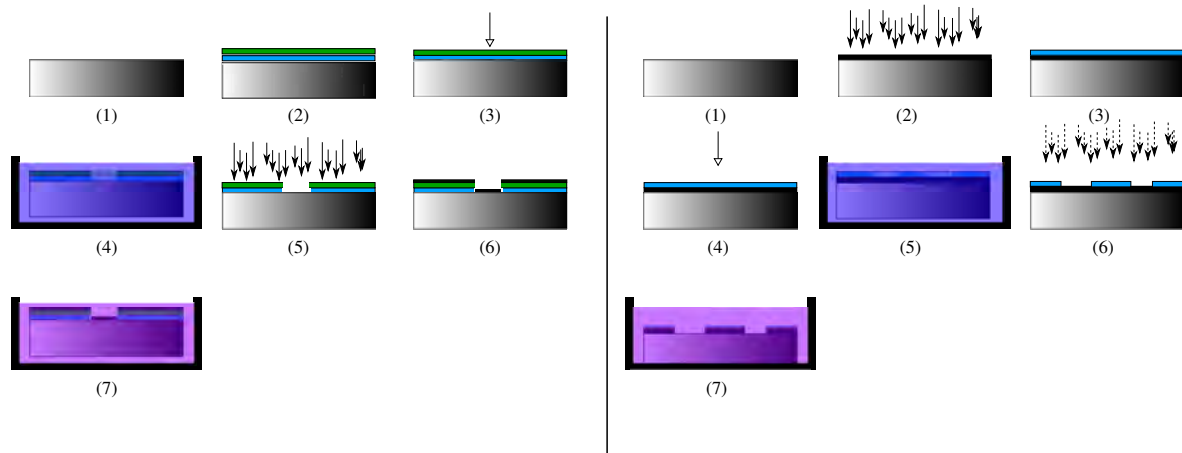


**Figure A.2:** Illustration of the different lithographic steps in depositing a metal layer using lift-off (left) and etching (right). The different steps in the lift-off process are: 1. empty substrate, 2. spin-coat resist, 3. expose pattern, 4. develop exposed pattern to remove parts of the resist, 5. evaporate metal layer, 6. the result after evaporation, 7. remove all resist using strong solvent. The different steps in the etch process are: 1. empty substrate, 2. deposit metal, 3. spin-coat resist, 4. expose pattern, 5. develop exposed pattern, 6. etch, 7. remove residual resist using strong solvent.

Parameter	Value
Cl <sub>2</sub> flow	50 SCCM
Ar flow	5 SCCM
Gas pressure	80 mtorr
Rf power	100 W
Inductive power	100 W
Temperature	R.T.

**Table A.1:** Parameters used for TiN etch. Rf power denotes capacitively coupled power to the plasma.

## Etching

To define electrodes for actuation, a one-step etch process was developed to etch TiN using an Oxford Instruments Oxford Plasmalab 100 [119]. There are several gases that can be used to etch TiN in a plasma system [120, 121, 122]. In the lab Cl<sub>2</sub> was available and selected for usage. The parameters selected for TiN etching are compiled in table A.1. It was seen that a patterned TiN substrate requires a much longer etching time compared to a TiN film. This is believed to be due to gas capture in the resist trenches which significantly increases the probability of re-deposition and reduced gas access to the TiN.

It should be noted that using the recipe found in table A.1, any gold structures, e.g. alignment marks, have to be protected since gold gets damaged by the etch process.

The etching speed is measured using a laser interferometer. The reflected laser intensity is measured and can be used to monitor the thickness of the etched layer. The resulting laser intensity when etching a Ti/TiN 70/20 nm dual stack is depicted in figure A.3. The three regions correspond to I, TiN etch, II, Ti etch and III, etching the underlying

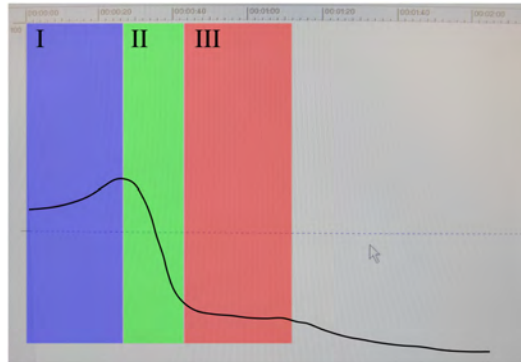


**Figure A.3:** Reflectivity profile when etching a stack of TiN on top of Ti.

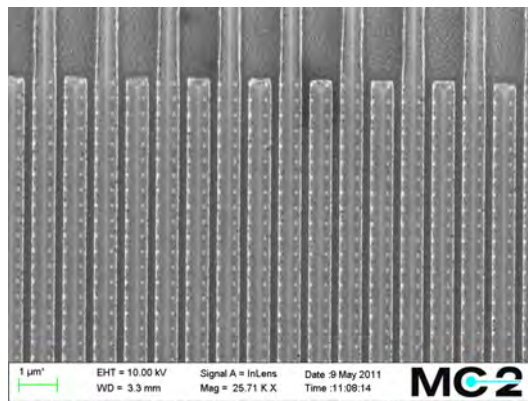


**Figure A.4:** Ni dots on meanders; the sample before growing VACNFs for the tunable CNF PCs.

substrate.

### Samples pre growth

A typical tunable sample before growth can be seen in figure A.4. The Ni dots can be seen as brighter spots close to the edges of each row and the rows are the electrode meanders. A careful look also reveals that the dots lie closer to the left side than the right. This is an alignment error between the two e-beam exposures and only occurs for the tunable samples where there are two e-beam exposures.

# Bibliography

- [1] Charles Kittel. *Introduction to Solid State Physics*. John Wiley and Sons, seventh edition, 1996.
- [2] E. Yablonovitch. Inhibited spontaneous emission in Solid-State physics and electronics. *Physical Review Letters*, **58** (20):2059–2062, 1987.
- [3] V. G Veselago. The electrodynamics of substances with simultaneously negative values of  $\epsilon$  and  $\mu$ . *Soviet Physics Uspekhi*, **10**:509–514, 1968.
- [4] A. Berrier, M. Mulot, M. Swillo, M. Qiu, L. Thylén, A. Talneau, and S. Anand. Negative refraction at infrared wavelengths in a Two-Dimensional photonic crystal. *Physical Review Letters*, **93** (7):073902, 2004.
- [5] R. Moussa, S. Foteinopoulou, Lei Zhang, G. Tuttle, K. Guven, E. Ozbay, and C. M. Soukoulis. Negative refraction and superlens behavior in a two-dimensional photonic crystal. *Physical Review B*, **71** (8):085106, 2005.
- [6] J. J. Baumberg, N. M. B. Perney, M. C. Netti, M. D. C. Charlton, M. Zoorob, and G. J. Parker. Visible-wavelength super-refraction in photonic crystal superprisms. *Applied Physics Letters*, **85**:354, 2004.
- [7] Bong-Shik Song, Susumu Noda, Takashi Asano, and Yoshihiro Akahane. Ultra-high-Q photonic double-heterostructure nanocavity. *Nature Materials*, **4** (3):207–210, 2005.
- [8] Marko Lončar, Dušan Nedeljković, Theodor Doll, Jelena Vučković, Axel Scherer, and Thomas P. Pearsall. Waveguiding in planar photonic crystals. *Applied Physics Letters*, **77**:1937, 2000.
- [9] K. C. Kwan, X. M. Tao, and G. D. Peng. Transition of lasing modes in disordered active photonic crystals. *Optics Letters*, **32** (18):2720–2722, 2007.
- [10] Michael Scharrer, Alexey Yamilov, Xiaohua Wu, Hui Cao, and Robert P. H. Chang. Ultraviolet lasing in high-order bands of three-dimensional ZnO photonic crystals. *Applied Physics Letters*, **88**:201103, 2006.
- [11] Wenyi Cao, Antonio Munoz, Peter Palffy-Muhoray, and Bahman Taheri. Lasing in a three-dimensional photonic crystal of the liquid crystal blue phase II. *Nature Materials*, **1** (2):111–113, 2002.

- [12] F. Riboli, P. Barthelemy, S. Vignolini, F. Intonti, A. De Rossi, S. Combrie, and D. S. Wiersma. Anderson localization of near-visible light in two dimensions. *Optics Letters*, **36** (2):127–129, 2011.
- [13] John D Joannopoulos, Steven G Johnson, Joshua N Winn, and Robert D Meade. *Photonic Crystals: Molding the Flow of Light (second edition)*. Princeton U.P., 2007.
- [14] K. Sakoda. *Optical properties of Photonic Crystals*. Springer, 2001.
- [15] K. Inoue and K. Ohtaka, (Eds.). *Photonic Crystals; Physics, Fabrication and Applications*. Springer, 2004.
- [16] L. Brillouin. *Wave Propagation in Periodic Structures*. Dover Publications, 1953.
- [17] Concita Sibilica, T. M. Benson, and Marian Marciniak., (Eds.). *Photonic crystals: physics and technology*. Springer, 2008.
- [18] Sajeev John. Strong localization of photons in certain disordered dielectric superlattices. *Physical Review Letters*, **58** (23):2486–2489, 1987.
- [19] J. W. S Rayleigh. On the remarkable phenomenon of crystalline reflexion described by prof. stokes. *Phil. Mag.*, **26**:256 65, 1888.
- [20] Thomas F. Krauss, Richard M. De La Rue, and Stuart Brand. Two-dimensional photonic-bandgap structures operating at near-infrared wavelengths. *Nature*, **383** (6602):699–702, 1996.
- [21] Gallium arsenide- NanoPiX- the nanostructuring platform. <http://nanophotonics.st-and.ac.uk/EPIX/GaAs.shtml> visited 2011-12-10.
- [22] K.M. Ho, C.T. Chan, C.M. Soukoulis, R. Biswas, and M. Sigalas. Photonic band gaps in three dimensions: New layer-by-layer periodic structures. *Solid State Communications*, **89** (5):413–416, 1994.
- [23] Ronold Wyeth Percival King, George J Fikioris, and Richard Bruce Mack. *Cylindrical Antennas and Arrays*. Cambridge Univ. Press, New York, 2. ed., rev. and enl. edition, 2002.
- [24] Ben A Munk. *Frequency Selective Surfaces: Theory and Design*. Wiley, New York, 2000.
- [25] Eugene Hecht. *Optics*. Addison-Wesley, Reading Mass., 2nd ed., repr. with corrections. edition, 1988.
- [26] D. Shechtman, I. Blech, D. Gratias, and J.W. Cahn. Metallic phase with long-range orientational order and no translational symmetry. *Physical Review Letters*, **53** (20):1951–3, 1984.
- [27] Michel Duneau and André Katz. Quasiperiodic patterns. *Physical Review Letters*, **54** (25):2688–2691, 1985.

- [28] Nobel win for crystal discovery.  
*BBC*, 2011.  
<http://www.bbc.co.uk/news/science-environment-15181187>  
visited 2011-12-10
- [29] Y. S Chan, C. T Chan, and Z. Y Liu. Photonic band gaps in two dimensional photonic quasicrystals. *Physical Review Letters*, **80**:956–959, 1998.
- [30] M. A. Kaliteevski, S. Brand, R. A. Abram, T. F. Krauss, R. DeLa Rue, and P. Millar. Two-dimensional penrose-tiled photonic quasicrystals: from diffraction pattern to band structure. *Nanotechnology*, **11** (4):274–280, 2000.
- [31] Tao Xu, Ning Zhu, Michelle Y.-C. Xu, Lech Wosinski, J. Stewart Aitchison, and H. E. Ruda. Pillar-array based optical sensor. *Optics Express*, **18** (6):5420–5425, 2010.
- [32] K. Asakawa and Y. Sugimoto. Photonic crystal-based integrated optics for advanced ultra-fast all-optical signal processing. *Integrated Optics: Theory and Applications Proc. SPIE - Int. Soc. Opt. Eng.*, **5956**:59560–1, 2005.
- [33] H. F. Jones. *Groups, representations and physics*. Institute of physics publishing, Bristol, second edition, 2003.
- [34] Sumio Iijima. Helical microtubules of graphitic carbon. *Nature*, **354**:56–58, 1991.
- [35] T. Koyama and M. T. Endo. Method for manufacturing carbon fibers by a vapor phase process, Japanese patent no. 1982-58, 966, 1983.
- [36] T. V. Hughes and C. R. Chambers, Manufacture of Carbon Filaments, US patent no. 405, 480, 1889.
- [37] L.V. Radushkevich and V.M. Lukyanovich. O strukture ugleroda, obrazujucesja pri termiceskom razlozenii okisi ugleroda na zeleznom kontakte (About the structure of carbon formed by thermal decomposition of carbon monoxide on iron substrate). *Zurn. Fisic. Chim.*, **26**:88–95, 1952.
- [38] Farzan A. Ghavanini, Maria Lopez-Damian, Damon Rafeian, Krister Svensson, Per Lundgren, and Peter Enoksson. Controlling the initial phase of PECVD growth of vertically aligned carbon nanofibers on TiN. *Sensors and Actuators A: Physical*, **172** (1):347–358, 2011.
- [39] Yucheng Lan, Yang Wang, and Z. F. Ren. Physics and applications of aligned carbon nanotubes. *Advances in Physics*, **60** (4):553–678, 2011.
- [40] K. Kempa, B. Kimball, J. Rybczynski, Z.P. Huang, P.F. Wu, D. Steeves, M. Sennett, M. Giersig, D.V.G.L.N. Rao, D.L. Carnahan, D.Z. Wang, J.Y. Lao, W.Z. Li, and Z.F. Ren. Photonic crystals based on periodic arrays of aligned carbon nanotubes. *Nano Letters*, **3** (1):13–18, 2003.

- [41] J. Rybczynski, K. Kempa, Y. Wang, Z. F. Ren, J. B. Carlson, B. R. Kimball, and G. Benham. Visible light diffraction studies on periodically aligned arrays of carbon nanotubes: Experimental and theoretical comparison. *Applied Physics Letters*, **88** (20):203122–3, 2006.
- [42] K. Kempa, J. Rybczynski, Z. Huang, K. Gregorczyk, A. Vidan, B. Kimball, J. Carlson, G. Benham, Y. Wang, A. Herczynski, and Z. F. Ren. Carbon nanotubes as optical antennae. *Advanced Materials*, **19** (3):421–426, 2007.
- [43] Y. Wang, K. Kempa, B. Kimball, J. B. Carlson, G. Benham, W. Z. Li, T. Kempa, J. Rybczynski, A. Herczynski, and Z. F. Ren. Receiving and transmitting light-like radio waves: Antenna effect in arrays of aligned carbon nanotubes. *Applied Physics Letters*, **85** (13):2607–2609, 2004.
- [44] Palash Bharadwaj, Bradley Deutsch, and Lukas Novotny. Optical antennas. *Advances in Optics and Photonics*, **1** (3):438–483, 2009.
- [45] Haider Butt, Qing Dai, Ranjith Rajesekharan, Timothy D. Wilkinson, and Gehan A. J. Amaratunga. Plasmonic band gaps and waveguide effects in carbon nanotube arrays based metamaterials. *ACS Nano*, **5**:9138–43, 2011.
- [46] Eleftherios Lidorikis and Andrea C. Ferrari. Photonics with multiwall carbon nanotube arrays. *ACS Nano*, **3** (5):1238–1248, 2009.
- [47] Chen-Yang Liu, Yen-Tun Peng, Jun-Zhi Wang, and Lien-Wen Chen. Creation of tunable bandgaps in a three-dimensional anisotropic photonic crystal modulated by a nematic liquid crystal. *Physica B: Condensed Matter*, **388** (1-2):124–129, 2007.
- [48] Qi Wu, Ethan Schonbrun, and Wounjhang Park. Tunable superlensing by a mechanically controlled photonic crystal. *Journal of the Optical Society of America B*, **23** (3):479–484, 2006.
- [49] S. Furumi, H. Fudouzi, and T. Sawada. Self-organized colloidal crystals for photonics and laser applications. *Laser & Photonics Reviews*, **4** (2):205–220, 2010.
- [50] S. Rajic, J.L. Corbeil, and P.G. Datskos. Feasibility of tunable MEMS photonic crystal devices. *Ultramicroscopy*, **97** (1-4):473–479, 2003.
- [51] Thomas Alkeskjold, Jesper Laegsgaard, Anders Bjarklev, David Hermann, Anawati Anawati, Jes Broeng, Jun Li, and Shin-Tson Wu. All-optical modulation in dye-doped nematic liquid crystal photonic bandgap fibers. *Optics Express*, **12** (24):5857–5871, 2004.
- [52] Tijmen G. Euser, Adriaan J. Molenaar, J. G. Fleming, Boris Gralak, Albert Polman, and Willem L. Vos. All-optical octave-broad ultrafast switching of Si woodpile photonic band gap crystals. *Physical Review B*, **77** (11):115214, 2008.
- [53] Ilya Fushman, Edo Waks, Dirk Englund, Nick Stoltz, Pierre Petroff, and Jelena Vučković. Ultrafast nonlinear optical tuning of photonic crystal cavities. *Applied Physics Letters*, **90**:091118, 2007.

- [54] Yurii A Vlasov, Martin O’Boyle, Hendrik F Hamann, and Sharee J McNab. Active control of slow light on a chip with photonic crystal waveguides. *Nature*, **438**:65–69, 2005.
- [55] K. -H Choi, Y. Cui, K. Liu, D. MacFarlane, and J. -B Lee. Ultra-compact electrothermally tunable photonic crystal prism for on-chip optical router application. *Solid-State Sensors, Actuators and Microsystems Conference (TRANSDUCERS), 2011 16th International*, pages 2558–2561, 2011.
- [56] J. E. Jang, S. N. Cha, Y. Choi, Gehan A. J. Amaratunga, D. J. Kang, D. G. Hasko, J. E. Jung, and J. M. Kim. Nanoelectromechanical switches with vertically aligned carbon nanotubes. *Applied Physics Letters*, **87** (16):163114, 2005.
- [57] Jae Eun Jang, Seung Nam Cha, Young Jin Choi, Dae Joon Kang, Tim P. Butler, David G. Hasko, Jae Eun Jung, Jong Min Kim, and Amaratunga Gehan A. J. Nanoscale memory cell based on a nanoelectromechanical switched capacitor. *Nature Nanotechnology*, **3** (1):26–30, 2008.
- [58] John David Jackson. *Classical Electrodynamics*. John Wiley and Sons, third edition, 1998.
- [59] Steven G Johnson. Notes on the algebraic structure of wave equations. <http://math.mit.edu/~stevenj/18.369/wave-equations.pdf> visited 2011-12-10
- [60] David Keun Cheng. *Fundamentals of Engineering Electromagnetics*. Addison-Wesley series in electrical engineering. Addison-Wesley, Reading, Mass, 1993.
- [61] Bahaa E. A. Saleh and Malvin Carl Teich. *Fundamentals of Photonics*. Wiley-Interscience, 2 edition, 2007.
- [62] Gaston Floquet. Sur les équations différentielles linéaires à coefficients périodiques. *Ann. École Norm. Sup.*, **12**:47–88, 1883.
- [63] Stefan A. Maier. *Plasmonics: Fundamentals And Applications*. Springer Verlag, New York, 2007.
- [64] Y. Zhang, E. Suhir, and Y. Xu. Effective young’s modulus of carbon nanofiber array. *Journal of Materials Research*, **21** (11):2948–54, 2006.
- [65] Anders Eriksson, SangWook Lee, Abdelrahim A. Sourab, Andreas Isacson, Risto Kaunisto, Jari M. Kinaret, and Eleanor E. B. Campbell. Direct transmission detection of tunable mechanical resonance in an individual carbon nanofiber relay. *Nano Letters*, **8** (4):1224–1228, 2008.
- [66] D. Gross. *Engineering mechanics*. Springer, 2011.
- [67] Tanil Ozkan, Mohammad Naraghi, and Ioannis Chasiotis. Mechanical properties of vapor grown carbon nanofibers. *Carbon*, **48** (1):239–244, 2010.

- [68] Chenyu Wei and Deepak Srivastava. Nanomechanics of carbon nanofibers: Structural and elastic properties. *Applied Physics Letters*, **85**:2208, 2004.
- [69] Edward D Palik, editor. *Handbook of optical constants of solids [electronic resource]*. Academic Press, 1998.
- [70] Vl. A Margulis and E. A Gaiduk. Dielectric function of single-wall carbon nanotubes. *Chemical Physics Letters*, **341**:16 22, 2001.
- [71] Francis Léonard and J. Tersoff. Dielectric response of semiconducting carbon nanotubes. *Applied Physics Letters*, **81**:4835, 2002.
- [72] P. Yeh, A. Yariv, and Hong. Electromagnetic propagation in periodic stratified media. i. general theory. *Journal of the Optical Society of America*, **67**:423–38, 1977.
- [73] Pochi Yeh. *Optical Waves in Layered Media*. John Wiley and Sons, 1988.
- [74] Ardavan F. Oskooi, David Roundy, Mihai Ibanescu, Peter Bermel, J.D. Joannopoulos, and Steven G. Johnson. Meep: A flexible free-software package for electromagnetic simulations by the FDTD method. *Computer Physics Communications*, **181**(3):687–702, 2010.
- [75] Lumerical solutions, inc.  
<http://www.lumerical.com/>  
visited 2011-12-10
- [76] Allen Taflove and Susan C Hagness. *Computational Electrodynamics, The finite-difference time-domain method*. Artech House, Boston, 2000.
- [77] Anders Bondeson, Thomas Rylander, and Pär Ingelström. *Computational Electromagnetics*. Springer-Verlag New York Inc., 2005.
- [78] Jean-Pierre Berenger. A perfectly matched layer for the absorption of electromagnetic waves. *Journal of Computational Physics*, **114**:185 200, 1994.
- [79] Peter J. F. Harris. *Carbon Nanotubes and Related Structures: New Materials for the Twenty-first Century*. Cambridge University Press, reprint edition, 2001.
- [80] Mildred S. Dresselhaus, Gene Dresselhaus, Phaedon Avouris, and R.E. Smalley. *Carbon Nanotubes: Synthesis, Structure, Properties and Applications*. Springer, first edition, 2001.
- [81] Aixtron - carbon nanotube and nanofiber systems.  
<http://www.aixtron.com/index.php?id=852&L=1>  
visited 2011-12-10
- [82] M. S Kabir, R.E. Morjan, O. Nerushev, P. Lundgren, S. Bengtsson, P Enoksson, and E.E.B. Campbell. Fabrication of individual vertically aligned carbon nanofibres on metal substrates from prefabricated catalyst dots. *Nanotechnology*, **17**:790, 2006.

- [83] Z. F. Ren, Z. P. Huang, J. W. Xu, J. H. Wang, P. Bush, M. P. Siegal, and P. N. Provencio. Synthesis of large arrays of Well-Aligned carbon nanotubes on glass. *Science*, **282** (5391):1105–1107, 1998.
- [84] Krijn P. De Jong and John W. Geus. Carbon nanofibers: Catalytic synthesis and applications. *Catalysis Reviews*, **42**:481–510, 2000.
- [85] M. Chhowalla, K. B. K. Teo, C. Ducati, N. L. Rupesinghe, G. A. J. Amaratunga, A. C. Ferrari, D. Roy, J. Robertson, and W. I. Milne. Growth process conditions of vertically aligned carbon nanotubes using plasma enhanced chemical vapor deposition. *Journal of Applied Physics*, **90** (10):5308–5317, 2001.
- [86] Stig Helveg et al. Atomic-scale imaging of carbon nanofibre growth. *Nature*, **427**:426–429, 2004.
- [87] R.E. Morjan, M.S. Kabir, S.W. Lee, O.A. Nerushev, P. Lundgren, S. Bengtsson, Y.W. Park, and E.E.B. Campbell. Selective growth of individual multiwalled carbon nanotubes. *Current Applied Physics*, **4** (6):591–594, 2004.
- [88] J. W. Seo, A. Magrez, M. Milas, K. Lee, V. Lukovac, and L. Forro. Catalytically grown carbon nanotubes: from synthesis to toxicity. *Journal of Physics D: Applied Physics*, **40** (6):R109–R120, 2007.
- [89] M. Meyyappan, Lance and Cassell Delzeit, and David Hash. Carbon nanotube growth by PECVD: a review. *Plasma sources science and technology*, **12**:205–216, 2003.
- [90] M. S Kabir, R. E. Morjan, O. A. Nerushev, P. Lundgren, S. Bengtsson, P. Enoksson, and E.E.B. Campbell. Plasma enhanced chemical vapour deposition growth of carbon nanotubes on different metal underlayers. *Nanotechnology*, **16**:458–466, 2005.
- [91] A. V Melechko, V. I Merkulov, T. E McKnight, M. A Guillorn, K. L Klein, D. H Lowndes, and M. L Simpson. Vertically aligned carbon nanofibers and related structures: Controlled synthesis and directed assembly. *Journal of applied physics*, **97** (41301):041301, 2005.
- [92] Jae-Hee Han, Tae Young Lee, Do Yoon Kim, Ji-Beom Yoo, Chong-Yun Park, Jin Ju Choi, Taewon Jung, In Taek Han, J. E. Jung, and J. M. Kim. High field-emission current of carbon nanotubes grown on TiN-coated ta substrate for electron emitters in a microwave power amplifier. *Journal of Vacuum Science & Technology B: Microelectronics and Nanometer Structures*, **22** :1636, 2004.
- [93] Jean-Baptiste A Kpetsu, Pawel Jedrzejowski, Claude Côté, Andranik Sarkissian, Philippe Mérel, Philips Laou, Suzanne Paradis, Sylvain Désilets, Hao Liu, and Xueliang Sun. Influence of ni catalyst layer and TiN diffusion barrier on carbon nanotube growth rate. *Nanoscale Research Letters*, **5** (3):539, 2010.

- [94] Anupama Arun, Helene Le Poche, Tonio Idda, Donatello Acquaviva, Montserrat Fernandez-Bolanos Badia, Philippe Pantigny, Paul Salet, and Adrian Mihai Ionescu. Tunable MEMS capacitors using vertical carbon nanotube arrays grown on metal lines. *Nanotechnology*, **22**:025203, 2011.
- [95] Raluca Elena Morjan. *Towards Controlled Growth and Applications of Carbon Nanotubes*. PhD thesis, Chalmers University of Technology, 2005.
- [96] Farzan Alavian Ghavanini. *Synthesis and characterization of vertically aligned carbon nanofibers for nanoscale devices*. PhD thesis, Chalmers University of Technology, Göteborg, 2011. ISBN: 978-91-7385-587-7.
- [97] M. A. Guillorn, T. E. McKnight, A. Melechko, V. I. Merkulov, P. F. Britt, D. W. Austin, D. H. Lowndes, and M. L. Simpson. Individually addressable vertically aligned carbon nanofiber-based electrochemical probes. *Journal of Applied Physics*, **91**:3824, 2002.
- [98] Xuesong Li, Xianfeng Zhang, Lijie Ci, Rakesh Shah, Christopher Wolfe, Swastik Kar, Saikat Talapatra, and Pulickel M Ajayan. Air-assisted growth of ultra-long carbon nanotube bundles. *Nanotechnology*, **19** (45):455609, 2008.
- [99] Mohammadreza Saeidi and Majid Vaezzadeh. Ultra-long carbon nanotube growth on catalyst. *Physica E: Low-dimensional Systems and Nanostructures*, **41** (9):1723–1726, 2009.
- [100] M. R. Gonçalves, A. Siegel, and O. Marti. Influence of the light-scattering form factor on the bragg diffraction patterns of arrays of metallic nanoparticles. *Journal of Microscopy*, **229** (3):475–482, 2008.
- [101] Jun Rong Ong, G. Alagappan, P. Wu, and X. W. Sun. White beam diffraction in a two-dimensional photonic crystal. *Journal of the Optical Society of America A*, **26** (5):1256–1259, 2009.
- [102] Harland G Tompkins and Eugene Irene, (Eds.). *Handbook of Ellipsometry*. Springer-Verlag GmbH & Co. KG, 2005.
- [103] Spectroscopic ellipsometers – J.A. Woollam co.  
<http://www.jawoollam.com/>  
visited 2011-12-10
- [104] Yurii A Vlasov and Sharee J McNab. Coupling into the slow light mode in slab-type photonic crystal waveguides. *Optics Letters*, **31**:50 52, 2006.
- [105] Stefan Bengtsson. On comb-like varactor, 2008. Private communication.
- [106] Chun-Hung Lin, Hsuen-Li Chen, Wen-Chi Chao, Chung-I Hsieh, and Wen-Huei Chang. Optical characterization of two-dimensional photonic crystals based on spectroscopic ellipsometry with rigorous coupled-wave analysis. *Microelectronic Engineering*, **83** (4-9):1798–1804, 2006.

- [107] C. I. Hsieh, H. L. Chen, W. C. Chao, and F. H. Ko. Optical properties of two-dimensional photonic-bandgap crystals characterized by spectral ellipsometry. *Microelectronic Engineering*, **73-74** :920–926, 2004.
- [108] N. Paraire and Y. Benachour. Investigation of planar photonic crystal band diagrams under the light cone using surface coupling techniques. *Applied Physics B*, **89**:245–250, 2007.
- [109] Jie-Hua Zhao, Todd Ryan, Paul S. Ho, Andrew J. McKerrow, and Wei-Yan Shih. Measurement of elastic modulus, poisson ratio, and coefficient of thermal expansion of on-wafer submicron films. *Journal of Applied Physics*, **85** (9):6421, 1999.
- [110] Gabriel M. Rebeiz. *RF MEMS*. John Wiley & Sons, Inc., Hoboken, NJ, USA, 2003.
- [111] Samuel Olsson. *Electrostatically tunable periodic waveguides with carbon nanofibres*. MSc thesis, Chalmers University of Technology, Göteborg, 2008.
- [112] Bryan Ellis, Marie A. Mayer, Gary Shambat, Tomas Sarmiento, James Harris, Eugene E. Haller, and Jelena Vuckovic. Ultralow-threshold electrically pumped quantum-dot photonic-crystal nanocavity laser. *Nature Photonics*, **5** (5):297–300, 2011.
- [113] Stephen A. Campbell. *The Science and Engineering of Microelectronic Fabrication*. Oxford University Press, USA, 2 edition, 2001.
- [114] JEOL JBX-9300FS electron beam lithography system training.  
[http://www.nanolithography.gatech.edu/JEOL\\_JBX-9300FS\\_Training.pdf](http://www.nanolithography.gatech.edu/JEOL_JBX-9300FS_Training.pdf)  
visited 2011-12-10
- [115] Mihir Parikh. Corrections to proximity effects in electron beam lithography. I. theory. *Journal of Applied Physics*, **50**:4371, 1979.
- [116] V.V. Ivin, M.V. Silakov, D.S. Kozlov, K.J. Nordquist, B. Lu, and D.J. Resnick. The inclusion of secondary electrons and bremsstrahlung x-rays in an electron beam resist model. *Microelectronic Engineering*, **61-62**:343–349, 2002.
- [117] PMMA and LOR under layer resists - MicroChem.  
<http://www.microchem.com/Prod-PMMA.htm>  
visited 2011-12-10
- [118] Polymethylglutarimide (PMGI) resists - MicroChem.  
[http://www.microchem.com/Prod-PMGI\\_LOR.htm](http://www.microchem.com/Prod-PMGI_LOR.htm)  
visited 2011-12-10
- [119] Oxford instruments: plasma technology processes.  
<http://www.oxford-instruments.com/products/etching-deposition-growth/processes/Pages/plasma-technologies-processes.aspx>  
visited 2011-12-10

- [120] J. Tonotani, T. Iwamoto, F. Sato, K. Hattori, S. Ohmi, and H. Iwai. Dry etching characteristics of TiN film using Ar/CHF<sub>3</sub>, Ar/Cl<sub>2</sub>, and Ar/BCl<sub>3</sub> gas chemistries in an inductively coupled plasma. *Journal of Vacuum Science & Technology B: Microelectronics and Nanometer Structures*, **21** (5):2163, 2003.
- [121] M.C. Lemme, J.K. Efavi, T. Mollenhauer, M. Schmidt, H.D.B. Gottlob, T. Wahlbrink, and H. Kurz. Nanoscale TiN metal gate technology for CMOS integration. *Microelectronic Engineering*, **83** (4-9):1551–1554, 2006.
- [122] K. R Williams, K. Gupta, and M. Wasilik. Etch rates for micromachining processing-Part II. *Journal of Microelectromechanical Systems*, **12** (6):761–778, 2003.